

PROGRAMA DE DOCTORADO EN INGENIERÍA INDUSTRIAL: TECNOLOGÍAS DE DISEÑO Y  
PRODUCCIÓN INDUSTRIAL  
EN RÉGIMEN DE COTUTELA

TESIS DOCTORAL

MODELO MULTIDOMINIO Y SU APLICACIÓN AL  
MANTENIMIENTO EN CONDICIÓN DE TRANSMISIONES  
MEDIANTE ENGRANAJES

PhD THESIS

MULTI-DOMAIN MODEL AND CONDITION MONITORING OF  
GEAR TRANSMISSION

AUTORA

SAFA BOUDHRAA

DIRECTORES

ALFONSO FERNÁNDEZ DEL RINCÓN

FAKHER CHAARI

UNIVERSIDAD DE CANTABRIA

EN COTUTELA CON LA UNIVERSIDAD DE SFAX (TÚNEZ)

Escuela de **Doctorado** de la Universidad de Cantabria

Santander 2022

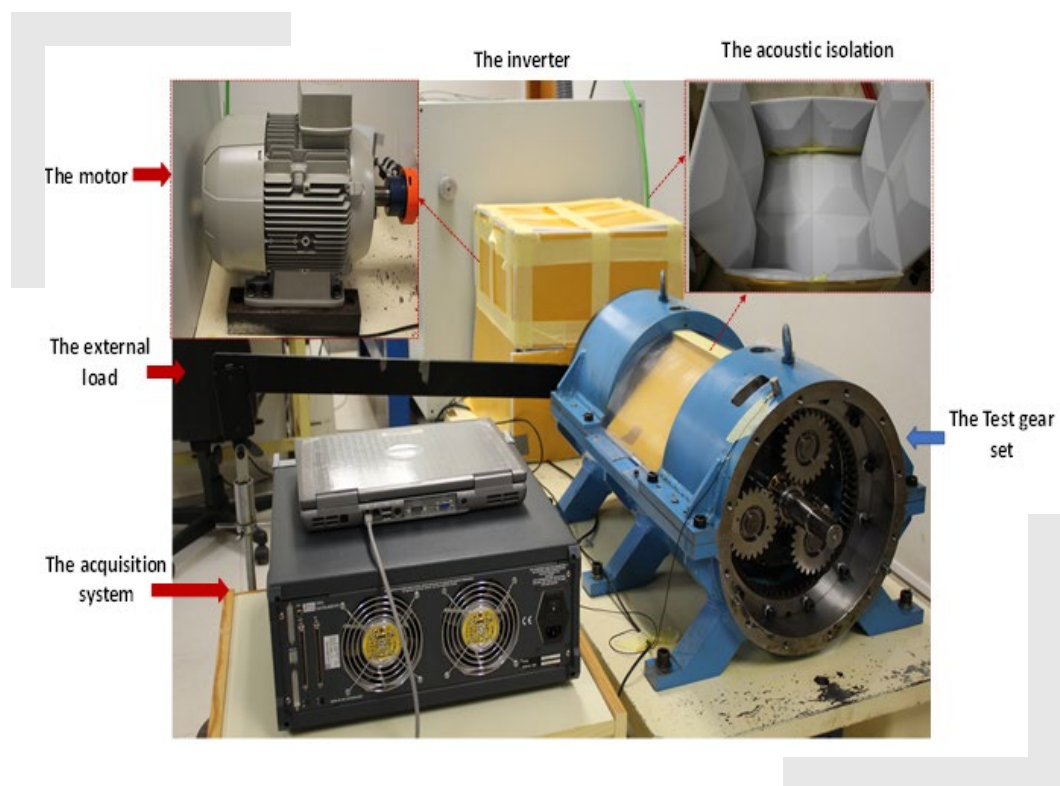
TESIS  
DOCTORAL



2022

MODELO MULTIDOMINIO Y SU APLICACION AL MANTENIMIENTO EN CONDICIÓN DE  
TRANSMISIONES MEDIANTE ENGRANAJES





The present PhD thesis study the electro-mechanical interaction between an asynchronous motor and a mechanical transmission by using the motor current signature analysis (MCSA) technique. The study combines a double approach theoretical and experimental. Theoretical models have been developed for simulate the dynamic behavior of electrical and mechanical components in order to get a better knowledge on the relationship between both domains. Park transformation has been applied on the simulation of an asynchronous motor that drives the mechanical transmission. Several examples of mechanical transmission have been modeled, both ordinary and planetary, including the parametric excitation due to the variable gear mesh stiffness as well as the presence of defects with different sizes and locations. The developed models have been validated by the assessment of experimental measurements recorded on two laboratory test benches, comparing the signals coming from different domains as electrical currents, mechanical vibration and sound pressure both in sound condition and in presence of defects.

Esta tesis estudia la interacción electro-mecánica entre un motor asíncrono y una transmisión mecánica mediante la técnica de análisis de la corriente del motor (Motor Current Signature Analysis MSCA). El estudio combina un doble enfoque teórico y experimental. Se han desarrollado modelos teóricos que simulan el comportamiento dinámico de componentes eléctricos y mecánicos con el propósito de conseguir un mejor conocimiento de la relación entre ambos dominios. Se ha utilizado la transformada de Park en la simulación de un motor asíncrono que acciona la transmisión mecánica. Se han modelizado diversos ejemplos de transmisión, tanto ordinarias como planetarias, incorporando la excitación paramétrica debida a la rigidez de engrane variable, así como la presencia de defectos con distintos tamaños y localizaciones. Los modelos desarrollados han sido validados mediante la evaluación de registros experimentales obtenidos en dos bancos de ensayo de laboratorio, comparando las señales procedentes de distintos dominios como corriente eléctrica, vibraciones mecánicas y presión sonora tanto en condiciones normales como en presencia de defectos.



## Dedication

“A Journey of a Thousand Miles Begins with a Single Step”. Research is a very long and tiring journey, but nothing comes for free.

Therefore, I dedicate my degree and the effort in this work to my family who has always stood guard for this dream.

To my MOM, the first source of inspiration and reason for this hard work.

To the little piece of heaven I have, my daughter Emna, I hope that one day you will be proud of this achievement.

To my husband, who has always been by my side encouraging me.

To my father, sisters, and brothers, to my aunts and uncle who have always believed in me as a brilliant exception in the family.

To the soul of my sweetheart, my grandmother, and my grandfather, I wished that they witnessed this achievement. They would be so proud.

To all my friends who did not stop believing in me no matter how long the journey was.

Great dreams are always coming from a very hopeful environment, and I am so lucky to have such a dreaming family.

It was very hard, but ***I DID IT***.

*Safa Boudhraa*



## **Acknowledgement**

The research activity is a huge team effort. The collective effort had certainly supported the individual activity by guidelines, orientations and correcting.

Within this context, I had the opportunity to be part of a collaboration between the Laboratory of Mechanics, Modelling and Production, in the National School of Engineers of Sfax-Tunisia and the Group of Mechanical Engineering, University of Cantabria-Spain.

I express my deep gratitude to my directors of this thesis Professor Fakher Chaari and Professor Alfonso Fernandez Del Rincon for their unconditional support throughout this research. I also thank Professor Mohamed Amine ben Souf for his help and assistance.

I would like to thank my Tutor, Professor Fernando Viadero for giving me the chance to be part of the Laboratory of Mechanical Engineering, University of Cantabria-Spain. Also, I am grateful to Professor Mohamed Haddar for this great research opportunity.

I want to express my deep appreciation to each member of the mechanical engineering department for their help and support during my experimental research activity and for being so warm and welcoming.

Finally, I would like to express my sincere gratitude to Professor Ana for her hospitality and support during the period I have been in Spain.

*Safa Boudhraa*



# Abstract

For as long as humans have been using mechanical mechanism in power transmission, this revolutionary field has been in permanent progress. Planetary gearbox is one of the common setups used in the industries.

In fact, planetary gears are exposed to a lot of excitations of vibrations and noise. These excitations can be internal, specific to the actual running of the system, or external, associated with fluctuations in motor torque, load torque and speed. Scientific research is working on optimizing these components design and especially working on controlling its operating state using non-destructive techniques. In addition, the criticality of these systems has made monitoring it one of the biggest scientific and industrial concern. The presence of any gears defect impacts the dynamic behaviour of the electromechanical system and generates load perturbation.

## Main highlights

The objective of this PhD thesis is to study the electro mechanical interaction between an asynchronous motor and a planetary gearbox. The ultimate work is focused on the motor current signature analysis (MCSA) technique. The current signal was presented simultaneously with mechanical signals: vibrations and acoustic pressure.

First, numerical models were used to define the impact of the gears' behaviour on the current signal. The initial model was composed of the electrical part of the asynchronous motor and a dynamic model of the planetary gears. The motor was modelled using Park transformation that generates a new bi-phased model. For the mechanical system, a one stage spur gears example was used. The objective behind using this model was first to have the hand to gears modelling then, to approve the electrical model and to validate the electromechanical coupling. The second mechanical system was a double stage planetary gearbox testbench. In this part a torsional model was used to simulate the planetary test bench. In both cases, the numerical model determines the impact of the load perturbation due to the mechanical system on the motor current. The numerical study has studied the impact of a local crack on the electrical signal. In order to validate the model, different simulations took place by implementing defects with different sizes, localisation, and number.

Later, the numerical simulations were followed by an experimental test. The experiments were elaborated on a double stages' planetary gearbox.

The experimental tests were held also on two test benches. First, electrical clamps have been connected to a geared motor connected to one stage helicoidal gears. The objective of these measurements was to investigate the sensitivity of the instrument used in current signal recording. The same electrical clamp was used to record the phase current in the asynchronous motor driving the planetary gearbox.

Meanwhile, mechanical signals were taken simultaneously. Microphones were used to save the acoustic pressure around the whole test bench. Besides, accelerometers were mounted to investigate the vibrations level of the system. Finally, a teeth crack was implemented on the planet gears in the planetary gearbox to study the impact of defects on current signal.

## **Results and discussion**

The numerical simulations of the current signals were presented in the temporal domain and also in the frequency spectrum using the Fast Fourier Transformation (FFT). The frequency spectrum presents the electromechanical interaction between systems by the appearance of the related mechanical frequencies. These frequencies are given as a modulation of the mechanical frequencies by the supply frequency. In the healthy configuration, the meshing frequency and the rotating frequencies appears as a mechanical key frequency. After including gears defects, the current signal highlights the appearance of additional frequencies related to the damaged component. Analysing the motor current frequency spectrum can describes the state of the mechanical system by the visible frequencies.

The current signal results obtained from the numerical simulations were supported by experimental tests. The experiments have proven the current signal is sensitive the behaviour of the mechanical system by the appearance of related frequencies. The vibrations signals and the acoustic pressure taken simultaneously has confirmed the behaviour of the mechanical system seen in the motor current signal.

In order to study the sensitivity of the current signal, a wear degradation study has taken place. For the micro-pitting defects mechanical signals such vibrations are more sensitive than current. This is mainly related to the location of the sensors used.

## **Conclusion**

Finally, as a conclusion of this work the motor current signal is a relevant non-destructive technique that can be used to study the behaviour of gears systems. At some level, the frequency of the spectrum of the motor current signal analysis presents the impact of the dynamic behaviour of the gears on the electrical signals. The current signal is sensitive to different sizes and location of teeth defects. Finally, the electrical outcome has been approved by the comparison study between current and the vibrations, acoustic pressure.

## **Future work**

Given the conclusion of the thesis presented, this research work can be extended in different perspectives. First the numerical model can be improved by using a 3D model of the planetary test bench and a permeance model to describe the electrical system. This system can provide a deep description of the dynamic behaviour of the electromechanical system. Also, in the numerical simulations, the

transmission errors can be taken into consideration in order to reflect the real situation of the electromechanical systems in industries.

Finally, regarding the experiment's tests, the use of the electrical clamps is not very sensitive to the wear degradation phenomena. therefore, it is recommended to extend the research studies to different current recording tools.



# Resumen

Desde su invención, las transmisiones de potencia mecánicas han sufrido una evolución constante. Las transmisiones planetarias son una de las configuraciones más comúnmente utilizadas en la industria.

De hecho, las transmisiones planetarias sufren diversas excitaciones que conducen a problemas de ruido y vibraciones. Estas excitaciones pueden ser internas, debidas a las interacciones específicas del sistema, o externas, asociadas a las fluctuaciones del par motor, del par resistente y de la velocidad. Actualmente se trabaja en optimizar el diseño de todos los componentes y, especialmente, en controlar su estado de operación utilizando técnicas no destructivas. Además, el hecho de que las transmisiones sean un componente tan crítico, hace que su correcta monitorización sea una de las principales preocupaciones, tanto desde el punto de vista científico como industrial. La presencia de cualquier tipo de defecto en los engranajes afecta al comportamiento dinámico del sistema electromecánico y genera perturbaciones en la carga transmitida.

## Metodología

El objetivo de esta Tesis Doctoral es estudiar la interacción electromecánica entre un motor asíncrono y una transmisión planetaria. El trabajo se centra en la técnica de análisis de la intensidad de corriente del motor (MCSA). La intensidad de corriente se manifiesta desde el punto de vista mecánico mediante vibraciones y presión acústica.

En primer lugar, se utilizaron modelos numéricos para definir el impacto del comportamiento de los engranajes en la intensidad de corriente. El modelo teórico se compone por una parte eléctrica que representa el motor asíncrono y una parte mecánica que representa el comportamiento dinámico de la transmisión planetaria. El motor se modelizó utilizando la transformación de Park, que genera un modelo bifásico. Para la transmisión planetaria, se utilizó una etapa de engranajes con dientes rectos. El objetivo de este modelo inicial era familiarizarse con el modelizado de engranajes, probar el modelo eléctrico y validar el acoplamiento electromecánico. Posteriormente, se modelizó un banco de ensayos con dos etapas de transmisiones planetarias, simuladas con un modelo torsional. En ambos casos, los modelos numéricos son capaces de determinar el impacto en la perturbación de la carga en la intensidad de corriente, estudiando el efecto de una grieta en la señal eléctrica. Se implementaron

diferentes tipos de defectos, variando su tamaño, localización y número para comprobar los resultados y validar el modelo.

Posteriormente, se diseñó una campaña experimental, que se llevó a cabo en dos bancos de ensayos de transmisiones planetarias de doble etapa. Inicialmente se usó una pinza amperimétrica con el objetivo de obtener la sensibilidad del instrumental utilizado para medir la intensidad de corriente eléctrica. Esta misma pinza se utilizó para medir la fase de la corriente del motor asíncrono. En estos mismos ensayos se grabó también la presión acústica alrededor del banco de ensayos con la ayuda de micrófonos y se registraron vibraciones con acelerómetros. Finalmente, se generó una grieta en un diente de un engranaje para estudiar su efecto en la señal de intensidad de corriente.

### **Resultados y discusión**

Las simulaciones numéricas de las señales de intensidad de corriente se han obtenido tanto en el dominio temporal como en el de la frecuencia, utilizando para ello la transformada rápida de Fourier (FFT). El espectro de frecuencia recoge la interacción mecánica entre sistemas mediante la aparición de frecuencias mecánicas relacionadas, que se manifiestan como una modulación de la frecuencia mecánica. En la configuración sin defectos, la frecuencia de engrane y las frecuencias de giro se observan con claridad. Cuando se incluyen los defectos, la señal de la intensidad de corriente muestra la aparición de frecuencias relacionadas con el componente dañado.

Respecto a la validación experimental, se ha comprobado que el comportamiento del sistema mecánico afecta a la señal de intensidad de corriente, ya que aparecen frecuencias relacionadas con él. Las medidas sobre las vibraciones y la presión acústica han confirmado el comportamiento del sistema mecánico recogido en la señal de intensidad de corriente. Para poder estudiar la sensibilidad de la señal de intensidad de corriente, se llevó a cabo un estudio de desgaste. Las micropicaduras en los engranajes se detectan mejor con las medidas mecánicas (por ejemplo, vibraciones), que con la medida de la señal de intensidad de corriente. Esto se debe fundamentalmente a la localización de los sensores.

### **Conclusiones**

Como conclusión de este trabajo, se puede establecer que la señal de intensidad de corriente del motor es una técnica no destructiva cuya utilización es viable para el monitorizado de sistemas de transmisión planetarias. A cierto nivel, el espectro de frecuencias de la señal de intensidad

de corriente del motor recoge el impacto producido por el comportamiento dinámico de los engranajes. De hecho, la señal de intensidad de corriente del motor puede detectar la presencia de defectos y varía según el tamaño y la localización de los mismos. Para validarlo, se han cruzado datos con las otras medidas realizadas de vibración y presión acústica.

### **Trabajo futuro**

Dada la conclusión principal de este trabajo de Tesis Doctoral, el camino a seguir presenta diferentes ramales. El modelo numérico se puede mejorar pasando del plano al espacio tridimensional del banco de ensayos, y un modelo de permeancia para describir el sistema eléctrico. También se podrían tener en cuenta los errores de transmisión para representar la realidad con mayor exactitud.

Respecto a los ensayos experimentales, el uso de las pinzas amperimétricas no parece ser muy acertadas para los ensayos de desgaste, por lo que se recomienda explorar otras vías.



# List of content

Chapter 1: Bibliographical review .....	5
1. Introduction.....	5
2. Dynamic modelling of electromechanical systems .....	6
2.1 Dynamic modelling of asynchronous motors.....	6
2.1.1 Analytical models of asynchronous machines (dq transformation) .....	6
2.1.2 The semi analytical models of asynchronous machines (Permeances networks).....	8
2.1.3 The Numerical models of asynchronous machines (Finite Element Method) .....	10
2.2. The dynamic modelling of the planetary gears .....	10
2.2.1. Lumped parameters models of gears.....	11
2.2.2. Planetary gear dynamic modelling:.....	12
2.2.3. Finite element modelling of Planetary gearbox.....	14
3. The gears defect .....	14
3.1. Gears defects classification .....	14
3.1.1. Local teeth damage.....	15
3.1.2. Distributed Damage.....	16
3.2. Gear defects modelling.....	18
3.2.1. Analytical modelling.....	18
4. Methods used in detecting gear defects.....	20
4.1. Vibration signals.....	21
4.2. Acoustic emission (AE).....	23
4.3. Acoustic radiation.....	25
4.4. Motor Current Signature Analysis (MCSA).....	27
5. Signal processing techniques.....	29
5.1. Time domain.....	29
5.2. Time frequency Domain.....	30
5.2.1. Fast Fourier transform (FFT).....	30
5.2.2. The heterodyne technique.....	30
5.2.3. Wavelet transform method .....	31
5.2.4. Empirical mode decomposition (EMD) .....	31
5.2.5. Time synchronous Averaging.....	31
Conclusion.....	32
Chapter 2: Numerical model description.....	34
1. Introduction.....	34
2. Gear dynamic model .....	34
3. Electric Drive modelling .....	38

3.1. Model's assumptions .....	38
3.2. Analytical Development.....	38
4. The impact of the gear's teeth crack on the gear meshing stiffness .....	41
5. Electromechanical interaction .....	43
5.1. Theoretical background.....	43
5.3. Coupling model .....	46
5.3. Solution .....	47
6. Case study: Simple stage of spur gears .....	47
6.1. The electromechanical system.....	48
6.2. Time motor current signal <b><i>Ids</i></b> for coupled system for healthy configuration.....	48
6.3. The Mechanical signals in presence of tooth crack.....	50
6.4. The impact of signal defect on current signal .....	51
6.4.1. Single defect impact on the stator current .....	51
6.3.3. The impact of the defect severity on the stator current .....	52
6.3.3. The impact of combined defects of the stator current .....	53
7. Conclusion.....	54
Chapter 3: Experimental test benches .....	56
1. Introduction .....	56
2. Low-speed test bench.....	56
3. Planetary gearbox testbench.....	58
4. Instrumentations .....	61
4.1. Sensors .....	62
4.2. Acquisition .....	63
5. Conclusion.....	64
Chapter 4: Dynamic behaviour of the double stage planetary gearbox by the motor current signal ....	67
1. Introduction.....	67
2. Assumptions.....	67
2.1. Define parameters.....	67
2.2. Key frequencies.....	69
3. Numerical model of the planetary testbench.....	70
4. The impact of the mechanical behaviour on the current signal.....	72
4.1. Temporal domain response .....	72
4.2. Frequency domain responses.....	74
5. Conclusion.....	75
Chapter 5: The Multiphysics investigations on the experimental testbench: motor stator current signal, vibrations level and acoustic pressure .....	77
1. Introduction .....	77
2. The phase Current response to the Low speed testbench .....	77

2.1.	The current signal for Free motor:.....	78
2.2.	The current signal after coupling the motor to the gears.....	81
3.	Multiphysics study of the behaviour of the Planetary gearbox testbench.....	83
3.1.	The motor phase current signal.....	83
3.1.1.	Current signal for Free motor.....	83
3.1.2.	The impact of the planetary gearbox on measurements.....	84
3.2.	The vibrations signal.....	86
3.3.	The Acoustic pressure of the mechanical system.....	87
4.	Conclusion.....	88
Chapter 6: The impact of the gears defect on the planetary gearbox's dynamic behaviour.....		91
1.	Introduction.....	91
2.	Numerical study of the tooth crack on the motor current signal.....	91
2.1.	Numerical modelling of Tooth crack.....	91
2.2.	Motor current signal response in the presence of tooth crack in planetary gearbox: Temporal response.....	92
2.2.1.	Sun defect.....	93
2.2.2.	Planet defect.....	94
2.3.	The frequency spectrum of the stator current in the presence of tooth defect.....	95
2.3.1.	The impact of the Planet Defect on the frequency spectrum:.....	95
3.	The experimental study of the impact of gears defect.....	96
3.1.	The implementation of the teeth defects in planetary gearbox testbench.....	96
3.2.	The impact of the tooth defect on the MCSA, Vibration's level and the acoustic pressure to gears tooth crack.....	97
3.2.1.	The impact of the planet defect on the temporal measurement.....	98
3.2.2.	The signals in the frequency domain.....	99
3.2.3.	Combined defects in the test gearbox.....	105
4.	The wear degradation phenomena impact of the phase current signal.....	107
4.1.	The degradation states.....	107
4.2.	The impact of the wear degradation on the current spectrum.....	108
4.3.	Kurtosis.....	110
4.4.	The impact of sun teeth wears on current signals.....	111
5.	The vibrations signals in the presence of the wear degradation.....	112
Conclusion.....		116



# List of Figures

FIGURE.1.1: PLANETARY GEARBOX.....	5
FIGURE.1.2: SCHEMATIC REPRESENTATION OF THE MAGNETIC AXES OF THE ASYNCHRONOUS MACHINE [1].....	7
FIGURE.1.3: EXTRACT OF THE EQUIVALENT MAGNETIC CIRCUIT OF AN INDUCTION MACHINE [5] .....	9
FIGURE.1.4: TUBE FLUX [6] .....	9
FIGURE.1.5: DYNAMIC MODEL USED BY TUPLIN (MASS- SPRING) [8].....	11
FIGURE.1.6: GENERAL MODEL OF GEAR TOOTH [8] .....	12
FIGURE.1.7: SOME TORSIONAL MODELS WITH TOOTH COMPLIANCE [8].....	12
FIGURE.1.8: PLANETARY GEAR DYNAMIC MODELLING [11] .....	13
FIGURE.1.9: GEARS DEFECTS CLASSIFICATION [15].....	14
FIGURE.1.10: PITTING [17].....	15
<b>TOOTH BREAKAGE -BENDING FATIGUE.....</b>	<b>16</b>
FIGURE.1.11: BREAKAGE [17] .....	16
FIGURE.1.12. SCORING [20] .....	17
FIGURE.1.13: SCUFFING [21] .....	17
FIGURE.1.14: OVERHEATING DEFECT ON A GEAR .....	18
FIGURE.1.15: THE SHAPE OF THE SPALLING [26].....	19
FIGURE.1.16: NONUNIFORM CANTILEVER BEAM MODELLING OF TOOTH WITH SPALLING [26] .....	20
FIGURE.1.17: MODELLING GEAR’S CRACK USING FINITE ELEMENT METHOD [27] .....	20
FIGURE.1.18: THE EXPERIMENTAL SETUP TEST-ACOUSTICS RESEARCH LAB., AMIR KABIR UNIVERSITY OF TECHNOLOGY [28] .....	22
FIGURE.1.19: THE SPECTRA OF THE ACCELERATIONS SIGNAL OF THE TEST RING [35] .....	23
FIGURE.1.20: AE PROCESS TREATMENT [38] .....	24

FIGURE.1.21: EXPERIMENTAL DISPOSITIVE [43] .....	25
FIGURE.1.22: PRESSURE SPECTRUM OBSERVED IN THE CENTRE OF THE FLUID CAVITY [43].....	25
FIGURE.1.23: EXPERIMENTAL SET-IN PRESENCE OF MICROPHONES [44] .....	26
FIGURE.1.24: FREQUENCY SPECTRUM OF SOUND POWER [44] .....	26
FIGURE.1.25: ASYNCHRONOUS MOTOR [45] .....	27
FIGURE.1.26: THE STATOR PHASE CURRENT RECORDING.....	27
FIGURE.2.1: SCHEMATIC OF SPUR GEAR MODEL: (A) GLOBAL SYSTEM AND (B) WHEEL-PINION CONTACT .....	35
FIGURE.2.2: THE EQUIVALENT BI-PHASED MACHINE OBTAINED FROM AN ASYNCHRONOUS MOTOR .....	40
FIGURE.2.3: THE GEAR MESHING STIFFNESS .....	42
FIGURE.2.4: THE GEAR MESHING STIFFNESS IN THE PRESENCE OF TOOTH CRACK: (A): THE MESHING STIFFNESS IN [0s,0.4s]; (B): ZOOM OF THE MESHING STIFFNESS IN [0s,0.08s] .....	43
FIGURE.2.5: SCHEME OF THE COUPLING MODEL OF THE ELECTROMECHANICAL SYSTEM.....	46
FIGURE.2.6: STATOR CURRENT SIGNAL $i_{ds}$ ON THE DQ FRAME .....	49
(A): THE CURRENT STATOR SIGNAL IN [0s;4s]; (B): ZOOM OF THE CURRENT STATOR SIGNAL IN[2s;2,1s].....	49
FIGURE.2.7: THE VELOCITY OF THE PINION IN TWO OPERATING CONFIGURATIONS.....	50
(A): THE VELOCITY OF THE PINION IN [0s;1,6s]; (B): ZOOM OF THE PINION VELOCITY IN[1s;1,6s] .....	50
FIGURE.2.8. STATOR CURRENT SIGNAL $i_{ds}$ ON THE DQ FRAME .....	51
FIGURE.2.9. FREQUENCY SPECTRUM OF THE STATOR CURRENT SIGNAL $i_{ds}$ ON THE DQ FRAME IN HEALTHY CONFIGURATION AND DEFECTED CASE .....	52
FIGURE.2.10. FREQUENCY SPECTRUM OF THE STATOR CURRENT SIGNAL $i_{ds}$ ON THE DQ FRAME FOR DEFECT'S DIMENSION .....	53
FIGURE.2.11. FREQUENCY SPECTRUM OF THE STATOR CURRENT SIGNAL $i_{ds}$ ON THE DQ FRAME IN HEALTHY CONFIGURATION AND DEFECTED CASE (FOR COMBINED DEFECTS).....	54
FIGURE.3.1.: THE EXPERIMENTAL TEST RIG .....	57
FIGURE.3.2: THE GEARED MOTOR STRUCTURE [1].....	57

FIGURE.3.3: THE LOW-SPEED TEST BENCH SYSTEM .....	58
FIGURE.3.4: THE EXPERIMENTAL TEST BENCH (A) THE EXPERIMENTAL SET (B) LOAD APPLICATION .....	60
FIGURE.3.5: THE ELECTRICAL CABINET .....	61
FIGURE.3.6: PLACEMENT OF DIFFERENT SENSORS ON THE TEST BENCH .....	62
FIGURE.3.7: SENSORS USED IN THE TEST: (A) CLAMPS, (B) ACCELEROMETER, (C) TACHOMETER AND (D) MICROPHONES .....	63
FIGURE.3.8: SCADAS DATA ACQUISITION: (A) INPUT SCHEDULING; (B) THE SCADAS SYSTEM MANAGED BY LMS TEST LAB .....	64
FIGURE.4.1. THE T-EQUIVALENT CIRCUIT OF ASYNCHRONOUS MOTOR.....	68
FIGURE.4.2.: THE DOUBLE STAGE GEARBOX SYSTEM (A): EXPERIMENTAL TEST RIG; (B): NUMERICAL MODEL OF THE SYSTEM AND (C) DISPOSAL OF THE PLANETS ON THE CARRIER .....	69
FIGURE.4.5: NUMERICAL MODEL OF THE TEST BENCH: (A) KINEMATIC AND (B) DYNAMIC MODEL.....	70
FIGURE.4.6: CURRENT SIGNAL FOR HEALTHY CONFIGURATION: (A): THE CURRENT SIGNAL IN [0s,1s] AND (B): ZOOM OF THE CURRENT SIGNAL IN [0.5s,0.7s].....	73
FIGURE.4.7: THE FREQUENCY SPECTRUM OF THE <i>ids</i> CURRENT IN THE HEALTHY CONFIGURATION .....	74
FIGURE.4.8: THE FREQUENCY SPECTRUM OF A PHASE CURRENT IN THE HEALTHY CONFIGURATION .....	75
FIGURE.5.1: THE CURRENT SIGNAL OF A FREE MOTOR: (A) IN [0s,35s] AND (B) ZOOM OF THE CURRENT SIGNAL IN [0s,0.5s] .....	78
FIGURE.5.2: THE FREQUENCY SPECTRUM OF THE CURRENT SIGNAL FOR FREE MOTOR .....	79
LINEAR SCALE (B) LOGARITHMIC SCALE.....	79
FIGURE.5.3: THE CURRENT FREQUENCY SPECTRUM HIGHLIGHTING THE IMPACT OF THE GEARBOX CONNECTED TO THE MOTOR. (A) : [0Hz, 500Hz] ; (B)[0Hz,90Hz] ; (c)[90Hz,500Hz].....	80
FIGURE.5.4: THE CURRENT SPECTRUM WHILE THE MOTOR IS CONNECTED TO THE HELICOIDAL PAIR OF GEARS.....	82
FIGURE.5.5: THE FREQUENCY SPECTRUM OF THE CURRENT SIGNAL FOR FREE MOTOR .....	84
FIGURE.5.6: THE FREQUENCY SPECTRUM CURRENT SIGNAL (BLUE: FOR FREE MOTOR, RED: THE MOTOR IS ALREADY CONNECTED TO THE PLANETARY GEARBOX) ;(A) ZOOM IN FREQUENCY RANGE [0Hz;300Hz] (B) ZOOM IN FREQUENCY RANGE [260Hz;400Hz] (C) CURRENT SIGNAL IN THE PRESENCE OF DEFECT [0Hz;100Hz] .....	86
FIGURE.5.7: THE FREQUENCY SPECTRUM OF THE VIBRATIONS SIGNALS: (A) THE FREQUENCY SPECTRUM IN [0Hz, 2000Hz] AND (B) ZOOM OF THE FREQUENCY SPECTRUM OF THE VIBRATIONS SIGNAL IN [900Hz,1000Hz].....	87

FIGURE.5.8: THE FREQUENCY SPECTRUM OF THE ACOUSTIC PRESSURE: (A) THE SIGNAL IN [0Hz,1100Hz] AND (B) ZOOM OF THE ACOUSTIC PRESSURE SPECTRUM IN [900Hz, 1100Hz] .....	88
FIGURE.6.1: THE GEAR MESHING FREQUENCY: (A)THE GEAR MESHING STIFFNESS FOR THE HEALTHY CONFIGURATION RING-PLANET1 ; (B) THE GEAR MESHING STIFFNESS FOR THE HEALTHY CONFIGURATION SUN-PLANET1; (B) THE IMPACT OF THE TOOTH DEFECT ON THE GEAR MESHING STIFFNESS RING-PLANET1 .....	92
FIGURE.6.2. TEMPORAL EVOLUTION OF THE CURRENT SIGNAL <i>ids</i> (A): COMPARISON BETWEEN THE HEALTHY CONFIGURATION AND THE DEFECTED CASE, (B): CURRENT SIGNAL IN THE PRESENCE OF SUN DEFECT .....	93
FIGURE.6.3: TEMPORAL EVOLUTION OF THE CURRENT SIGNAL <i>IDS</i> FOR PLANET DEFECT; (A): THE CURRENT SIGNAL FOR ONE FACE DEFECT; (B): THE CURRENT SIGNAL FOR DOUBLE FACE DEFECT .....	94
FIGURE.6.4: THE FREQUENCY SPECTRUM IN OF THE <i>IDS</i> CURRENT IN THE PRESENCE OF PLANET DEFECT .....	95
FIGURE.6.5: THE FREQUENCY SPECTRUM OF THE PHASE CURRENT IN THE PRESENCE OF PLANET DEFECT (RED: IN THE PRESENCE OF THE DEFECT; BLUE FOR THE HEALTHY CONFIGURATION) (NUMERICAL SIMULATIONS) .....	96
FIGURE.6.6: DIFFERENT GEARS DEFECTS: (A) HEALTHY CONFIGURATION, (B) WEAR DEGRADATION, (C) PLANET DEFECT AND (D) SUN DEFECT .....	97
FIGURE.6.7: TEMPORAL SIGNAL OF THE MEASUREMENTS (RED: SIGNAL IN THE PRESENCE OF DEFECT; BLUE: HEALTHY CONFIGURATION): (A)THE CURRENT SIGNAL; (B) THE VIBRATION SIGNAL OF THE TEST GEARBOX; (C) THE ACOUSTIC PRESSURE .....	98
FIGURE.6.8: THE CURRENT SPECTRUM IN THE PRESENCE OF THE PLANET DEFECT (RED: DEFECTED CONFIGURATION; BLUE: HEALTHY CONFIGURATION) .....	99
FIGURE.6.9: COMPARING BETWEEN THE VIBRATION'S FREQUENCY SPECTRUM FOR HEALTHY CONFIGURATION AND IN THE PRESENCE OF PLANET DEFECT .....	100
FIGURE.6.11: THE VIBRATIONS SPECTRUM IN THE PRESENCE OF PLANET DEFECT IN A FREQUENCY RANGE [0Hz,30Hz] ;(A): THE VIBRATIONS SIGNALS IN [0,14.5Hz] ;(B): THE VIBRATIONS SIGNALS IN [0,30Hz] .....	101
FIGURE.6.12: THE VIBRATIONS SPECTRUM IN THE PRESENCE OF PLANET DEFECT IN THE FREQUENCY RANGE [250Hz, 980Hz] .....	102
FIGURE.6.13: THE ACOUSTIC PRESSURE SPECTRUM (BLUE: HEALTHY CONFIGURATION; RED: THE PRESENCE OF PLANET DEFECT).....	103
FIGURE.6.14: THE ACOUSTIC PRESSURE SPECTRUM IN THE PRESENCE OF PLANET DEFECT. (A): THE ACOUSTIC PRESSURE IN [12Hz, 14.5] ;(b) : THE ACOUSTIC PRESSURE IN[220Hz, 340Hz]; (c) : THE ACOUSTIC RADIATION IN [920Hz, 1000Hz].....	104
FIGURE.6.17: THE CURRENT SPECTRUM IN THE PRESENCE OF COMBINED DEFECT.....	106

FIGURE.6.18: THE REFERENCE SET AND AFTER DEGRADATION SET.(A):THE SUN ; (B) : ZOOM OF THE DEGRADATION IMPACT ; (C) THE WEAR IN THE LUBRIFICANT .....	108
FIGURE.6.19: THE REFERENCE SET AND THE DEGRADATION SET .....	108
FIGURE.6.20: THE CURRENT SIGNAL COMPARING BETWEEN THE CURRENT AFTER 40HOURS OF RUNNING AND 4 HOURS (A): [0Hz; 150Hz]; (B): [4Hz; 40Hz] ; (c) [90Hz; 140Hz] .....	109
FIGURE.6.21. THE KURTOSIS EVOLUTION FOR THE 40 HOURS TEST .....	110
FIGURE.6.22.: THE SUN SURFACE DURING THE TEST (A): THE SUN IN THE HEALTHY CONFIGURATION; (B): THE SUN AFTER THE INTENSIVE TEST.....	111
FIGURE.6.23: SUN MASS EVOLUTION DURING THE TEST.....	112
FIGURE.6.24: COMPARISON BETWEEN VIBRATION SIGNALS AT THE FIRST HOUR AND THE NINTH HOUR.....	113
FIGURE.6.25: THE VIBRATIONS FREQUENCY SPECTRUM; (A): ZOOM OF THE FREQUENCY SPECTRUM OF THE VIBRATIONS SIGNAL IN [0Hz,50Hz] ; (B) THE FREQUENCY SPECTRUM OF THE VIBRATIONS SIGNAL IN [0Hz,500Hz]; (B) THE FREQUENCY SPECTRUM OF THE VIBRATIONS SIGNAL IN [200Hz,300Hz] .....	114
FIGURE.6.26: THE VIBRATIONS FREQUENCY SPECTRUM .....	115
FIGURE.6.27: COMPARISON BETWEEN THE CURRENT SIGNAL INITIAL TEST AND AFTER 3 HOURS OF RUNNING SYSTEM. ....	116



# List of Tables

TABLE.1.1. NOMENCLATURE OF MODELS .....	12
TABLE.1.2. KEY FREQUENCY OF GEARS DEFECTS .....	15
TABLE.1.3. NDT TECHNIQUES.....	21
TABLE.2.1: THE KINEMATIC PARAMETERS .....	36
TABLE.2.2: THE KEY FREQUENCIES OF THE MECHANICAL SYSTEM .....	48
TABLE.2.3: MOTOR PARAMETERS .....	48
TABLE.3.1. THE MECHANICAL CHARACTERISTICS OF THE GEARED MOTOR .....	58
TABLE 3.2. THE MECHANICAL SYSTEM CHARACTERISTICS.....	58
TABLE.3.3: THE MECHANICAL SYSTEM PARAMETERS .....	59
TABLE.3.4: THE PARAMETERS OF THE MOTOR .....	61
TABLE.4.1. THE MOTOR'S PARAMETERS .....	68
TABLE.4.2: KEY FREQUENCIES IN PLANETARY GEARBOX .....	70
TABLE.6.1: FREQUENCIES (IN HZ) FOR EACH COMBINATION OF THE EXPRESSION: .....	100
TABLE.6.2: THE IMPACT OF THE SIZE AND THE LOCATION OF DEFECT OF THE INCREASE OF THE CURRENT AMPLITUDE.....	107
TABLE.6.3. THE HOURLY EVOLUTION OF THE SUN'S MASS .....	112



# Nomenclature

## Electrical system

r: subscripts for the rotor

s: subscripts for the stator

j: subscripts for the motor phase where  $j \in \{a, b, c\}$

R: subscripts for the Resistance

L: subscripts for the self-inductance

M: subscripts for the mutual inductance

i: subscripts for the current

v: subscripts for the voltage

$\psi$ : subscripts for the magnetic flux

$\omega$ : subscripts for the angular velocity

f: subscripts for the motor frequency

N: subscripts for the motor speed (rpm)

p: subscripts for the number of pairs of poles

$T_{cte}$ : the Constant load torque

$T_{per}$  : the magnitude of the load torque oscillation

$\omega_{per}$ : the angular frequency of the load perturbation

$f_{per}$ : The perturbation frequency

$T_{motor}$ : The motor torque

$\omega_r$ : the rotor velocity

$\theta_r$ : the mechanical rotor positions

$p$ : pole pairs

$s$ : slip of the asynchronous motor

$F_{rt}^{(R)}$ : rotor MMF in rotor reference frame ( $R$ )

$F_{st}(\theta, t)$ : The MMF of the stator

$B(\theta, t)$ : the air gap flux density

$\Lambda$ : the permeance

$B(\theta, t)$ : The phase modulation of the flux density

$\Phi(t)$ : the phase

$V(t)$ : The voltage introduces from the source

$I(t)$ : the current intensity

$R_s$  : the stator resistance  
 $i_{st}(t)$ : the current result from Stator MMF  
 $i_{rt}(t)$ : The current result from of the Rotor MMF  
 $i_{ij}$ : the current of the j phase  
 $\psi_{ij}$  : The magnetic flux of j phase.  
 $M_{as}$ : Mutual inductance between two phases of the stator  
 $M_{ar}$ : Mutual inductance between two phases of the rotor  
 $L_{as}$ : Self-inductance of the stator  
 $L_{ar}$ : Self-inductance of the stator  
 $M_{rs}$ : Maximum inductance between a stator's phase and a rotor's phase  
 $R_s$ : The stator resistance  
 $R_r$ : The rotor resistance  
 $L_s$ : the stator inductance  
 $L_r$ : The rotor inductance

### **Mechanical system**

s: subscripts for the sun gear  
 r: subscripts for the ring gear  
 c: subscripts for the carrier gear  
 t: subscripts for the test gearbox  
 r: subscripts for the reaction gearbox  
 $f_i$ : subscripts for the frequency of the  $i^{\text{th}}$  gear where  $i \in \{s, r, c, 1, 2, 3\}$   
 k: subscripts for the stiffness  
 M: subscripts for the mass  
 C: subscripts for the damping  
 $C_{em}$ : Subscripts for the electromechanical torque  
 $f_s$ : the sun frequency  
 $f_c$ : The carrier frequency  
 $T_{em}$ : The gear mesh period  
 $F_{em}$ : The gear mesh frequency  
 $f_{dp}$ : The defected planet frequency  
 $f_{ds}$ : The defected sun frequency  
 $F_{co}$ : The coincidence defect frequency

# General Introduction

Planetary gearboxes have been used in different industrial domains especially in applications that recommend large torque transmission, aerospace, and energy generation. These mechanical systems have been exposed to numerical simulations and experiments to define in behaviour and work on monitoring it.

In fact, planetary gears are exposed to a lot of excitations of vibrations and noise. These excitations can be internal such as rattling and bearing misalignment, specific to the actual running of the system, or external, associated with fluctuations in motor torque, load torque and speed. Scientific research is working on optimizing these components design and especially controlling its operating state using non-destructive techniques. The Non-destructive techniques have been the actual technological methods used in preventative maintenance without causing any functional or design damage on the system.

Therefore, due to the criticality of this system, monitoring it has become one of the biggest scientific and industrial concern. The presence of any gears defect impacts the dynamic behaviour of the electromechanical system and generates load perturbation.

Therefore, depending on the defects type, size, and localisation several techniques have been developed to monitor the electromechanical systems. Mechanical signals such as vibrations, acoustic emission and acoustic pressure have been among the non-destructive methods in investigating the gears state. These techniques depend most on the dynamic behaviour of the system and its response to any perturbations due to anomalies or malfunctioning.

However, measuring vibration signals inside the gearbox is impossible in some cases or very difficult because of the inaccessibility constraints in mounting the sensors. Also, it can be affected by noise associated with external perturbations. Besides, technical difficulties may arise due to the implementation of sensors on rotary parts and in difficult environments.

On the other hand, the motor current signature analysis (MCSA) can easily describe the behaviour of the electrical device and the mechanical system. Therefore, this technique can help to describe the status of the entire mechanical system.

The motor current signature analysis (MCSA) has been one of the recommended non-destructive techniques to monitor electromechanical systems for its accessibility advantages. Also, for industrial application, the current signal is considered more available and easier to track in the preventive maintenance routine.

Within this context, this thesis investigates the impact of gears defects in planetary gearboxes on the stator current signal using MCSA. The research work presented the MCSA method in two parts. First, the study was oriented to a numerical model that generates the electro-mechanical interaction between the gearbox system and the asynchronous motor. Using the same model, teeth crack has been implemented to study the impact of this defect on the motor current.

Second, experimental tests have been carried out. In the experiments the current signals have been recorded simultaneously with vibration signals and acoustic pressure in different operating conditions. The aim behind using different sensors is to elaborate a comparative study in condition monitoring terminology.

The thesis report is presented in six chapters as follows.

The first chapter is a fast loop on universal and broad terms, definitions and functions straightforwardly linked to the multidomain modelling of the planetary gearboxes and controlling defects techniques. This part of the work provided the bibliographical review.

The second chapter is dedicated to the numerical modelling of the gear systems and the electrical device. In this part the theoretical electromechanical interaction has been presented. Therefore, , a simple model of spur gears is used .The results are shared in order to validate and approve the electromechanical terminology defined.

In the third chapter, experimental investigations are done on the test bench using different sensors. This chapter is devoted basically into three main parts:

A first one will present a low speed testbench composed by a geared motor and helicoidal gears. A second part will give a detailed presentation of a planetary gearbox testbench. This system is driven by an asynchronous motor. In this chapter we defined all the measurements instrumentations related to each physical phenomenon involved in our research study.

The fourth chapter presents the numerical system used to model the planetary gearbox in chapter 2.A global electromechanical system formed of the asynchronous device and a torsional model of two planetary gearbox stages.

This part correlates the experimental results obtained from the stator current measurements to the numerical simulations. The results of the current signal were recorded in the time domain and transformed to the frequency domain using the Fast Fourier Transformation (FFT). In this section the signals present the impact of the gears' dynamic behaviour on the current in healthy configurations. The comparative investigation elaborated is essentially a qualitative study.

The stator phase current measured in different operating conditions is compared to the phase current obtained after applying the reverse Park transformation on the Simulated results.

One of the main objectives of this research is the study of the use of current signals in industrial maintenance. Therefore, in the fifth chapter, gears defects were implemented on one gear in order to investigate its impact on stator current. The experimental results were followed by simulations in presence of modelled gears defect. For the numerical modelling, a teeth crack is assumed by decreasing in the gear meshing stiffness in the concerned tooth.

The last chapter has been devoted to a comparison study between the vibrations level, Motor Current Signature Analysis, and the acoustic pressure. This part of work aimed to assess the efficiency of the stator current to describe the mechanical behaviour seen in different mechanical signals.

Finally, a conclusion and a summary are presented to generate the future ideas and future work.



# **Chapter 1:**

## **Bibliographical Review**



# Chapter 1: Bibliographical review

## 1. Introduction

Before strengthening technical studies, basic knowledge is a fundamental step in research and development studies. This chapter focuses on basic headlines that are primordial for numerical methods of multiphysics modelling of planetary gears and basic techniques to detect gears defects. Gears are rotating mechanical components used for the transmission of the movements also in several domains like aeronautics, big industries, automotive ...etc.

The shaped geometry of the teeth in gears are meant to minimize wear, vibration, and noise, and to maximize the efficiency of power transmission. Therefore, studies are devoted between working on the kinematic of gears and investigating its dynamic behaviour. Planetary gears (PG) are widely used for its high-power density that it can achieve comparing with compacted size. Planetary gears involve 3 families of gears: a sun gear (S), planet gear (P) and a ring gear (R) (the internal gear), and a carrier (C) as seen in figure.1.1. This type of gearbox possesses an axi-symmetric configuration and equally spaced planets. With these two characteristics, the radial forces created at the mesh of each gear set balance each other. This balancing phenomenon is taking place only in the ideal cases considering that the manufacturing system is perfect and does not present any errors transmissions.

So, the radial bearing forces are zero. Furthermore, the input load sharing in planets reduce the gear loads. Finally, the self-centring capability of planetary gear sets tends to reduce many effects of manufacturing errors. The gearbox is driven by induction motors. As any Electro-mechanical system, gearboxes are exposed to mechanical defects. These defects can affect the performance of the system.

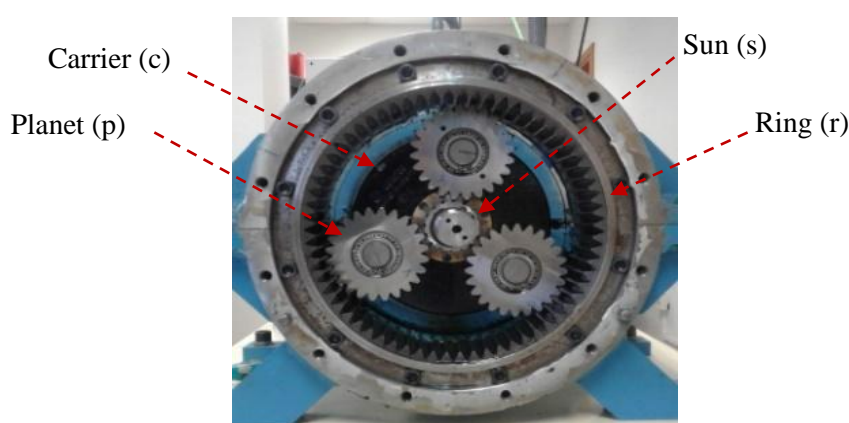


Figure.1.1: Planetary gearbox

This chapter presents two important parts: the first part is dedicated to defining the general field of the work in terms of multidomain modelling of electromechanical systems based on gears. Also, a second axis is orientated to gears defect and monitoring it.

## 2. Dynamic modelling of electromechanical systems

The mechanical sets are always driven by electrical systems. This electromechanical system is always exposed to malfunctioning and anomalies. Sometimes, in systems with complicated design, it turns to be difficult to monitor the mechanical and the electrical part separately. Therefore, using the electrical signals to investigate the behaviour of the gears would facilitate the condition monitoring study. Hence, investigating the behaviour of electromechanical systems depends on the approaches used in modelling.

### 2.1 Dynamic modelling of asynchronous motors

Modelling the electromechanical system is an essential step for these machines diagnosis. In fact, it presents the basics models and parameters that helps to better understand the state of the machine through its behaviour. It is distinguished both analytical and numerical. Analytical methods are based on the development of equations that describes the physical phenomena generated in the system. These equations describe both static and dynamic behaviour depending on the operating conditions and the target of the development. Numerical models are based on more complex equations that can describe more than one physical phenomena.

#### 2.1.1 Analytical models of asynchronous machines (dq transformation)

Modelling the electrical machine has been a tool whether to study the machine state or to ensure the physical coupling between motor and any mechanical system. The model used depends on the application [1]. Thus, the objective of this study is to investigate the state of the mechanical system. These models aim to determine the indicators of mechanical defects constructed from the electric quantities. It can be analytical or digital.

Indeed, the analytical methods are based on the establishment of analytical equations to describe the behaviour static or dynamic electric of a machine in steady state or transient. On the other hand, numerical methods use on nonlinear partial differential equations and with variable coefficients over time. The implementation of these methods is complex, but they are very precise since they consider many phenomena in the machine. Each of these methods presents advantages and disadvantages and the choice depends on the accuracy of the desired results.

The Direct-quadrature-zero transformation (dq0) is an analytical method that aims to transform a three-phased machine into a bi-directional maintaining the physical phenomena. Since this method recommends theoretical development of equations, it is necessary to make the following assumptions to simplify the complexity of the system:

- The saturation is neglected: the own and mutual inductances are independent of the currents flowing in the different windings.

- Hysteresis and Eddy currents are not considered in the magnetic parts because it is assumed that the magnetic circuit is perfectly laminated.
- The notches are supposed to be infinitely thin in order to neglect the notches effect.
- Magnetomotive forces are sinusoidally distributed in the air gap and are assumed uniform; there is symmetry with respect to the magnetic axis of the windings.

The analysis of the signature of the stator currents are carried out with the aid of several techniques, which the most used models are those based on the Park transformation. The purpose behind this theory is to give a mathematical model of conventional electrical machines to study its behaviour. Three-phase asynchronous machine bipolar consists of a fixed inductor (stator) and a rotating armature (rotor) each provided with a three-phase winding (the imaginary rotor winding represents the cage of squirrel consisting of conductive bars short-circuited by two rings to ends).

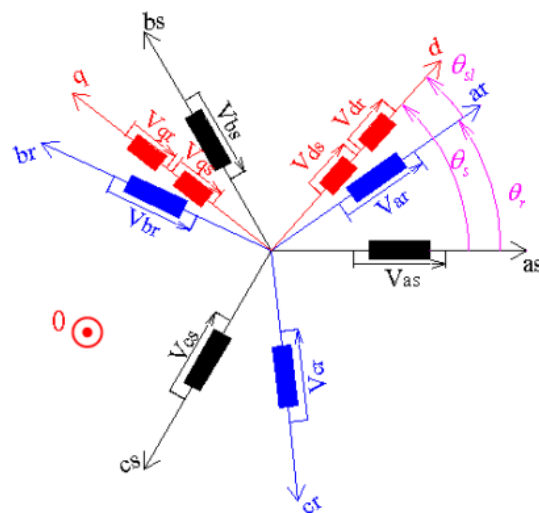


Figure.1.2: Schematic representation of the magnetic axes of the asynchronous machine [1]

The three stator phase windings as, bs and cs as they are schematically represented by the respective magnetic axes in the figure.1.2, as well as the three rotor windings ar, br and cr. Two perpendicular axes d (direct) and q (in quadrature) are also represented defining a new orthonormal frame. In the dq0 frame the electrical and magnetic equations of the asynchronous machine will be expressed more simply through a transformation into function of the angles between the different axes of the machine.

This change of variables can be interpreted as the substitution of real windings by fictitious windings (ds, qs, 0s, dr, qr and 0r) whose magnetic axes are connected to the axes d, q and 0, but whose conductors remain bound to the reinforcements that support them. The matrix that ensures this transformation is given by expression below.

$$T_{dq0/abc} = \sqrt{\frac{2}{3}} \begin{bmatrix} \cos \theta & \cos(\theta - \frac{2\pi}{3}) & \cos(\theta + \frac{2\pi}{3}) \\ -\sin \theta & -\sin(\theta - \frac{2\pi}{3}) & -\sin(\theta + \frac{2\pi}{3}) \\ \frac{1}{\sqrt{2}} & \frac{1}{\sqrt{2}} & \frac{1}{\sqrt{2}} \end{bmatrix} \quad (1.1)$$

Where  $\theta$ : is the angular position of the rotor with respect to the stator and  $X$  is the nominal scale,  $X_i$  are the scale in the dq0 frame.

There are three types of frames that depend on the application [2]:

**A) Frame (d, q) connected to the stator:**

$$\begin{cases} \omega_s = \frac{d\theta_s}{dt} = 0 \\ \omega_r = -\omega \end{cases} \quad (1.2)$$

This frame, connected to the stator, is used to study of launch and braking of the motor.

**B) Frame connected to the rotor:**

$$\begin{cases} \omega_s = \frac{d\theta_s}{dt} = \omega \\ \omega_r = 0 \end{cases} \quad (1.3)$$

This frame is connected to the rotor. It used for studying transients' regimes in asynchronous and synchronous machines.

**C) Frame connected to the rotating field:**

$$\begin{cases} \omega_s = \omega_e \\ \omega_r = \omega_e - \omega_s \end{cases} \quad (1.4)$$

Finally, this frame is the most known. It is used to carry out the vector control because the magnitudes of setting become continuous.

**2.1.2 The semi analytical models of asynchronous machines (Permeances networks)**

Comparing to the analytical methods, semi analytical methods take into consideration different physical phenomena such as saturation and notches harmonics. These methods are recommended in motor's defects studies. The most used semi analytical methods: The coupled Inductors [3], which simulate the coupling phenomena between inductances. Second model is the permeance networks. This model is used mostly in studying the dynamic behaviour of the electrical devices and monitoring it.



### 2.1.3 The Numerical models of asynchronous machines (Finite Element Method)

The Finite element method (FEM) has become the most used tool for computing the magnetic fields in electrical machinery. Such numerical techniques enable the designer to study the problems that are difficult to be solved by analytical methods.

This method is consisted of discretising the machine in 2D or 3D model, depending on the degree of complexity of the problem. The Finite element model is based on Maxwell that defines the relationship between the magnetic field and the electric field.

$$\text{div}(\vec{B}) = 0 \quad (1.6)$$

$$\overrightarrow{\text{rot}}(\vec{E}) = -\frac{\partial \vec{B}}{\partial t} \quad (1.7)$$

$$\overrightarrow{\text{rot}}(\vec{H}) = \vec{E} + \frac{\partial \vec{D}}{\partial t} \quad (1.8)$$

$$\vec{B} = \mu_0 \mu_r \vec{H} \quad (1.9)$$

$$\vec{J} = \sigma \vec{E} \quad (1.10)$$

Where:

$\vec{B}$ : magnetic induction field.

$\vec{H}$ : Magnetic field

$\vec{J}$ : Conduction currents

$\vec{E}$ : Electric field

$\vec{D}$ : Electric induction field

$\mu_r$ : The relative permeability of the material

$\mu_0$ : The air permeability

Even with simple 2D models, Finite element methods require important resolution time for low frequencies. Therefore, very important simulations time is needed in order to reach the steady regime. For the Finite Element method, the geometry of the machine is an essential input so it must be properly defined. The choice of the method to model the electric device depends essentially on the available inputs, the objective of the modelling and the degree of complexity of the problem.

## 2.2. The dynamic modelling of the planetary gears

As any system, to describe the dynamic behaviour of the gears we distinguish two main models, which are theoretical lumped models (LPM) and Finite Element Method (FEM).

### 2.2.1. Lumped parameters models of gears

According to Nevzat Özgüvzn and R. Houser in their paper [7], five classifications were distinguished:

#### Simple dynamic factor mesh:

Tuplin has introduced the first dynamic model constitute of spring-mass [8,9]. In this model an equivalent constant mesh stiffness was considered, and gears errors were modelled by the insertion and withdrawal of wedges with various shapes at the base of the spring. Thus, the dynamic loads due to transient excitation were approximated for various forms of errors. As the problem was considered as a transient excitation problem disregarding the periodicity of the excitation, this simple spring-mass model can be used to estimate dynamic factors only at conditions well below resonance. The dynamic model employed by Tuplin is shown in Figure.1.5.

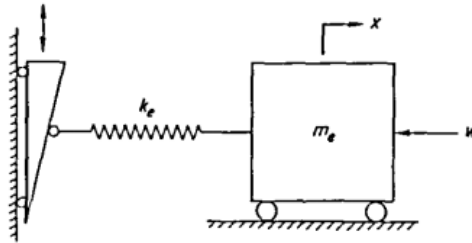


Figure.1.5: Dynamic model used by TUPLIN (mass- spring) [8]

#### Models with Tooth Compliance:

The basic characteristic of this model is that the only compliance considered is due to the gear tooth and that all other elements have been assumed to be perfectly rigid.

In this group, we distinguish two models as studied in the work elaborated by [10,7]

- A single tooth model: the objectives usually are tooth stress analysis
- A tooth pair model: the focus is mostly **contact stress** and **meshing stiffness analysis**. (Our case)

The resulting models are torsional or translational models. The translational models shown in the figure.1.6 aimed to study the forced vibrations of the teeth where the tooth of a gear itself is considered as a cantilever beam. Whereas the torsional models developed in figure.1.7 are meant to study the torsional vibrations of gears in mesh.

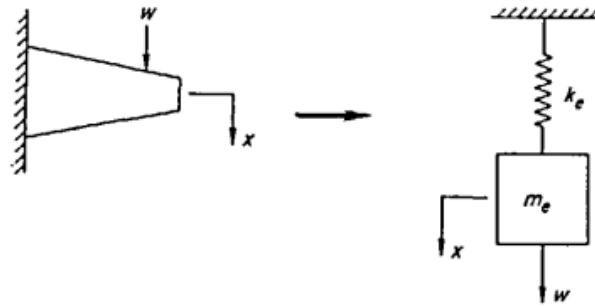


Figure.1.6: General model of gear tooth [8]

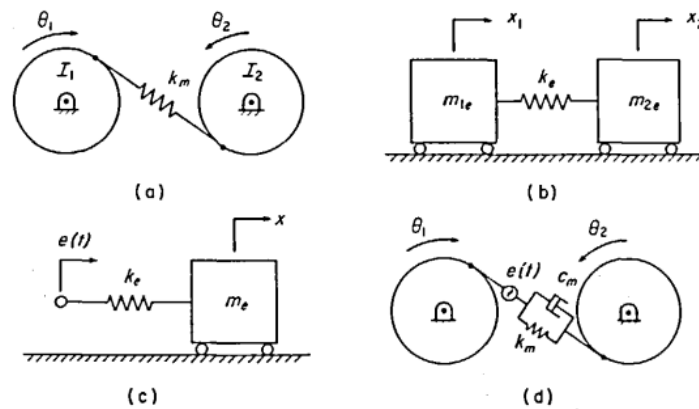


Figure.1.7: Some torsional models with tooth compliance [8]

Where all the parameters seen in figure.1.7 as illustrated below in table.1.1

Table.1.1. Nomenclature of models

<b>I<sub>i</sub></b>	Mass moment of inertia of gear i
<b>w</b>	Transmitted load
<b>M<sub>i</sub></b>	Equivalent mass of inertia I <sub>i</sub>
<b>M</b>	Equivalent mass of all inertias
<b>K</b>	Equivalent tooth mesh stiffness
<b>Em</b>	Tooth mesh damping
<b>e(t)</b>	Displacement input representing gear errors

The configurations (b) and (c) present torsional models in their translational models. In such models the system is idealized as a pair of inertias coupled by a spring which permits relative motion (d).

### 2.2.2. Planetary gear dynamic modelling:

In most of the research papers, planetary gears are modelled as it is presented in figure.1.8. Each component is considered as a rigid body able to translate in two directions, and to rotate around its rotational axis.

Chaari et al. [11] have worked on that model with model had **18 Degree of freedom**, obtained according to  $3N+9$  with N is the number of planets. (Three DOF per node).

Mathematically this model is described by the motion equation given by expression (1.11)

$$M\ddot{q} + (C_b + C_m)\dot{q} + (K_b + K_e(t))q = F(t) \quad (1.11)$$

Where:

q is the degree of freedom vector

M is the mass matrix

$C_b$  is the bearings damping matrix

$C_m$  is the mesh damping matrix

$K_b$  is the bearings stiffness matrix

$K_e(t)$  is the mesh stiffness matrix

F(t) is the external force vector applied on the system

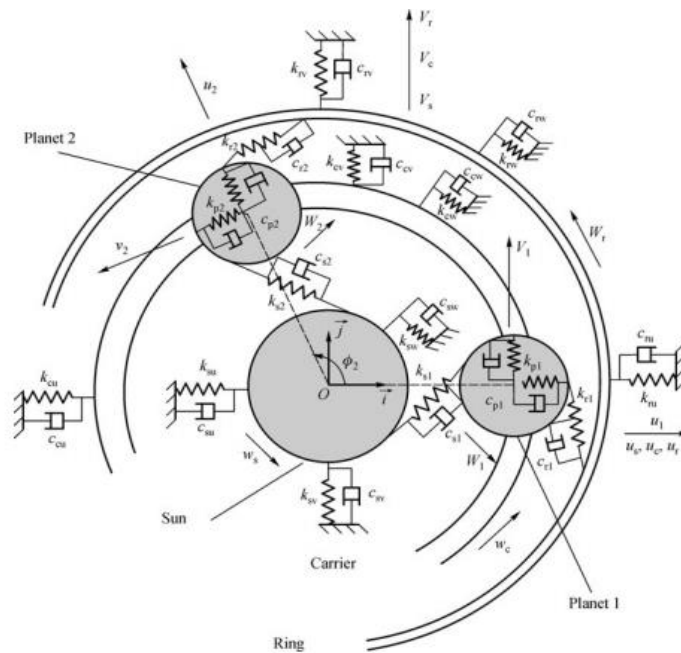


Figure.1.8: Planetary gear dynamic modelling [11]

Damping is called to characterize the energy dissipation. Some researchers have used in modelling damping phenomenon the Rayleigh, the viscous damping called also “Rayleigh damping” is mass-proportional and stiffness-proportional as it is shown in the expression below:

$$[C] = \alpha[M] + \beta[K] \quad (1.12)$$

With:  $\alpha$  and  $\beta$  are two constants elaborated by Dhatt [12].

Another model of damping can be used. This model is based mainly on the equivalent viscous modal damping. Al-shyyab *et al.* in their work [13] assume that the damping mechanisms at the gear meshes and bearings of a planetary gear set are difficult to model so they introduce viscous gear mesh damping elements to represent the energy dissipation of the system.

### 2.2.3. Finite element modelling of Planetary gearbox

The finite element model has been developed to accomplish the limitation of the LPM. The gears are considered in simulations as a deformable component. These assumptions will help to present a more accurate result of the behaviour of the gear [14] Yuksel and Kahraman employed this finite element model to study tooth wear and its impact on the dynamic behaviour of a planetary gear.

## 3. The gears defect

Gears are a mechanical component exposed to different types of defects depending on its functionality and location.

### 3.1. Gears defects classification

According to Chaari *et al.* [15], gear defects can be classified into geometry and tooth failure as it is illustrated in the figure.1.9. Geometry failure includes defects and assembly errors, whereas tooth errors are due to occur during running. This family of errors is decomposed divided into local damages and distributed damage (ISO 10825 (ISO 10825, 1995) standard).

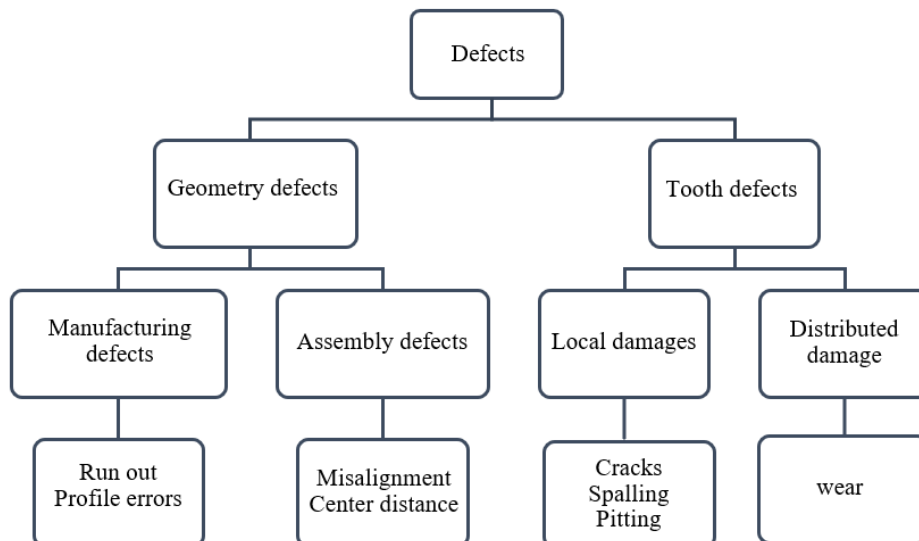


Figure.1.9: Gears defects classification [15]

The detection of the tooth defect is nowadays a real challenge for the scientific researchers and the industrial companies. This intense orientation is due to this defect size and difficulty of detection.

Therefore, the coming work will concentrate on the tooth damage, types and methods of modelling and detection. Each defect is characterized by a key frequency as illustrated in the table below.

Table.1.2. Key frequency of gears defects

Defect type	Defect localization	Frequency
<b>Local defect</b>	Planet defect	$f_{lpa} = \frac{z_s z_r}{z_p (z_r + z_s)} f_s$
	Planet defect (from both sides)	$f_{lpa} = 2 \frac{z_s z_r}{z_p (z_r + z_s)} f_s$
	Sun defect	$f_{lsd} = K \frac{z_r}{z_r + z_s} f_s$
	Ring defect	$f_{lrd} = K \frac{z_s}{z_r + z_s} f_s$
<b>Distributed defect</b>	wear-Planet defect	$f_{lpa} = \frac{z_s z_r}{z_p (z_r + z_s)} f_s$
	wear-Sun defect	$f_{csd} = \frac{z_r}{z_r + z_s} f_s$
	wear-Ring defect	$f_{crd} = \frac{z_s}{z_r + z_s} f_s$

**3.1.1. Local teeth damage**

**Pitting**

Pitting is caused by rolling contact or a mixed condition of rolling and sliding contact (ISO 10825, 2009). According to the ISO standard, pitting is characterized by small, scattered holes. According to Davis [16] the pitting process starts with a fatigue crack that initiates either at the surface or at a small depth just below the surface. When the crack grows, the surface loses a piece of material which results in a pit. A spall may then be formed if several small pits grow together into one single pit [16]. Pitting is a form of surface fatigue which may occur soon after operation begins.

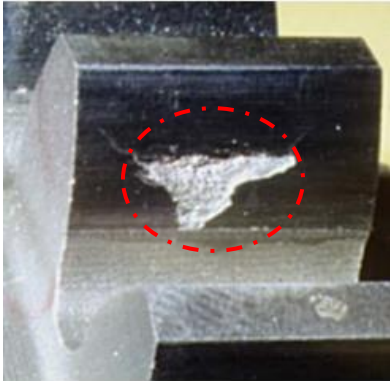


Figure.1.10: Pitting [17]

The impact of the pitting fault seen the figure. 1.10 can't be clearly seen in the time neither the frequency domain representations unless the fault severity is important.

### **Tooth breakage -Bending fatigue**

Spalling (or tooth breakage) is the initiation of crack that takes place at the weakest point, normally at the root of the tooth or at the fillet where high stress concentration exists together with highest tensile stress from bending or from the surface defects as shown in figure.1.11.

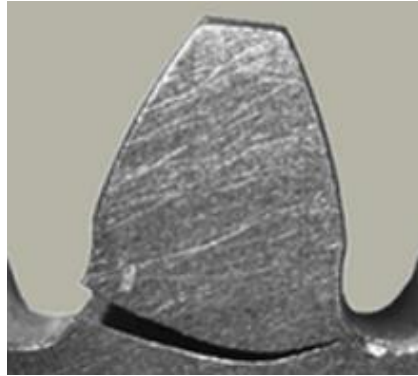


Figure.1.11: Breakage [17]

### **Case Crushing**

This type of defect is due to excessive compressive loads. It occurs in case-hardened gears when a crack propagates in the interface between the case material and the core material (ISO 10825, 2009). The crack initiates when subsurface stresses exceed the material strength of the subsurface material. Then it propagates along the interface between the case and the core until material is lost and a spall is formed. Case crushing can be avoided by increasing the case depth of the gear [18]. These kinds of problems are usually caused by cutting edge of a hob and the tooth flank work.

### **3.1.2. Distributed Damage**

#### **Abrasive wear**

Abrasive wear in gears is caused by hard particles which act as contaminants in the gear [19]. These particles have either been added externally or internally depending on the source of origin. If the contaminants have been added externally it might have been due to contamination from manufacturing or assembly. While internal contaminants may originate from pitting or wear. The abrasive wear is characterised by the removal of surface material.

#### **Scoring**

Scoring shown in the figure below is due to a combination of two distinct activities. First, lubrication failure in the contact region and second, establishment of metal-to-metal contact. Later, welding and tearing action resulting from metallic contact removes the metal rapidly and continuously so far, the load speed and oil temperature remain at the same level. The scoring is classified into initial, moderate, and destructive.

Scoring is considered one of the most common gear defects. It is like adhesive wear, seen above, but at an advanced stage. Scoring may be encountered in a short operating period, and it damages immediately the surface of gear [20].



Figure.1.12. Scoring [20]

**Scuffing**

Scuffing, referred also to as scoring, is a lubrication failure, frequently brought on by an increase in the operating temperature. The lubricant film breaks down, allowing metal-to-metal contact at high spots on the flank surfaces. Under sufficient conditions of load and temperature, this metal-to-metal contact causes asperities to weld together and then tear apart as the motion continues [21].

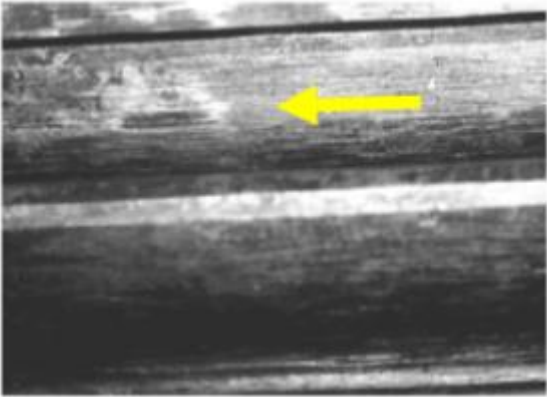


Figure.1.13: Scuffing [21]

**Plastic Deformation of the Teeth Surface**

Plastic flow of tooth surface results when it is subjected to high contact stress under rolling cum sliding action. Surface deformation takes place due to yielding of surface or subsurface material. The following figure illustrates the damage caused by the overheating associated with insufficient lubrication.

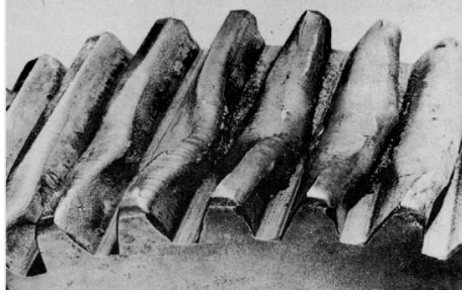


Figure.1.14: Overheating defect on a gear

### 3.2. Gear defects modelling

For the gears defect modelling, two types are distinguished: Analytical model of Finite Element Method.

#### 3.2.1. Analytical modelling

Gears defects are modelled in scientific research as a modification in the mesh stiffness function's shape and amplitude. The time varying mesh stiffness was investigated by several researchers. Chaari *et al.* [22] had developed an analytical model in order to quantify the reduction of the mesh stiffness due to a spalling and studied its dimensioning effects on the time varying mesh stiffness.

In the same context, Del Rincon *et al.* [23] also studied the effect of pitting on mesh stiffness function for an enhanced model gear. As developed in the work of Del Rincon *et al.*, the presence of a crack will lead to an amplitude and phase modulation of the gear mesh frequency. Besides it will generate high order harmonics, as a result of the stiffness modification in the affected tooth. Therefore, the inclusion of a crack in the model proposed affects the overall behaviour of the tooth.

In other research papers, the pit was modelled in elliptical shape in three different locations. They evaluated the influence of pitting on gear mesh stiffness using the finite element method. Recently, the influence of pitting on mesh stiffness function was studied by Liang *et al.* [24] who proposed an analytical method on mesh stiffness calculation based on potential energy method external spur gear. The model was validated through a finite element method. In their study, the pits are modelled in circular shapes, where the impact had been validated in three severity levels. Considering the effects of the gear tooth errors, Chen and Shao [25], also, had developed a general analytical model to analyse the influences of tooth profile modification. In this manner, Hui Ma *et al.* [26] had simulated the shape of a spilling by a symmetrical rectangle groove as seen in figure.1.15. When the tooth contact occurs in the scope of the spalling, the cross-section  $S_i$  will change from a rectangle to a gib.

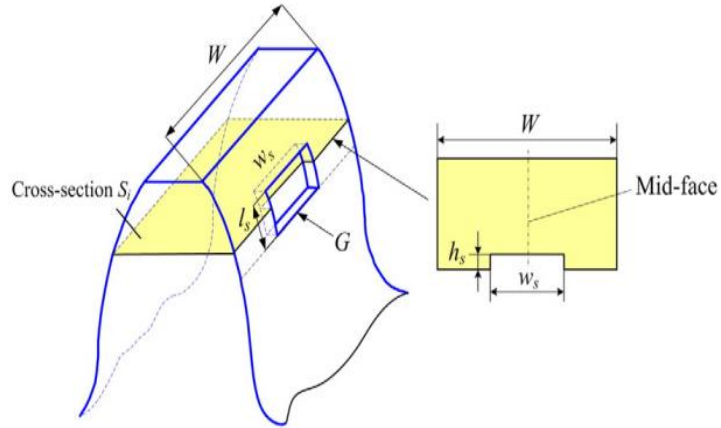


Figure.1.15: The shape of the spalling [26]

Where:  $W_s$  (spalling width) ,  $l_s$  :spalling length ,  $h_s$  is spalling depth.

The gear tooth is modelled as a nonuniform cantilever beam. In the figure.1.16,  $r_b$  denotes the radius of the base circle,  $\alpha_s$  denotes the pressure angle of the spalling starting position and  $\beta$  is the operating pressure angle. The mesh stiffness of single-tooth pair with spalling at meshing position j is written as follow [26]:

$$(k)_j = \left( \frac{1}{k_h} + \frac{1}{k_{t1}} + \frac{1}{k_{f1}} + \frac{1}{k_{t2}} + \frac{1}{k_{f2}} \right)^{-1} \quad (1.13)$$

where  $k_{ti}$  and  $k_{fi}$  ( $i = 1,2$ ) are the stiffness of tooth and fillet-foundation, respectively, here, subscripts 1 and 2 denote the driving gear and driven gear.  $k_h$  denotes the local contact stiffness. The stiffness of tooth  $k_{ti}$  can be expressed as:

$$k_{ti} = \left\{ \begin{array}{l} \left( \frac{1}{k_{bi}} + \frac{1}{k_{si}} + \frac{1}{k_{ai}} \right)^{-1} \\ \left( \frac{1}{k_{bsi}} + \frac{1}{k_{ssi}} + \frac{1}{k_{asi}} \right)^{-1} \quad \begin{array}{l} j \notin GD, i = 1, 2 \\ j \in GD, i = 1, 2 \end{array} \end{array} \right. \quad (1.14)$$

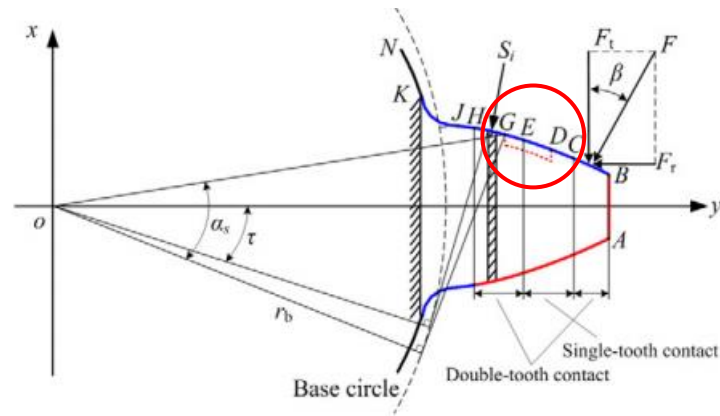


Figure.1.16: nonuniform cantilever beam modelling of tooth with spalling [26]

Besides the analytical method, finite elements have been used also to model teeth defects in several research works. Sfakiotakis et al. [27] have simulated the presence of cracks in gears as seen in figure.1.17. The behaviour of stress singularities is approximated by quarter point elements and the stress intensity factors are evaluated by displacement formulas. This generalised formulation efficiently approximates the load sharing and thus permits the evaluation of the dynamic stress intensity factors along the path of contact, for any crack appearing in spur gear drives. In the affected area, the type of meshing will be concentrated and more refined to better simulate and identify the defects impact.

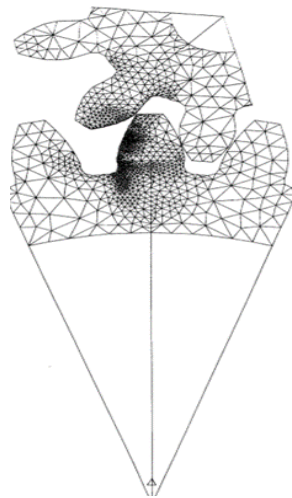


Figure.1.17: Modelling gear's crack using Finite element method [27]

#### 4. Methods used in detecting gear defects

Detecting defects, especially in gearboxes, by non-destructive techniques have been widely the centre of interest of industries and researchers due to its accessibility without damaging the component. According to the norms NF EN ISO 9712 August 2012, the main Non-destructive testing used nowadays are presented in table.1.3. The most common used methods are those based on Vibrations signals, acoustic signals and motor current signal analysis.

Table.1.3. NDT techniques

<b>NDT Technique</b>	<b>Abbreviation</b>
<b>Acoustic Emission Testing</b>	(AE)
<b>Electromagnetic Testing</b>	(ET)
<b>Guided Wave Testing</b>	(GW)
<b>Ground Penetrating Radar</b>	(GPR)
<b>Laser Testing Methods</b>	(LM)
<b>Leak Testing</b>	(LT)
<b>Magnetic Flux Leakage</b>	(MFL)
<b>Liquid Penetrant Testing</b>	(PT)
<b>Magnetic Particle Testing</b>	(MT)
<b>Neutron Radiographic Testing</b>	(NR)
<b>Radiographic Testing</b>	(RT)
<b>Thermal/Infrared Testing</b>	(IR)
<b>Vibration Analysis</b>	(VA)
<b>Ultrasonic Testing</b>	(UT)
<b>Visual Testing</b>	(VT)

#### **4.1.Vibration signals**

Vibration signals have been used basically for characterising the dynamic behaviour of the rotating machinery and orientated to several uses such as systems monitoring. The geometrical defect will cause load fluctuation, which itself consists of an additional source of vibrations. Therefore, vibrations frequencies will appear in the frequency spectrum extracted from the temporal signal.

In experiments the vibration level in the mechanical system is recorded using accelerometers. These accelerometers are placed in contact with the concerned component as seen in figure.1.18. The vibration signals in this testbench were obtained from a 2D accelerometer (Analog Devices Inc.-ADXL210JQC) mounted on the gearbox frame. The output of these tests elaborated by Amir *et al.* [28] aims to detect the existence of gear defect by analysing the vibrations spectrum.

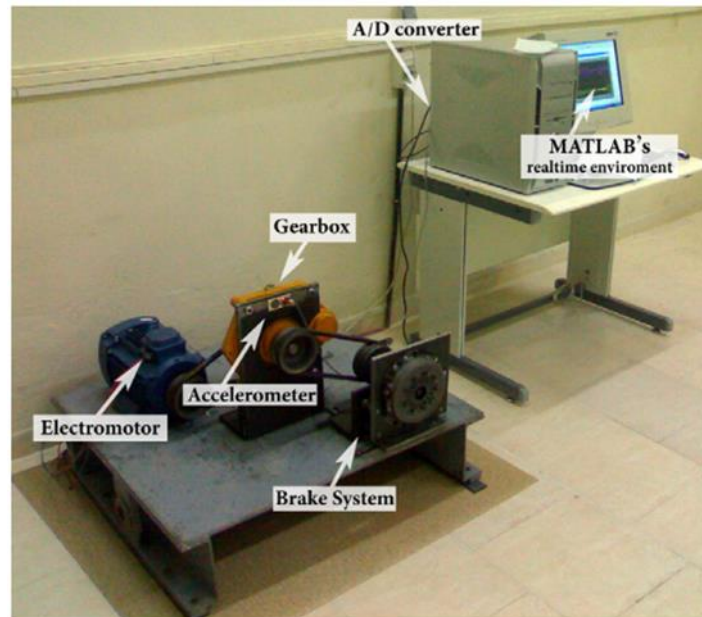


Figure.1.18: The experimental setup test-Acoustics Research Lab., Amir kabir University of Technology [28]

In recent years some interesting approaches based on using vibration signals for condition monitoring rotating machinery were developed. Within this context, Chaari *et al.* [29] have worked on modifying the mesh stiffness to simulate the pitting impact on the dynamic response of planetary gears. Monitoring the gear status takes into consideration non-stationary conditions such as variable load and variable speed in applying nonstationary conditions, it is proposed to use order analysis instead of classical spectral analysis [30].

Many researchers have focused on planetary gear modelling, such as Al-shyyab and Kahraman [31] who have presented a non-linear dynamic model for planetary gear sets. Inalpolat *et al.* [32] developed a model to investigate modulation sidebands seen in the frequency spectrum. These results are validated by experimental measurements. On the other hand, Zimroz *et al.* [33] had introduced a new diagnostic feature which is used for monitoring planetary gearboxes under varying external load conditions. The recognition of the gear defect in the frequency spectrum is easy to identify since each defect is characteristic by its key frequency.

Song *et al.* [34] had investigated the gear defect on different components by creating models using the finite element. The models were used also to calculate the resultant gear mesh stiffnesses, which were incorporated into the planetary gear model later to obtain the faulted vibration signal.

For the planetary gearbox, Ayoub *et al.* [35] had investigated the impact of a crack on one of the planets on the spectra of the acceleration of the test ring as seen in the results in figure.1.19.

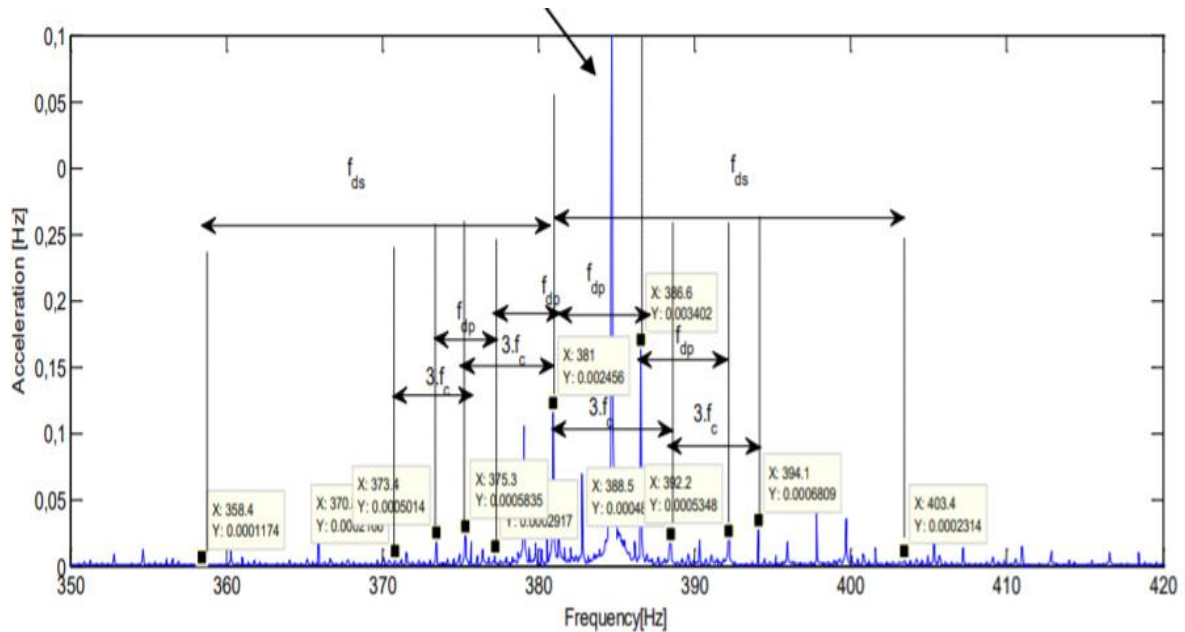


Figure.1.19: The spectra of the accelerations signal of the test ring [35]

The vibration signal clearly shows the impact of the gears defect on the acceleration spectra through the appearance of the defect's frequency in the spectrum. Vibration analysis was extensively used to investigate gears in different conditions and in defect detection. However, measuring vibration signals inside the gearbox is impossible in some cases or very difficult because of the inaccessibility constraints in mounting the sensors [36].

Firstly, vibration signals can be affected by noise associated with external perturbations. Besides, measurements are sensitive to the sensor positions. Also, Technical difficulties may arise due to the implementation of sensors on rotary parts and in difficult environments like high temperatures, limited space, or access for instance.

#### 4.2. Acoustic emission (AE)

The source of acoustic emission (AE) is attributed to the release of stored elastic energy that manifests itself in the form of elastic waves that propagate in all directions on the surface of a material. For gears, Tandon and Mata [37] applied AE to a spur gears test rig with a jet oil lubrication system to investigate the detectability of gear pitting damages. Their investigation has shown the advantage of AE over vibration for early detection of defects in gears by observing that the AE data displayed a sharp increase in the parameters when the defect size was around 500  $\mu\text{m}$ , while vibration data did not display a comparable increase until the defect size was more than 1 ,000  $\mu\text{m}$ .

Furthermore, AE is not affected by structural resonances and typical mechanical background noise (under 20kHz) [38]. The problem with the AE signal is that it is still challenged by the attenuation of the signal so that as such the AE sensor must be close to its source. To create the elastic wave without exciting it, the gear was under load and attached to sensors which will receive the acoustic wave. In fact,

when an unknown fault starts to form in any machinery, energy loss activities such as impacts, friction and crashing generate sound wave activity that spans a broad range of frequencies.

For gearbox, backlash and contact ratio are the major causes contributing to an excessive contact stress and gear's noise. They determine the vibration and acoustic emission. The figure.1.20 describes the dispositive required to detect any acoustic emission related to the presence of any defects. Starting with sensors which are used to capture the AE generated by cracks. The defects' frequencies are too low, which recommend the preamplifiers use. The preamplifiers are amplifiers that prepare a small electrical signal for further amplification or processing. They are typically used to amplify signals. The Acoustic signal will be collected and saved in an acquisition system and will be displayed later on software dedicated to do so.

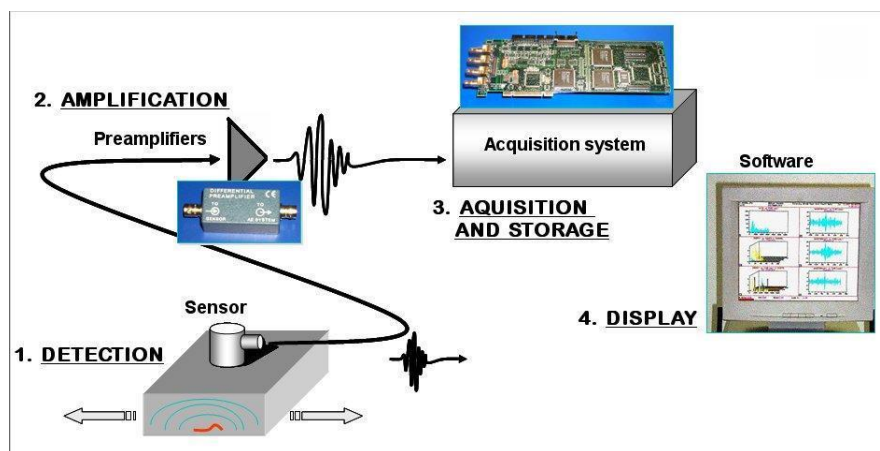


Figure.1.20: AE process treatment [38]

As for the methods of processing the acoustic emission signals of rotating machinery, there are parameter analysis methods and waveform analysis methods. The former ones are dominated by methods based on basic parameters such as the ring, energy, and amplitudes; compared with the original waveforms of signals.

However, these parameters lose massive information and have difficulties in characterising the essence of defects. Technicians have done a lot of research on waveform analysis methods. By building a theoretical model, Bashir simulated the acoustic emission energy which was sent upon the extension of the fine cracks on the rolling bearings in a helicopter gearcase. The impact of cracks could be tested in real time, and the bearing faults could be detected before surface materials were peeled off [39]. McFadden employed acoustic emission sensors to test the signals of angular contact thrust bearings under low-speed rotation. It has been noticed that, in low-speed rotation, the acoustic emission sensors could detect signals induced by the concentrated load of rolling elements [40]. Mba et al. distinguished the types of bearing faults using the acoustic emission technique and auto-regressive coefficients. They obtained substantial results, but did not validate them in practice [41,42].

### 4.3. Acoustic radiation

The acoustic radiation is the energy released moved outward along radial lines for important distances compared to the size of this wave’s source. Radiation involves not only the waves, but also their physical source and their interaction. Hence, this technique is now used in the condition monitoring of rotating machinery. Although acoustic radiation is recommended in several research studies for its great utility and interesting results, it is rather complicated. Abbas et. al [43] have worked on a gearbox’s model seen in the figure 1.21, based on FE approach which was developed to calculate the gearbox-radiated sound associated with the changing stiffness of the meshing teeth.

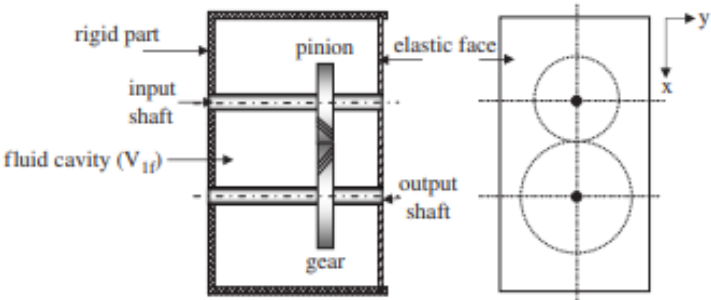


Figure.1.21: Experimental dispositive [43]

For the computation of the noise radiated by the elastic face of the gearbox, Helmholtz integral will be used to develop the Rayleigh integral method combined with the structural Finite element (FE) model. Numerical study in the paper of Abbas et al., has proved that the acoustic field depends on the geometrical dimensions, on the vibrational distribution of the elastic face and also on the resonance of the whole gearbox.

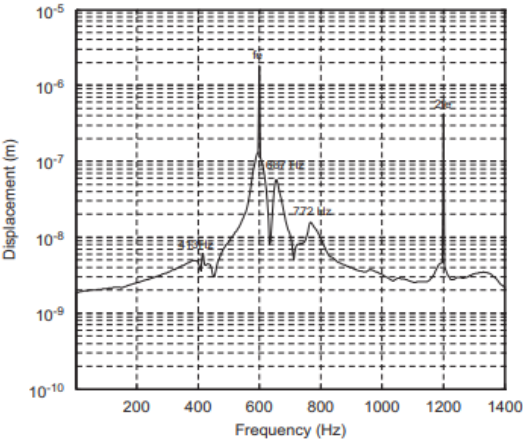


Figure.1.22: Pressure spectrum observed in the centre of the fluid cavity [43]

For the experimental tests, acoustic sensors in the acoustic emission are replaced by microphones which will receive the acoustic pressure around the gearbox. According to the work presented by Kato and al

[44] in their book “Acoustic Radiation Efficiency Models of a Simple Gearbox”, the sound power radiated from the gearbox was measured by using an acoustic intensity probe consisting of a pair of phase-matched microphones mounted face-to-face and spaced 6 mm apart as explained in the figure 1.23.

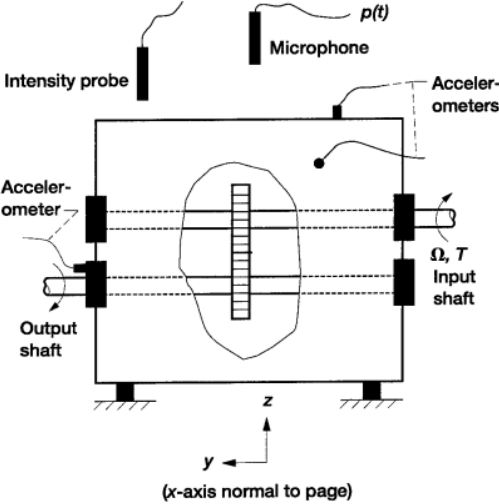


Figure.1.23: Experimental set-in presence of microphones [44]

The probe was positioned with the aid of a computer-controlled robot (RO). The robot was commanded to move the probe to 20 locations, each approximately 60 mm above the top of the housing. The 20 intensity spectra were averaged and multiplied by the area of the top of the housing to yield the radiated sound power at that operating condition. Figure.1.24 below shows the sound power spectrum for speed  $Q = 6000$  rpm and torque  $T = 68$  N-m. Here, the mesh frequency is 2800 Hz, and the shaft frequency is 100 Hz. In the spectrum some of the sidebands have significant amplitudes relative to the mesh frequency peak. A characterization of the sound power should include three pairs of sidebands in the computation.

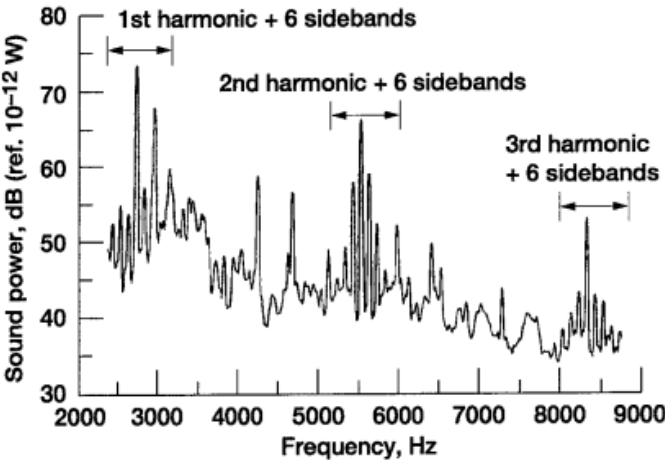


Figure.1.24: Frequency spectrum of sound power [44]

#### 4.4. Motor Current Signature Analysis (MCSA)

For the most common cases, gearbox is driven by an asynchronous motor, squirrel-cage type as it is presented in the figure.1.25.

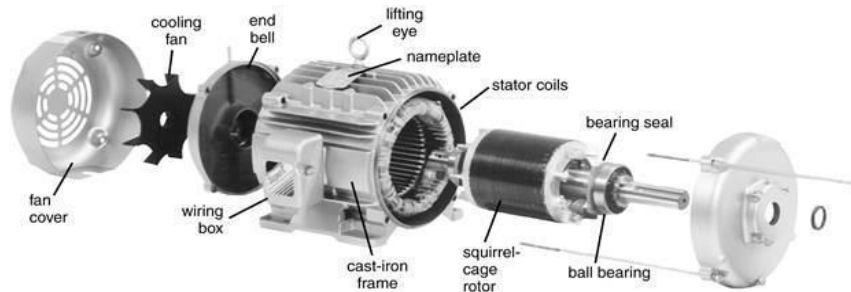


Figure.1.25: Asynchronous motor [45]

The motor current signature analysis method depends on measuring the stator current of the asynchronous motor on defecting the behaviour of the connected system as described in the figure.1.26.

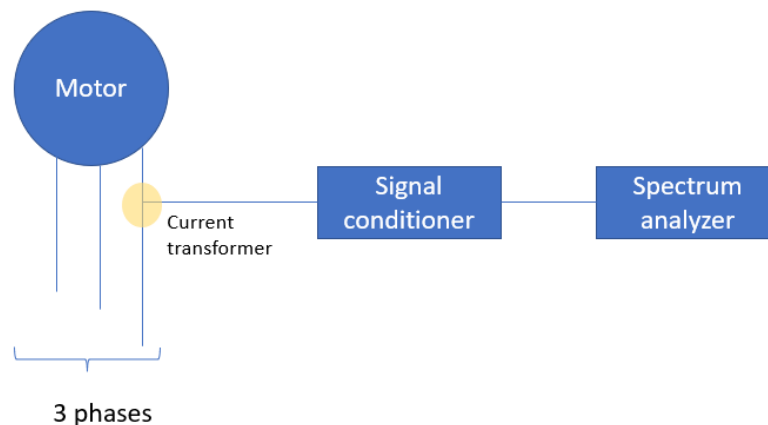


Figure.1.26: The stator phase current recording

In the existing researchers, detecting gearbox defects by experimental investigations are done by directly stator current measurements and each time it depends on equipment presented. Ottewill *et al.* [46] has worked on detecting the tooth profile faults in epicyclic gearbox and well presenting the results by passing by the synchronously averaged motor current. In that work, the motor currents from each phase were measured by ABB EL55P2 current sensors and recorded by a NI 9203 card. It was shown experimentally that a tooth defect introduced will excite a transient oscillation in measured currents. And with using the proposed synchronous averaging approach, it is possible to both identify a potential tooth fault and to highlight in which element in the gearbox the fault has occurred. Investigating the motor's behaviour was used in several studies to monitor the mechanical system, detecting defects. This Proposal was highlighted by the work developed by Balan *et al.* [47] studying the impact of the unbalance seen in the motor's component on the motor current signal.

Nowadays, the use of the electrical response of the motor in monitoring the rotating machinery is in a rising development. Several studies had worked on modelling the problem numerically in order to detect the rotating machinery defects. Nabih et al. [1] for example, have based the detection of gears fault on an electro-mechanical model that describes numerical modelling of both the transmission system and the asynchronous machine by the park transformation. In the same work, the stator current was used to highlight the presence of a tooth crack in the wheel. Aroua et al. [48] have used the angular approach modelling of induction motors for monitoring. The aim of this research work is to gain understanding of the interaction between Multiphysics subsystems, mainly in faulty cases

The analysis of the signature of the stator currents has traditionally been used to monitor induction motors and their bearings. This method has been used as a testing and analysis technique to improve the assessment of bearing wear during the operation of motors installed in inaccessible places. Several studies have shown that the analysis of the signals of the stator currents can be able to detect, differentiate, and track the progress of abnormalities such as tooth defects in the case of a wheel and worm transmission. The modelling of electromagnetic systems represents an important step in the diagnostic methods of these systems. It is a question of defining the appropriate models that allow the electromechanically analyses.

These models aim to determine the indicators of mechanical defects constructed from the electric quantities. It can be analytical or digital. Indeed, the analytical methods are based on the establishment of analytical equations to describe the behaviour of static or dynamic electric of a machine in steady state or transient. On the other hand, numerical methods are based on nonlinear partial differential equations and with variable coefficients over time. The implementation of these methods is complex, but they are very precise since they consider many phenomena in the machine. Each of these methods presents advantages and disadvantages and the choice depends on the accuracy of the desired results.

The analysis of the signature of the stator currents are carried out with the aid of several techniques, of which the most used models are those based on the park transformation. The purpose beyond this theory is to give a mathematical model of conventional electrical machines to study them in steady state or transient. Three-phase asynchronous machine bipolar consists of a fixed inductor (stator) and a rotating armature(rotor) each provided with a three-phase winding (the imaginary rotor winding represents the cage of squirrel consisting of conductive bars short-circuited by two rings to ends).

The use of the current signal to investigate the gearbox state is considered more accurate given the accessibility for different operating conditions and complex systems. This is one additional advantage compared with the vibration signals, since in the stator current, the modulations produced by the planet motion do not appear [49], which makes the spectrum more significant. Different research papers [49,50] had proved the sensitivity of this method not only to detect the state of the system but also to localize and identify the defect. Nandi et al. [50,51] had used the motor current signal analysis MCSA

to show that the appearance of the static and dynamic air gap eccentricity simultaneously is seen in the amplitude modulation of the stator current. Kia [52] had developed the idea of using the current of the driving machine to detect a mechanical system defect.

## 5. Signal processing techniques

Basically, the experimental data needs the pass by signal processing techniques, which are used for filtering and improving signal transmission fidelity. These techniques are meant to emphasise or detect components of interest in a measured signal. Choosing the appropriate technique depends on the domain of work. We distinguish mainly time domain indicators and the time -frequency domain.

### 5.1. Time domain

In the signal processing analyses we will be faced with several parameters which will define by itself the physical phenomena behind.

#### RMS

The root mean square (RMS:  $x_{rms}$  ) for a discretize sampled signal is defined as it is given below:[53]

$$x_{rms} = \sqrt{\frac{1}{N} \sum_{i=1}^N (x_i^2)} \quad (1.15)$$

Where:

N: the length of data set

$x_i$  the  $i$ -th element x

#### Crest factor:

The crest factor is the parameter sensitive to defect detection, such as the crack initiation. The crest factor CF is given by the expression below:

$$CF = \frac{|x|_{peak}}{x_{rms}} \quad (1.16)$$

With  $|x|_{peak}$  is the peak amplitude. In data the Cf should be seen an increase by the appearance of any crack. [53].

## Kurtosis

The kurtosis is used to see how peaky or how smooth the amplitude of data set  $x$ . If a signal contains sharp peaks with high values generated by a fault in the gearbox, it is expected that its distribution function will be sharper; the kurtosis of the fault signal should be higher than that of the healthy signal.

$$Kurt = \frac{N \sum_{i=1}^N (x_i - \bar{x})^4}{\left( \sum_{i=1}^N (x_i - \bar{x})^2 \right)^2} \quad (1.17)$$

Where  $x_i$  is the  $i$ -th element of  $x$ ,  $N$  is the length of the data set  $x$ ,  $\bar{x}$  is the mean value of the data  $x$

## 5.2. Time frequency Domain

### 5.2.1. Fast Fourier transform (FFT)

The Fast Fourier Transformation (FFT) is a mathematical operation that the signal from time domain representation to its equivalent frequency domain representation. The transformation is given by the equation:

$$X(f) = \int_{-\infty}^{+\infty} x(t) e^{2\pi i f t} dt \quad (1.18)$$

For a signal with constant energy the FFT is given by:

$$X(f) = \sum_{k=-\infty}^{+\infty} x(k) e^{2\pi i f k} \quad (1.19)$$

The signals analysis instruments utilise a Fast Fourier Transform (FFT) which is a special case of the generalised Discrete Fourier Transform.

### 5.2.2. The heterodyne technique

**Heterodyning** is a signal processing technique that creates new frequencies by combining or mixing two frequencies. Heterodyning is used to shift one frequency range into another, new one, and is also involved in the processes of modulation and demodulation [54].

In the most common application, two signals at frequencies  $f_1$  and  $f_2$  are mixed, creating two new signals, one at the sum  $f_1 + f_2$  of the two frequencies, and the other at the difference  $f_1 - f_2$ . These new frequencies are called **heterodynes**. Typically, only one of the new frequencies is desired, and the other signal is filtered out of the output of the mixer. The technique applied here is called heterodyne. Mathematically, heterodyning is based on the trigonometric identity. For two signals with frequency  $f_1$  and  $f_2$ , respectively, it could be written as:

$$\sin(2\pi f_1 t) * \sin(2\pi f_2 t) = \frac{1}{2} \cos(2\pi(f_1 - f_2)t) - \cos(2\pi(f_1 + f_2)t) \quad (1.20)$$

### 5.2.3. Wavelet transform method

The Wavelet transform is in fact an infinite set of various transforms, depending on the merit function used for its computation [55]. There are also many ways to sort the types of the wavelet transforms. Here we show only the division based on the wavelet orthogonality. We can use orthogonal wavelets for discrete wavelet transform development and non-orthogonal wavelets for continuous wavelet transform development. These two transforms have the following properties:

$$F(a, b) = \int_{-\infty}^{\infty} f(x)\psi_{(a,b)}^*(x)dx \quad (1.21)$$

The Fourier series does not work well when it must locally describe a function that shows some interruptions. Unlike the Fourier transform, wavelet analysis offers a wide range of functions of which one could choose the most appropriate for an application given.

### 5.2.4. Empirical mode decomposition (EMD)

The EMD method is a signal processing tool that decomposes any oscillating signal in finitely many parts, of decreasing instantaneous frequency. The originality of the method, compared for instance to a wavelet transform, is to be independent of fixed frequential filters: the signal decomposition is directly derived from the data. The empirical modal decomposition brings two novelties:

- It consists of a decomposition in an unfixed basis of the signal; it is self-adaptive.
- It is basically algorithmic, contrary to the analysis in components that require the computation of expensive matrices of covariance [56].

### 5.2.5. Time synchronous Averaging

Time synchronous averaging is a signal processing technique that extracts periodic waveforms from noisy data [57]. TSA is a fundamentally different process than the usual spectrum averaging that is generally done in FFT analysis. It is used to greatly reduce the effects of unwanted noise in the measurement. The waveform itself is averaged in a time buffer before the FFT is calculated, and the sampling of the signal is initiated by a trigger pulse input to the analyzer. The synchronous signal average,  $\bar{y}$ , may be given as below:

$$\bar{y}(\theta_{ave}) = \frac{1}{M} \sum_{m=0}^{M-1} y(\theta_{ave} + 2\pi m) \quad (1.22)$$

$y$  is the recorded signal to be analysed,  $M$  is the total number of averages to be performed and  $\theta_{ave}$  is the angular displacement of the signal to be averaged (modulo  $2\pi$ ). Ottewill and al [46] has used the synchronous averaging approach to extract an indication of the seeded tooth fault.

## **Conclusion**

The claim behind this chapter was to introduce a deep overview concerning the monitoring of the planetary gearboxes using multi domain techniques. In this state of the art, different methods of modelling planetary gearboxes and asynchronous machines were presented and highlighted. Still the challenge to overcome in this field is how to ensure a high performance, less noise produced, and a long service life with a moderate cost and ensuring the machines safety. All of the aforementioned parameters will be the fundamentals in all the dynamic studies presented later. In a global way, this research work aims to define the most efficient method to use in the condition monitoring of planetary gearboxes by involving different techniques.

# **Chapter 2:**

## **Numerical model description**



## Chapter 2: Numerical model description

### 1. Introduction

Numerical modelling and simulations are now a huge scientific focus that works on investigating machines behaviour and defining any component that could be related to any system's perturbation. Therefore, the ultimate purpose of this work is the electro-mechanical modelling of an electromechanical system. The system will be formed of one stage gear connected to an asynchronous motor. This chapter is presents into four main parts: First, a model of the gears is presented. This model describes the dynamic behaviour of the gears set. The second section will be dedicated to the electrical model of the driven machine which is obtained by transferring the asynchronous motor from tri-phases machine to an equivalent bi-phases machine using the Park transformation.

The third section presents a deep analytical development which describes in detail the coupling phenomenon between the electrical machine and the mechanical system. This part is dedicated essentially to define the impact of any perturbation on the motor current signal and to present the coupling terms in the numerical model. Finally, the previous two parts are gathered to present the final model based on the Multiphysics modelling of the whole testbench. This model is characterized by a system that contains non-linear equations which couple the electrical and mechanical expressions. This nonlinearity required a rung-kutta resolution method.

### 2. Gear dynamic model

The first part of the study is performed on a simple one stage of spur gears, pinion  $R_1$  and wheel  $R_2$  as defined in the figure.2.1 below. Each gear will be identified with four degrees of freedom ( $x, y, \theta_1, \theta_2$ ). Therefore, the mechanical system will be composed of eight degrees of freedom. The aim of this study is to validate the numerical model taken place before tackling a complex mechanical system.

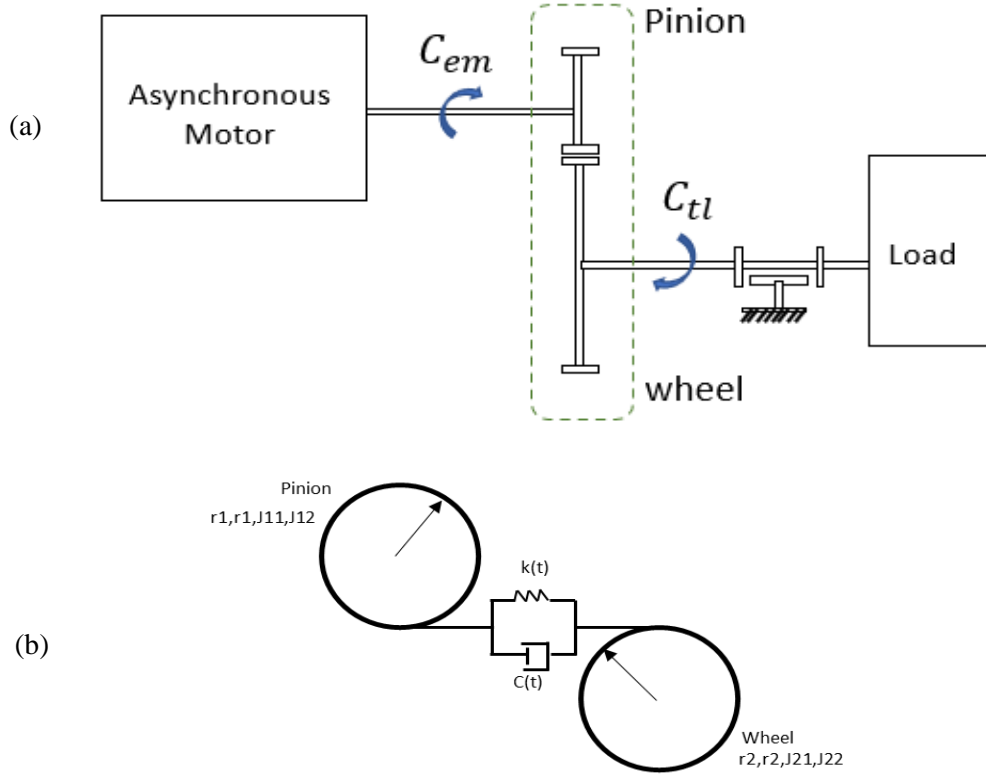


Figure.2.1: Schematic of spur gear model: (a) Global system and (b) Wheel-Pinion contact

Where:  $C_{em}$  is the motor torque and  $C_{tl}$  is the torque generated by the load.

For the meshing stiffness modelling, two approaches can be considered. Whether to consider that the teeth are infinitely rigid or to take into consideration the existence of the mesh flexibility. The first case is considered ideal and supposes that the transmission presents a permanent wheel-pinion contact. Meanwhile, this is not the case. The estimated stiffness of teeth at different points of contact on the flank and during different phases of meshing allows determining the mesh stiffness which is the main source of excitation of the system. The static torque in the system is given by an equivalent stiffness  $k_{eq}$  multiplied by the sum of the angular displacement due to the teeth, wheel, and shafts [58].

$$\frac{1}{K_{eq}} = \frac{1}{K_{bn}} + \frac{1}{K_{br}} + \frac{1}{K_w} + \frac{1}{K_t} \quad (2.1)$$

With  $K_{bn}$  is the tooth bending,  $K_{br}$  the bruising stiffness,  $K_w$  is the wheel body stiffness and  $K_t$  is the shaft twisting stiffness. Since  $K_{br}$ ,  $K_t$  and  $K_w$  is considered very high, the equivalent stiffness called gear meshing stiffness is almost equal to the bending stiffness.

The gear mesh stiffness is given by a periodic function as below:

$$k(t) = \begin{cases} K_{max} & \text{if } nT_e < t < (n+c-1)T_e \\ K_{min} & \text{if } (n+c-1)T_e < t < (n+1)T_e \end{cases} \quad (2.2)$$

where  $n$  represents the  $n^{th}$  gear meshing

The gear tooth meshes at first contact with only one pair of teeth during  $(1-c) T_e$  , then with two pair of teeth during  $(2-c) T_e$ . Using Fourier development of  $k(t)$  in (2.3) we obtain:

$$k(t) = k_m + \frac{\Delta k}{\pi} \sum_{i=1}^{\infty} \left[ \sin 2i\pi(c-1) \cos\left(\frac{2i\pi t}{T_e}\right) + 1 - \cos 2i\pi(c-1) \sin\left(\frac{2i\pi t}{T_e}\right) \right] \quad (2.3)$$

Where:

$$k_m = k_{max}(c-1) + (2-c)k_{min}$$

$$\Delta k = k_{max} - k_{min}$$

The impact of the teeth defect directly impacts the gear meshing frequency. In this case, it presents a decrease of the amplitude of the meshing stiffness periodically with angular frequency  $\omega_{def} = \frac{2\pi}{T_{def}}$  . This decrease is explained by the loss of contact while the defected tooth meshes and on the localisation of the defect. The impact of the defect is affected mainly by the number of times the defected tooth meshes.

The table.2.1 below presents the kinematic parameters of the mechanical system presented above.

Table.2.1: The kinematic parameters

Parameters	Identification
$Z_1$	Number of teeth of pinion
$Z_2$	Number of teeth of wheel
$A$	The pressure angle
$d_1$	The primitive diameter of pinion
$d_2$	The primitive diameter of wheel
$db_1$	The base diameter of pinion
$db_2$	The base diameter of wheel
$J_{12}$	The moment of inertia of the pinion
$J_{21}$	The moment of inertia of wheel
$c_{12}$	Contact ratio

Writing the kinematic and potential energies of the model yields, considering the Lagrange formal, we obtain the motion equation:

$$M\ddot{q} + C(\dot{t})\dot{q} + K(t)q = f(t) \quad (2.4)$$

With:

The mass matrix of the mechanical system is given by:

$$M = \text{diag}(M_1, M_1, J_{11}, J_{12}, M_2, M_2, J_{12}, J_{22}) \quad (2.5)$$

The damping matrix is given by:  $C = \alpha xM + \beta K_m$  :  $\alpha x = 0.05$  and  $\beta = 10^{-6}$

For the stiffness  $K(t)$  is given by:

$$K(t) = K_{cte}k(t) + K_p \quad (2.6)$$

With:

$$k_{cte} = \begin{bmatrix} (\sin(\alpha))^2 & \sin(\alpha)\cos(\alpha) & 0 & \frac{db_1}{2}\sin(\alpha) & -(\sin(\alpha))^2 & -\cos(\alpha)\sin(\alpha) & 0 & \frac{db_2}{2}\sin(\alpha) \\ \sin(\alpha)\cos(\alpha) & (\cos(\alpha))^2 & 0 & \frac{db_1}{2}\cos(\alpha) & -\cos(\alpha)\sin(\alpha) & -(\cos(\alpha))^2 & 0 & \frac{db_2}{2}\cos(\alpha) \\ 0 & 0 & 0 & 0 & 0 & 0 & 0 & 0 \\ \frac{db_1}{2}\sin(\alpha) & \frac{db_1}{2}\cos(\alpha) & 0 & \frac{db_1^2}{2} & \frac{db_1}{2}\sin(\alpha) & -\frac{db_1}{2}\cos(\alpha) & 0 & \frac{db_1}{2} * \frac{db_2}{2} \\ -(\sin(\alpha))^2 & -\cos(\alpha)\sin(\alpha) & 0 & \frac{db_1}{2}\sin(\alpha) & (\sin(\alpha))^2 & \cos(\alpha)\sin(\alpha) & 0 & -\frac{db_2}{2}\sin(\alpha) \\ -\cos(\alpha)\sin(\alpha) & -(\cos(\alpha))^2 & 0 & -\frac{db_1}{2}\cos(\alpha) & \cos(\alpha)\sin(\alpha) & (\cos(\alpha))^2 & 0 & -\frac{db_2}{2}\cos(\alpha) \\ 0 & 0 & 0 & 0 & 0 & 0 & 0 & 0 \\ \frac{db_2}{2}\sin(\alpha) & \frac{db_2}{2}\cos(\alpha) & 0 & \frac{db_1}{2} * \frac{db_2}{2} & -\frac{db_2}{2}\sin(\alpha) & \frac{db_2}{2}\cos(\alpha) & 0 & \frac{db_2^2}{2} \end{bmatrix} \quad (2.7)$$

$$K_p = \begin{bmatrix} Kx_1 & 0 & 0 & 0 & 0 & 0 & 0 & 0 \\ 0 & Ky_1 & 0 & 0 & 0 & 0 & 0 & 0 \\ 0 & 0 & K\theta_1 & -K\theta_1 & 0 & 0 & 0 & 0 \\ 0 & 0 & -K\theta_1 & K\theta_1 & 0 & 0 & 0 & 0 \\ 0 & 0 & 0 & 0 & Kx_2 & 0 & 0 & 0 \\ 0 & 0 & 0 & 0 & 0 & Ky_2 & 0 & 0 \\ 0 & 0 & 0 & 0 & 0 & 0 & K\theta_2 & -K\theta_2 \\ 0 & 0 & 0 & 0 & 0 & 0 & -K\theta_2 & K\theta_2 \end{bmatrix} \quad (2.8)$$

Where:

$$Ki_j = 10^8 \text{N/m}$$

i=x,y

j=1,2

$$K\theta_j = 10^5 \text{N/m.}$$

Finally, the external load is given as:

$$f(t) = (0 \ 0 \ C_m \ 0 \ 0 \ 0 \ -2C_m \ 0) \quad (2.9)$$

Where  $C_m = 20N.m$  is the motor torque

For this system the gear meshing frequency is given by:

$$F_{em} = F_1 Z_1 = F_2 Z_2 \quad (2.10)$$

Where  $Z_i$  is the number of teeth of the  $i^{\text{th}}$  gear and  $F_i$  is the frequency of teeth of the  $i^{\text{th}}$  gear.

### 3. Electric Drive modelling

The model used depends on the application [1]. Thus, the objective of this study is to investigate the state of the mechanical system. For this reason, it was decided to work with a DQ Park transformation since it is an analytical approach with settings easily identifiable [59]. Park transformation is an analytical method that aims to transform a three-phased machine into a bi-directional maintaining the physical phenomena.

#### 3.1. Model's assumptions

Since this method recommends theoretical developments of equations describing the electromagnetic response of an asynchronous motor, it is necessary to make the following assumptions to simplify the complexity of the system:

- The saturation is neglected: the own and mutual inductances are independent of the currents flowing in the different windings.
- Hysteresis and Eddy currents are not considered in the magnetic parts because it is assumed that the magnetic circuit is perfectly laminated.
- The notches are supposed to be infinitely thin in order to neglect the notches effect.
- Magnetomotive forces are sinusoidally distributed in the air gap and are assumed uniform; there is symmetry with respect to the magnetic axis of the windings.

The choice of the dq0 framework related to the rotating system depends on the objective of the study [60]. The change from a three-phased machine to a bi-phased was ensured by the matrix:

$$T_{dq0} = \sqrt{\frac{2}{3}} \begin{bmatrix} \cos \theta & \cos(\theta - \frac{2\pi}{3}) & \cos(\theta + \frac{2\pi}{3}) \\ -\sin(\theta) & -\sin(\theta - \frac{2\pi}{3}) & -\sin(\theta + \frac{2\pi}{3}) \\ \frac{1}{\sqrt{2}} & \frac{1}{\sqrt{2}} & \frac{1}{\sqrt{2}} \end{bmatrix} \quad (2.11)$$

Where  $\omega = \frac{d\theta}{dt}$

#### 3.2. Analytical Development

The relation ensuring the interaction between the magnetic field and the electric circuit is given by the Law of Faraday:[2]

$$v_{ij} = R_j i_{ij} + \frac{d\psi_{ij}}{dt} \quad (2.12)$$

Where:  $R_j$ : Resistance of j (stator, rotor) i: coiling (a, b, c)

$\psi_{ij}$ : The magnetic flux of j phase.

$i_{ij}$ : The current of the j phase.

The asynchronous motor case is squirrel cage motor which explains the following expression regarding electrical tension:

$$v_{ar} = v_{br} = v_{cr} = 0 \quad (2.13)$$

The relations between the magnetic flux  $\Psi$  and the current in each phase coiling, noted  $i_{ij}$ , are presented by the matrix expression below (2.14) and (2.15):

$$\begin{Bmatrix} \Psi_{as} \\ \Psi_{bs} \\ \Psi_{cs} \end{Bmatrix} = \begin{bmatrix} L_{as} & M_{as} & M_{rs} \cos \theta & M_{rs} \cos \theta & M_{rs} \cos(\theta + \frac{2\pi}{3}) & M_{rs} \cos(\theta - \frac{2\pi}{3}) \\ M_{as} & L_{as} & M_{rs} \cos \theta & M_{rs} \cos(\theta - \frac{2\pi}{3}) & M_{rs} \cos \theta & M_{rs} \cos(\theta + \frac{2\pi}{3}) \\ M_{as} & M_{as} & L_{as} & M_{rs} \cos(\theta + \frac{2\pi}{3}) & M_{rs} \cos(\theta + \frac{2\pi}{3}) & M_{rs} \cos \theta \end{bmatrix} * \begin{Bmatrix} i_{as} \\ i_{bs} \\ i_{cs} \\ i_{ar} \\ i_{br} \\ i_{cr} \end{Bmatrix} \quad (2.14)$$

$$\begin{Bmatrix} \Psi_{ar} \\ \Psi_{br} \\ \Psi_{cr} \end{Bmatrix} = \begin{bmatrix} M_{rs} \cos \theta & M_{rs} \cos(\theta - \frac{2\pi}{3}) & M_{rs} \cos(\theta + \frac{2\pi}{3}) & L_{ar} & M_{ar} & M_{ar} \\ M_{rs} \cos(\theta + \frac{2\pi}{3}) & M_{rs} \cos \theta & M_{rs} \cos(\theta - \frac{2\pi}{3}) & M_{ar} & L_{ar} & M_{ar} \\ M_{rs} \cos(\theta - \frac{2\pi}{3}) & M_{rs} \cos(\theta + \frac{2\pi}{3}) & M_{rs} \cos \theta & M_{ar} & M_{ar} & L_{ar} \end{bmatrix} * \begin{Bmatrix} i_{as} \\ i_{bs} \\ i_{cs} \\ i_{ar} \\ i_{br} \\ i_{cr} \end{Bmatrix} \quad (2.15)$$

Where:

$M_{as}$  : Mutual inductance between two phases of the stator

$M_{ar}$  : Mutual inductance between two phases of the rotor

$L_{as}$  : Self-inductance of the stator

$L_{ar}$  : Self-inductance of the stator

$M_{rs}$  : Maximum inductance between a stator's phase and a rotor's phase

The previous electrical and magnetic expressions are described in the same frame dq.

$$\begin{Bmatrix} v_{ds} \\ v_{qs} \end{Bmatrix} = \begin{bmatrix} R_s & 0 \\ 0 & R_s \end{bmatrix} \begin{Bmatrix} i_{ds} \\ i_{qs} \end{Bmatrix} + \frac{d}{dt} \begin{Bmatrix} \Psi_{ds} \\ \Psi_{qs} \end{Bmatrix} + \begin{bmatrix} 0 & -\omega_e \\ \omega_e & 0 \end{bmatrix} \begin{Bmatrix} \Psi_{ds} \\ v_{qs} \end{Bmatrix} \quad (2.16)$$

$$\begin{Bmatrix} v_{dr} \\ v_{qr} \end{Bmatrix} = \begin{bmatrix} R_r & 0 \\ 0 & R_r \end{bmatrix} \begin{Bmatrix} i_{dr} \\ i_{qr} \end{Bmatrix} + \frac{d}{dt} \begin{Bmatrix} \psi_{dr} \\ \psi_{qr} \end{Bmatrix} + \begin{bmatrix} 0 & -\omega_r \\ \omega_r & 0 \end{bmatrix} \begin{Bmatrix} \psi_{dr} \\ v_{qr} \end{Bmatrix} \quad (2.17)$$

$$\begin{Bmatrix} \psi_{ds} \\ \psi_{dr} \end{Bmatrix} = \begin{bmatrix} L_s & L_m \\ L_m & L_r \end{bmatrix} \begin{Bmatrix} i_{ds} \\ i_{dr} \end{Bmatrix} \quad (2.18)$$

$$\begin{Bmatrix} \psi_{qs} \\ \psi_{qr} \end{Bmatrix} = \begin{bmatrix} L_s & L_m \\ L_m & L_r \end{bmatrix} \begin{Bmatrix} i_{qs} \\ i_{qr} \end{Bmatrix} \quad (2.19)$$

Where:

$L_s = L_{as} - M_{as}$  : Stator synchronous inductance

$L_r = L_{ar} - M_{ar}$ : Rotor synchronous inductance

$L_m = \frac{3}{2}M_{rs}$ : Magnetizing inductance

where:  $\omega_s = p\pi f$  ,  $\omega = \frac{p\pi N}{30}$  and  $\omega_r = \omega - \omega_s$

The previous analytical development of the three phased motor had contributed to give a bi-phased equivalent machine, as presented in the figure.2.2. The stator current and the rotor magnetic flux, written in the same framework, had led to the global asynchronous machine model given by (2.15).

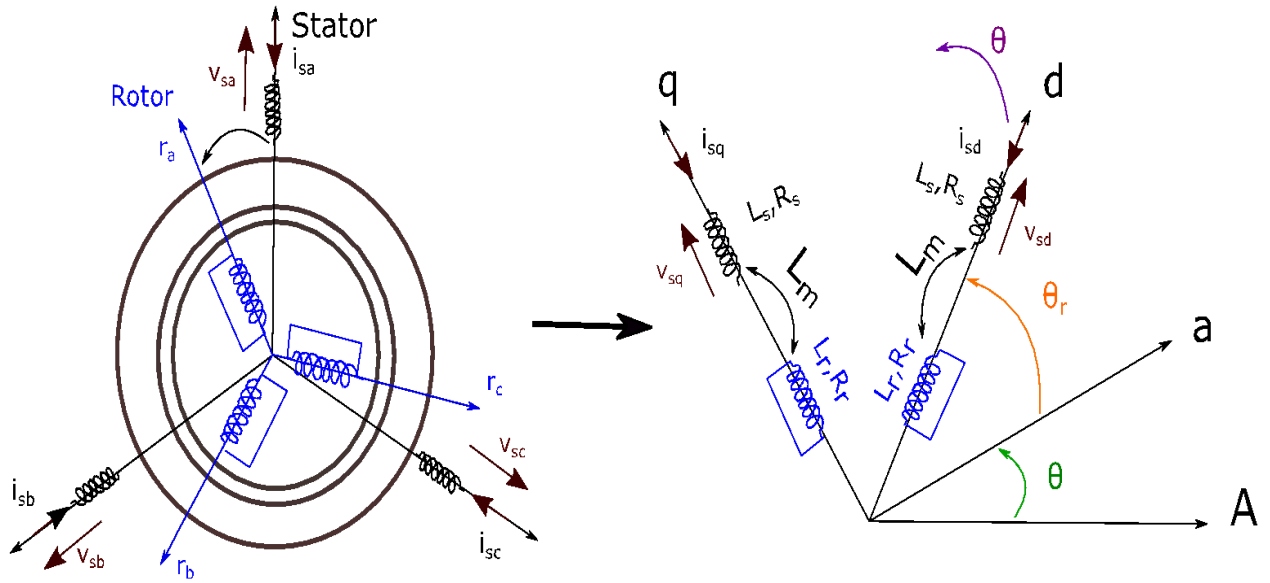


Figure.2.2: The equivalent bi-phased machine obtained from an asynchronous motor

$$\frac{d}{dt} \{X(t)\} = [A] \{X(t)\} + [B] \{U(t)\} \quad (2.20)$$

With:  $X(t)$  the state vector given by:

$$X(t) = \{i_{ds} \quad i_{qs} \quad \psi_{dr} \quad \psi_{qr}\}^T \quad (2.21)$$

$$\frac{d}{dt} \begin{Bmatrix} i_{ds} \\ i_{qs} \\ \psi_{dr} \\ \psi_{qr} \end{Bmatrix} = \begin{bmatrix} e_{11} & e_{12} * \omega_s & e_{13} & e_{14} * \omega \\ e_{21} * \omega_s & e_{22} & e_{23} * \omega & e_{24} \\ e_{31} & 0 & e_{33} & e_{34} * \omega_r \\ 0 & e_{42} & e_{43} * \omega_r & e_{44} \end{bmatrix} \begin{Bmatrix} i_{ds} \\ i_{qs} \\ \psi_{dr} \\ \psi_{qr} \end{Bmatrix} + \begin{bmatrix} \frac{1}{\sigma L_s} & 0 \\ 0 & \frac{1}{\sigma L_s} \\ 0 & 0 \\ 0 & 0 \end{bmatrix} \begin{Bmatrix} v_{ds} \\ v_{qs} \end{Bmatrix} \quad (2.22)$$

Where:

$$\sigma = 1 - \left(\frac{L_m^2}{L_s L_r}\right)$$

$$T_r = \frac{L_r}{R_r}$$

$$T_s = \frac{L_s}{R_s}$$

$$e_{11} = e_{22} = -\left(\frac{1}{\sigma T_s} + \frac{(1-\sigma)}{\sigma T_r}\right)$$

$$e_{33} = e_{44} = -\frac{1}{T_r}$$

$$e_{12} = e_{34} = 1$$

$$e_{21} = e_{43} = -1$$

$$e_{13} = e_{24} = \frac{(1-\sigma)}{\sigma T_r L_m}$$

$$e_{31} = e_{42} = \frac{L_m}{T_r}$$

$$e_{14} = -e_{23} = \frac{(1-\sigma)}{\sigma L_m}$$

#### 4. The impact of the gear's teeth crack on the gear meshing stiffness

When gears are meshed, the teeth of gears are acted upon by normal and tangential forces, leading to stress and ultimately deformation. So, if the tooth of a gear is considered as a type of cantilever beam, the deformation will be higher. Hence, the gear's materials are thermo-mechanically treated to achieve higher stiffness. The contact of two teeth from engagement to separation can be modelled by a stiffness which will obviously depend on the contact position. The mesh stiffness function is considered the most important function is gear transmission. It is classified as the principal source of vibration.

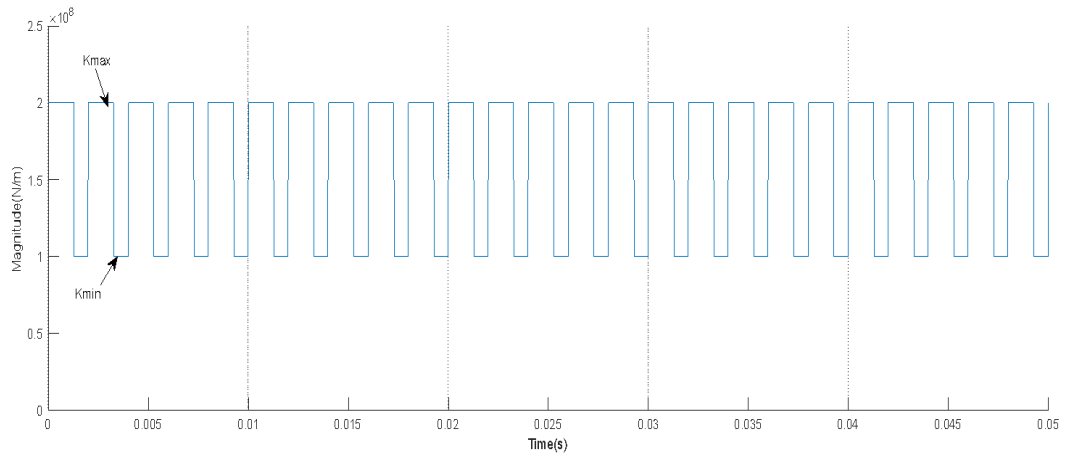


Figure.2.3: The gear meshing stiffness

The figure.2.3 presents the rate of the gear meshing stiffness. The gear mesh stiffness is periodic of a  $T_{em}$  period. A tooth crack is implemented on the pinion of the mechanical system as described in the figure.2.4. The model of the gear tooth defect is assumed as a reduction indicated by a reduction in the width of the tooth and as consequence an increase of the deflection due to the bending as studied in the work of Chaari et al. [61]. The gear tooth defect is a fall of gear mesh stiffness when the defected tooth is in contact will occur a gear meshing stiffness as seen in figure.2.4.  $T_1$  is the period of the defected tooth mesh. It corresponds to  $T_1 = \frac{1}{F_1}$  where  $F_1$  is the pinion frequency.

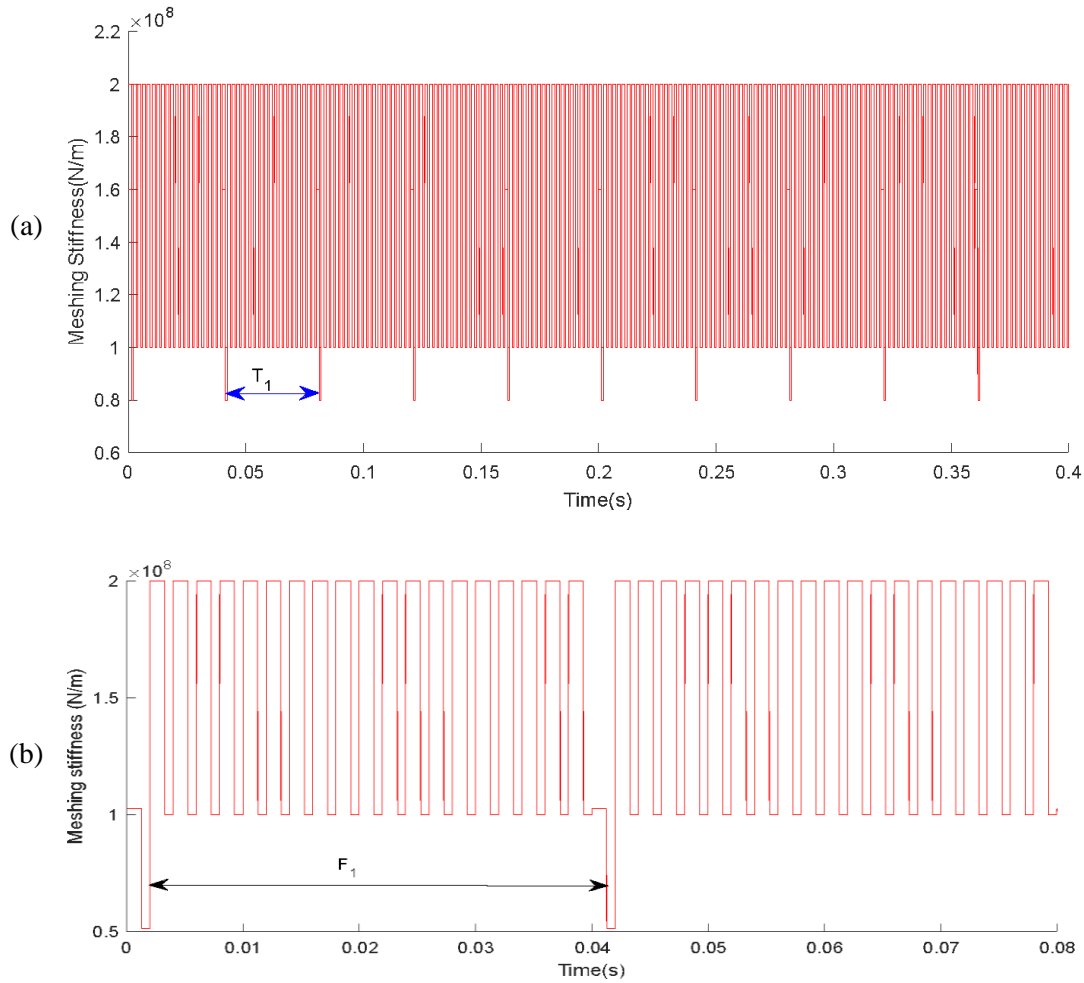


Figure.2.4: The gear meshing stiffness in the presence of tooth crack: (a): the meshing stiffness in [0s,0.4s]; (b): Zoom of the meshing stiffness in [0s,0.08s]

## 5. Electromechanical interaction

The dual mechanical system and electrical machines forms and electromechanical system. Studying these systems focuses on the interaction of electrical and mechanical systems as a whole and how the two systems interact with each other. For this study, the impact of the mechanical mechanism on the electrical system is the main interest.

### 5.1. Theoretical background

This work is interested in investigating the behaviour of the electromechanical system in the healthy configuration and in the presence of the defects. Therefore, studying the impact of the presence of gears and its defects on the motor current signal must pass by a theoretical explanation of the coupling phenomenon and all the mechanical parameters involved. The interaction between the motor and the mechanical system is caused by torque oscillation.

It has been shown that the torsional vibrations are resulted from the load oscillations in the output gears and the stiffness variation due to variation on number of teeth pairs in contact. Due to this torsional vibration, the rotation and mesh frequency components are added to the torque signal [62].

The method used to study the impact of a periodic load torque variation on the current is based on the magnetomotive force MMF and permeance wave approach [63].

The load fluctuation is mainly resulted from the mechanical contact and especially to geometry defects. In the presence of external perturbation, the load variation is given as (2.23):

$$T_{load}(t) = T_{cte} + T_{per} \cos(\omega_{per}t) \quad (2.23)$$

Where:  $T_{cte}$ : constant component,  $T_{per}$  is the amplitude of the load torque oscillation

and  $\omega_{per} = 2\pi f_{per}$ . Where  $f_{per}$  is the frequency of the external perturbation.

The motor speed can be obtained from the torque through this mathematical expression (2.24), (2.25):

$$\Sigma T(t) = T_{motor}(t) - T_{load}(t) = J \frac{d\omega_r}{dt} \quad (2.24)$$

$$\omega_r = \frac{1}{J} \int_t (T_{motor}(\tau) - T_{load}(\tau)) d\tau \quad (2.25)$$

In the steady state, the motor torque is equal to the  $T_{cte}$ : constant part of the load expression. Therefore, the rotor velocity ( $\omega_r$ ) is given by (2.26):

$$\omega_r = -\frac{1}{J} \int_t (T_c \cos(\omega_c \tau)) d\tau + C = -\frac{T_c}{J\omega_c} \sin(\omega_c t) + \omega_{r0} \quad (2.26)$$

So, the mechanical rotor position is given by the integration of the mechanical speed (2.27):

$$\theta_r(t) = \int_{t0}^t \omega_r(\tau) d\tau = -\frac{T_c}{J\omega_c^2} \cos(\omega_c t) + \omega_{r0} t \quad (2.27)$$

In ideal operating conditions  $\theta_r(t) = \omega_{r0} t$ , considering the integration constant zero. The oscillations of the mechanical rotor position  $\theta_r$  act on the rotor MMF. Otherwise, for reality, the rotor MMF in the rotor reference frame ( $R$ ), which is considered as a wave with  $p$  pole pairs and a frequency  $f_{st}$ , is given by (2.28):

$$F_{rt}^{(R)}(\theta', t) = F_{rt} \cos(p\theta' - s\omega_s t) \quad (2.28)$$

Where:  $\theta = \theta' + \theta_r$ .

$$\theta' = \theta - \omega_{r0} t - \frac{T_c}{J\omega_c^2} \cos(\omega_c t) \quad (2.29)$$

Thus, the rotor MMF can be transformed to the stationary stator reference frame using the relation

$$\omega_{r0} = \frac{1-s}{p} \omega_{st}$$

$$F_{rt}^{(R)}(\theta, t) = F_{rt} \cos \cos (p\theta - \omega_{st}t - \beta \cos \cos (\omega_{per}t)) \quad (2.30)$$

Where  $\beta = p \frac{T_{per}}{J\omega_{per}^2}$ .

As seen in equation (2.30),  $\beta \cos \cos (\omega_{per}t)$  is characterising the phase modulation in the phase of the MMF wave. The reason causing the oscillation of the torque has no direct impact on the MMF of the stator. Therefore, it can be written as following:

$$F_{st}(\theta, t) = F_{st} \cos (p\theta - \omega_s t - \varphi_s) \quad (2.31)$$

We define the air gap flux density,  $B(\theta, t)$  as the total MMF multiplied by the permeance  $\Lambda$  (which is considered as a constant for the sake of simplicity).

$$B(\theta, t) = (F_{st}(\theta, t) + F_{rt}(\theta, t))\Lambda = B_s \cos (p\theta - \omega_{st}t - \varphi_s) + B_r \cos (p\theta - \omega_{st}t - \beta \cos (\omega_{per}t)) \quad (2.32)$$

The phase modulation of the flux density  $B(\theta, t)$  exists for the flux  $\Phi(t)$ .  $\Phi(t)$  is obtained by a simple integration of  $B(\theta, t)$  (2.32) with respect to the winding structure. The winding structure has only an influence on the amplitudes of the flux harmonic components, not on their frequencies. Therefore,  $\Phi(t)$  is an arbitrary phase that can be expressed in a general form:

$$\phi(t) = \phi_s \cos (\omega_s t + \varphi_s) + \phi_r \cos (\omega_s t + \beta \cos (\omega_c t)) \quad (2.33)$$

The relationship between the current and the magnetic flux is given by Faraday law (2.34) as:

$$V(t) = R_s I(t) + \frac{d\phi(t)}{dt} \quad (2.34)$$

with  $V(t)$  is the voltage introduced from the source.

The derivation of the flux from (2.33) yields to:

$$\frac{d\phi(t)}{dt} = -\omega_{st}\phi_s \sin (\omega_s t + \varphi_s) - \omega_{st}\phi_r \sin (\omega_s t + \beta \cos (\omega_{per}t)) + \omega_{per}\beta\phi_r \sin (\omega_s t + \beta \cos (\omega_{per}t)) \sin (\omega_s t) \quad (2.35)$$

Finally, the stator current in any selected phase will be given by the expression below:

$$I(t) = \frac{1}{R_{st}} (V(t) - \frac{d\phi(t)}{dt}) \quad (2.36)$$

$$I(t) = \frac{1}{R_s} (V(t) - [-\omega_s \phi_s \sin(\omega_{st}t + \varphi_s) + \sin(\omega_{st}t + \beta \cos(\omega_{per}t))] [-\omega_s \phi_r + \omega_{per} \beta \phi_r \sin(\omega_s t)]) \quad (2.37)$$

In the work presented by Feng *et al.* [64], the gear fault generates a load torque oscillation that produces both FM (Frequency Modulation) and AM (Amplitude Modulation) effecting the stator current (2.37), with the supply frequency as a carrier frequency. The FM and AM frequencies are equal to the key frequencies of the gearboxes (meshing frequency, rotating frequency, and default frequency in case of defected gears). The current is expressed finally as following (2.38):

$$I(t) = i_{st}(t) + i_{rt}(t) = I_{st} \sin(\omega_{st}t + \varphi_s) + I_{rt} \sin(\omega_{st}t + \beta \cos(\omega_{per}t)) \quad (2.38)$$

With:  $i_{st}(t)$  is the result from the stator MMF and  $i_{rt}(t)$ , a direct consequence of the rotor MMF.  $i_{st}(t)$  is not influenced by the torque oscillation, although  $i_{rt}(t)$  is the term that shows the phase modulation due to the torque fluctuation. Feng *et al.* have used this demonstration that explains the impact of the torque fluctuation on the stator current to describe the electro-mechanical interaction between the motors and the mechanical systems.

### 5.3. Coupling model

The objective beyond this study is to have a multiphysics model of the testbench, which will help later in detecting any anomaly in the mechanical system using the current signal [65]. Therefore, the figure .2.5 presents the electromechanical interaction between both mechanical and the electrical model. To do so, the coupled state variable vector (3.18) contains the different electrical parameters of the motor (current and magnetic flux) and the displacement of each node of gear component and its velocity.

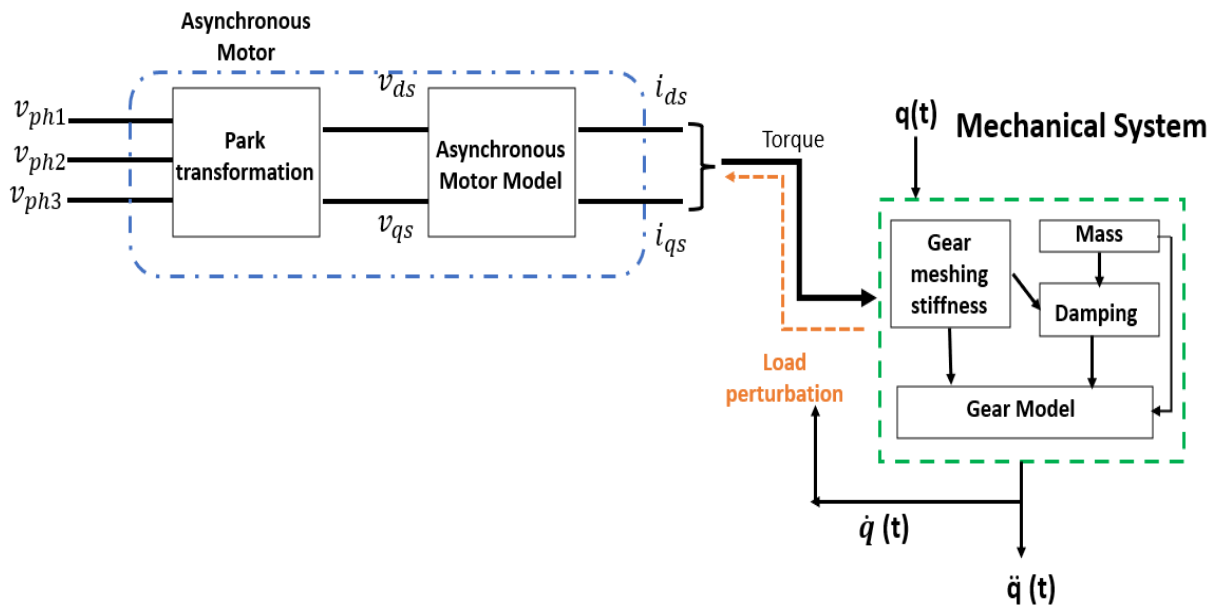


Figure.2.5: Scheme of the coupling model of the electromechanical system

This state vector is deduced from the need of combining a first order differential system (electrical equation) and the motion equation.

$$\{Z(t)\} = \{X(t) Y(t) \dot{Y}(t)\}^T \quad (2.39)$$

The coupled system gives a first order differential system, expressed in (2.40).

$$\dot{Z}(t) = A(t, Z(t)) Z(t) + B(t) \quad (2.40)$$

Where A(t) and B(t) are developed in the expression below.

$$\frac{d}{dt} \begin{pmatrix} i_{ds} \\ i_{qs} \\ \psi_{dr} \\ \psi_{dr} \\ u_1 \\ \dots \\ u_{12} \\ \dot{u}_1 \\ \dots \\ \dot{u}_{12} \end{pmatrix} = \begin{bmatrix} e_{11} & e_{12}\omega_s & e_{13} & e_{14}(\omega + \dot{u}_1) & 0 & \dots & \dots & 0 & 0 & \dots & \dots & 0 \\ e_{21}\omega_s & e_{22} & e_{23}(\omega + \dot{u}_1) & e_{24} & 0 & \dots & \dots & 0 & 0 & \dots & \dots & 0 \\ e_{31} & 0 & e_{31} & e_{34}\omega_r & 0 & \dots & \dots & 0 & 0 & \dots & \dots & 0 \\ 0 & e_{42} & e_{43}\omega_r & e_{44} & 0 & \dots & \dots & 0 & 0 & \dots & \dots & 0 \\ 0 & 0 & 0 & 0 & 0 & \dots & \dots & 0 & 1 & \dots & \dots & 0 \\ \dots & 0 & \dots & 1 & \dots & \dots \\ \dots & 0 & \dots & \dots & \dots & 0 \\ 0 & 0 & 0 & 0 & 0 & \dots & \dots & 0 & 0 & \dots & \dots & 1 \end{bmatrix} \begin{pmatrix} i_{ds} \\ i_{qs} \\ \psi_{dr} \\ \psi_{dr} \\ u_1 \\ \dots \\ u_{12} \\ \dot{u}_1 \\ \dots \\ \dot{u}_{12} \end{pmatrix} + \begin{bmatrix} 0 & 0 \\ \dots & \dots \\ \dots & \dots \\ 0 & 0 \end{bmatrix} \left[ p \frac{L_m}{L_r} \text{inv}(M) * F \begin{bmatrix} -\text{inv}(M) K \\ -\text{inv}(M) C \end{bmatrix} \right] \begin{pmatrix} i_{ds} \\ i_{qs} \\ \psi_{dr} \\ \psi_{dr} \\ u_1 \\ \dots \\ u_{12} \\ \dot{u}_1 \\ \dots \\ \dot{u}_{12} \end{pmatrix} + \begin{pmatrix} \frac{v_{ds}}{\sigma L_s} \\ \frac{v_{qs}}{\sigma L_s} \\ 0 \\ \dots \\ 0 \\ \dots \\ \dots \\ \dots \\ \text{inv}(M) F_{imp} \end{pmatrix} \quad (2.41)$$

The electro-mechanical interaction between the motor and the gearboxes system is ensured through:

- The impact of the system's vibrations and any anomaly is presented in equation (2.40) by  $\dot{\theta}_{sun}$ .
- The mechanical torque transmitted to the gearbox given by the following expression:

$$C_{em} = \frac{pL_m}{L_r} (\psi_{dr} i_{qs} - \psi_{qr} i_{ds}) \quad (2.42)$$

{F} express the coupling terms between the electrical and the mechanical model. This vector contains the current which would be multiplied by the magnetic flux, to express the electromagnetic torque (2.42).

Where: { $F_{imp}$ } expresses the external efforts if it exists.

### 5.3. Solution

The model includes non-linear terms which define the coupling between the electrical and the mechanical systems. For the resolution we used Runge Kutta order 4 (ode4). This algorithm based on a fixed increment is widely used for its accuracy and reduced time of simulation.

## 6. Case study: Simple stage of spur gears

The objective beyond exposing the results obtained for a simple spur gears model simulation is to validate the electrical model before coupling it to the complex model of the back-to-back gearboxes torsional model. The current result obtained from the numerical simulation is the projection on d axis  $i_{ds}$ .

### 6.1.The electromechanical system

The spur gears are formed of a pinion noted  $R_1$  ( $Z_1=20$ ) and wheel  $R_2$  ( $Z_2=30$ ). The key frequencies related to the mechanical system are presented in the table.2.2.

Table.2.2: The key frequencies of the mechanical system

Parameters	Value	Identification
$F_1$	20Hz	Frequency of pinion
$F_2$	16.67Hz	Frequency of wheel
$F_m$	500 Hz	The meshing frequency

For the driven machine, an asynchronous motor is considered. The supply frequency is maintained at 50Hz, with external load Given 300N.m. The electrical parameters of the motor are given in the table.2.3.

Table.2.3: Motor parameters

Parameters	Value
$R_s$	8.3 $\Omega$
$R_r$	4.162 $\Omega$
$L_s$	0.1215H
$L_r$	0.0983H
$L_m$	0.0983H

### 6.2.Time motor current signal $I_{ds}$ for coupled system for healthy configuration

Figure.2.6 illustrates the time evolution of the stator current  $i_{ds}$  obtained from the Park Transformation. As seen, the current signal is divided into two parts. The steady state regime, which is the concern of this study, and the transient regime that represents the run up of the motor. For this approach only results seen in the steady state are representative and will be investigated in this chapter. In Figure.4.1, the current signal shows a periodic fluctuation with an amplitude  $5.10^{-3}$  A and a period that corresponds to the gear mesh period  $T_{em} = 0.002s$  given by:

$$T_{em} = \frac{1}{F_m} \quad (2.43)$$

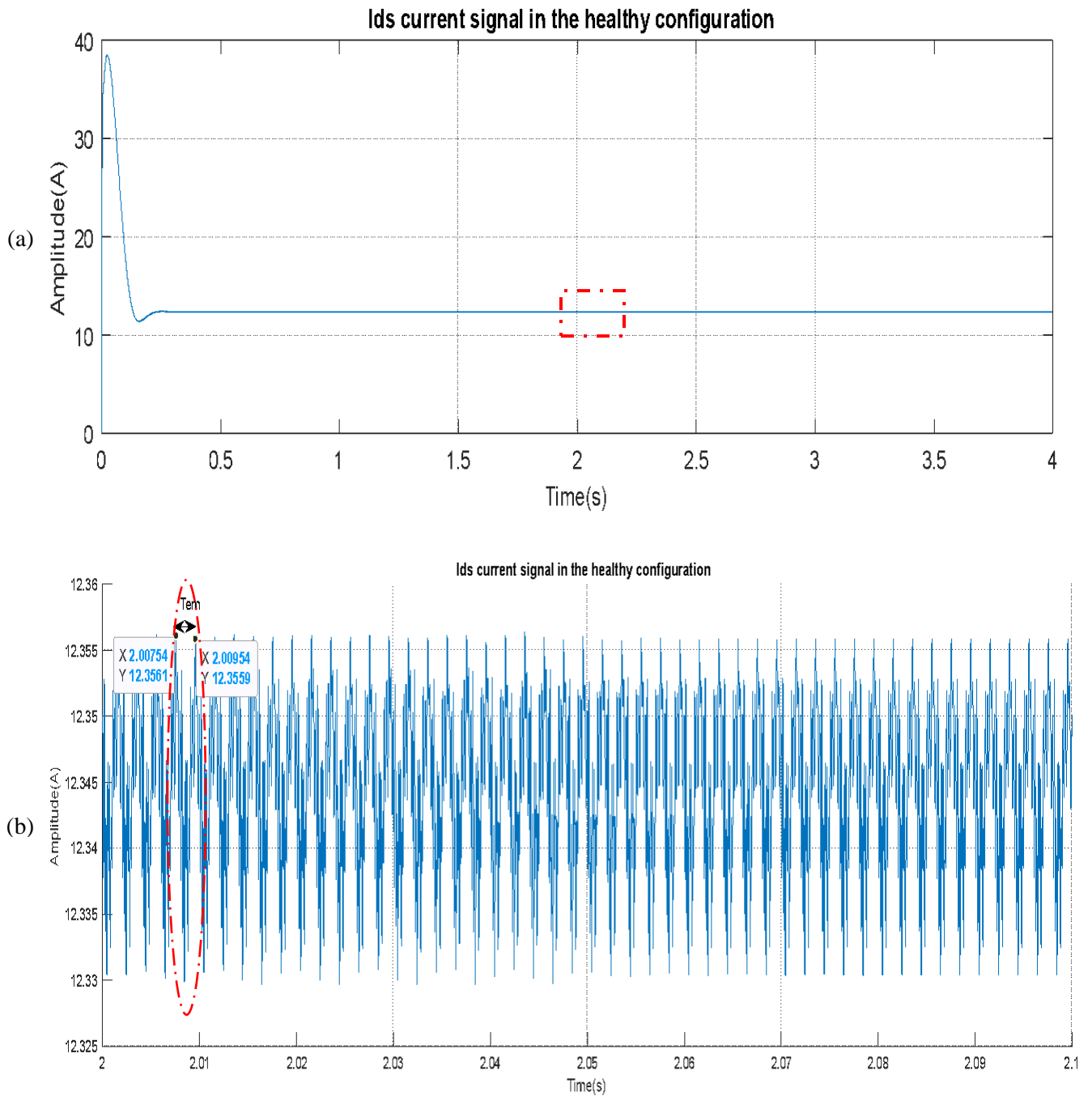


Figure.2.6: Stator current signal  $i_{dS}$  on the dq frame

(a): The current stator signal in [0s;4s]; (b): zoom of the current stator signal in [2s;2,1s]

### 6.3. The Mechanical signals in presence of tooth crack

The figure.2.7 presents the pinion velocity in two different configurations: The signal illustrated in blue represents the velocity in the healthy configuration, Meanwhile the red signal shows the pinion velocity in the presence of tooth crack. During each period of rotation of pinion besides to the meshing period additional peaks are noticed in time responses: these peaks are related to the faulty gear.

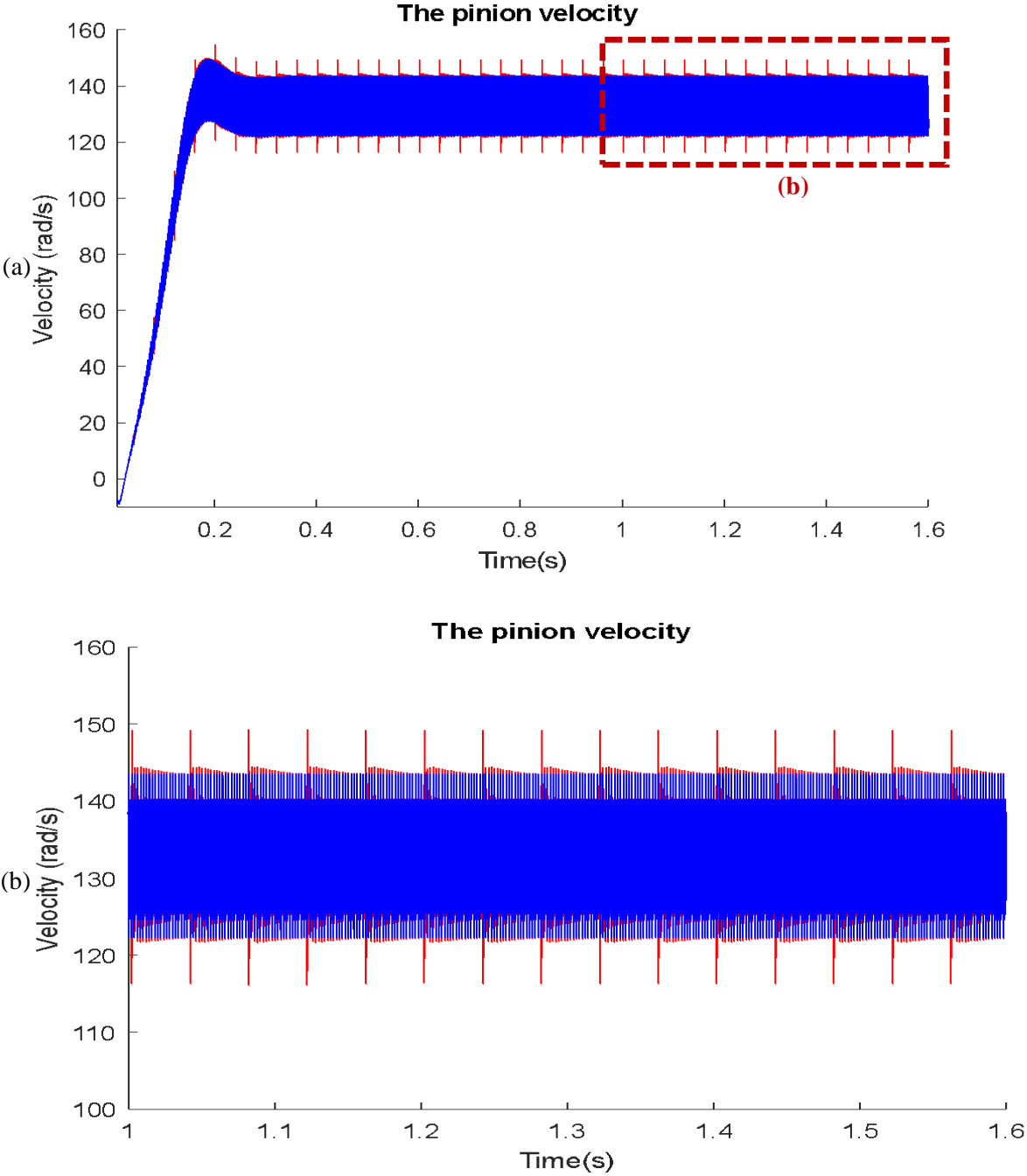


Figure.2.7: The velocity of the pinion in two operating configurations.

(a): The velocity of the pinion in [0s;1,6s]; (b): zoom of the pinion velocity in[1s;1,6s]

### 6.4.The impact of signal defect on current signal

The aim of this part of work is to investigate the sensitivity of the modelled current signal  $i_{ds}$  to the defect, its location, and its gravity impact on the current signal. Therefore, crack will be implemented on the gear teeth.

#### 6.4.1. Single defect impact on the stator current

The figure.2.8 presents a comparative investigation between the  $i_{ds}$  current signal for healthy configuration and in the presence of wheel tooth defect. As clearly seen in the figure.2.8, in the red current signal we notice presence of periodic impulses with periodicity  $t_f = Z_1 * T_{em}$ , which represent the wheel characteristic period ( $Z_1$  is the number of teeth of the damaged gear). In fact, the local change produced by the tooth damage in the mesh stiffness excites a periodic impulse in the tensional vibration, which is transmitted itself to the stator current,

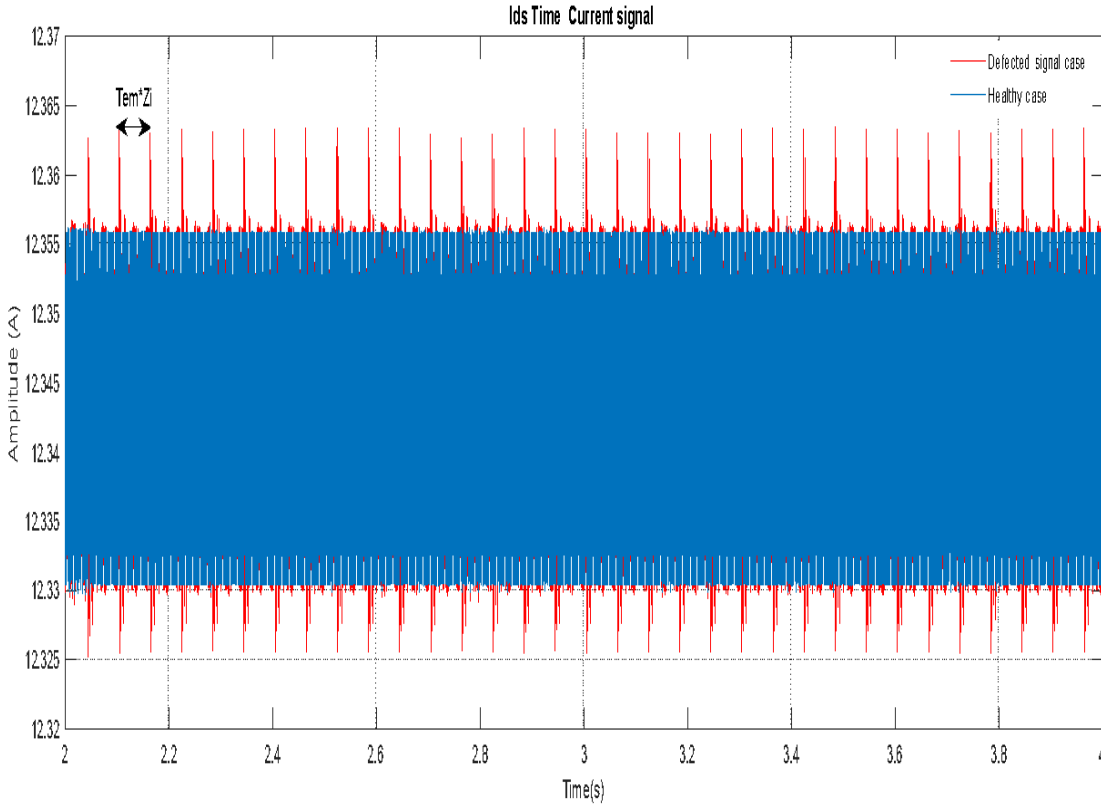


Figure.2.8. Stator current signal  $i_{ds}$  on the dq frame

The temporal variation highlights the impact of the electromechanical coupling on the current  $i_{ds}$  signal. To better identify the components impacting the signal, the coming results will be presented in a frequency domain using Fast Fourier Transformation (FFT) applied on the time  $i_{ds}$  signal. This will highlight the sensitivity of the current  $i_{ds}$  to the mechanical coupling and the perturbation due to the gear defect.

The figure.2.9 presents the  $i_{ds}$  frequency spectrum. Besides to the gear meshing frequency, sidebands has appeared as seen in the zoom. These sidebands present the related pinion frequency which identify the defect presence and location.

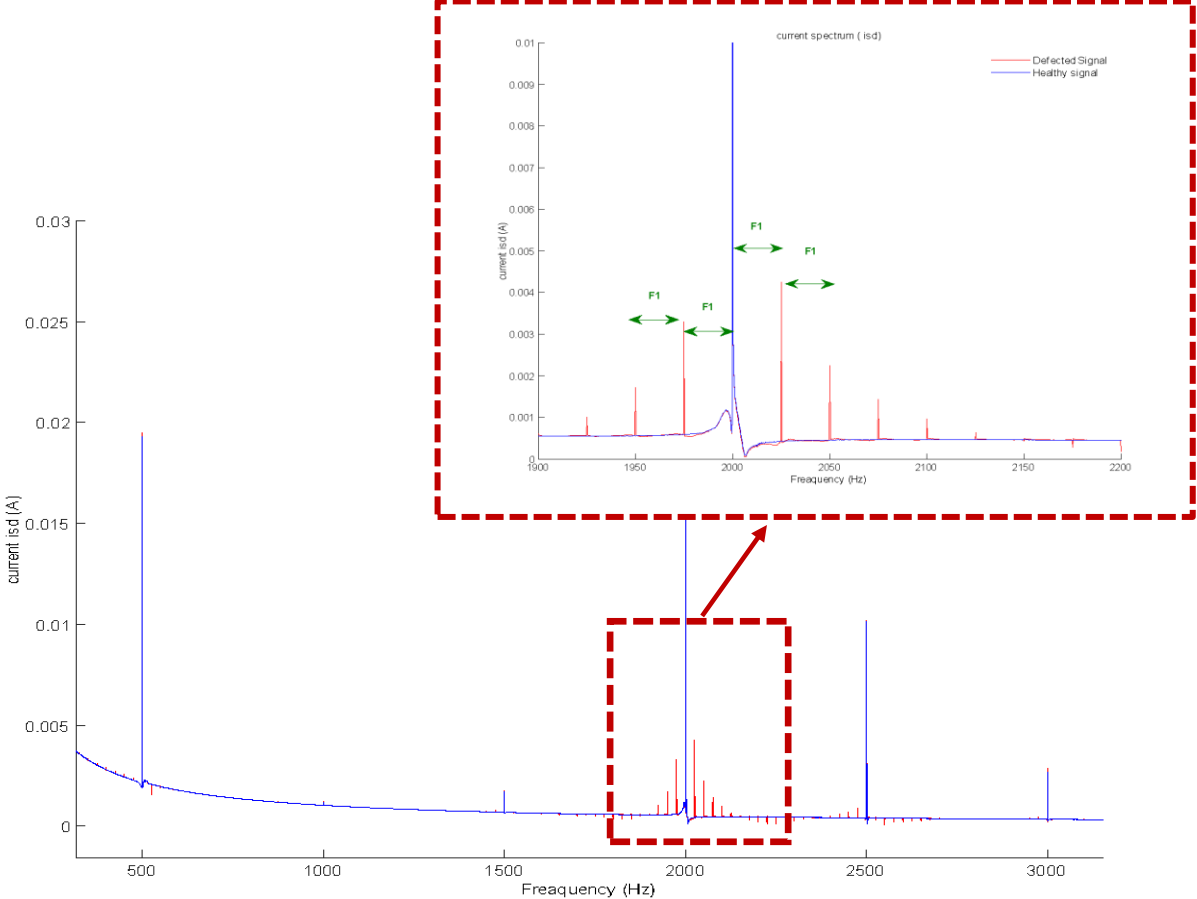


Figure.2.9. Frequency spectrum of the Stator current signal  $i_{ds}$  on the dq frame in healthy configuration and defected case

**6.3.3. The impact of the defect severity on the stator current**

In order to investigate the gravity of the crack, different groove size has been exposed to simulations. Figure.2.10 shows the influence of increasing the defect gravity (10 to 50%) on the current frequency spectrum. The focus in the figure.2.10 is establish on the sidebands around  $4F_m$ .

For a defect on the wheel, the amplitude of the peak related to the defect frequency proportionally increases with the defect. These faults express a transmission error and cause failure in the operation of the gears. The dysfunction resulting from tooth defect results in loss of contact due to deviation from the ideal profile which generates a decrease in the periodic decrease in the meshing stiffness [66]. The more the defect’s size is, the more the meshing stiffness decreases. The important impact in the stiffness

generates an important an  
confirmed by the study ela

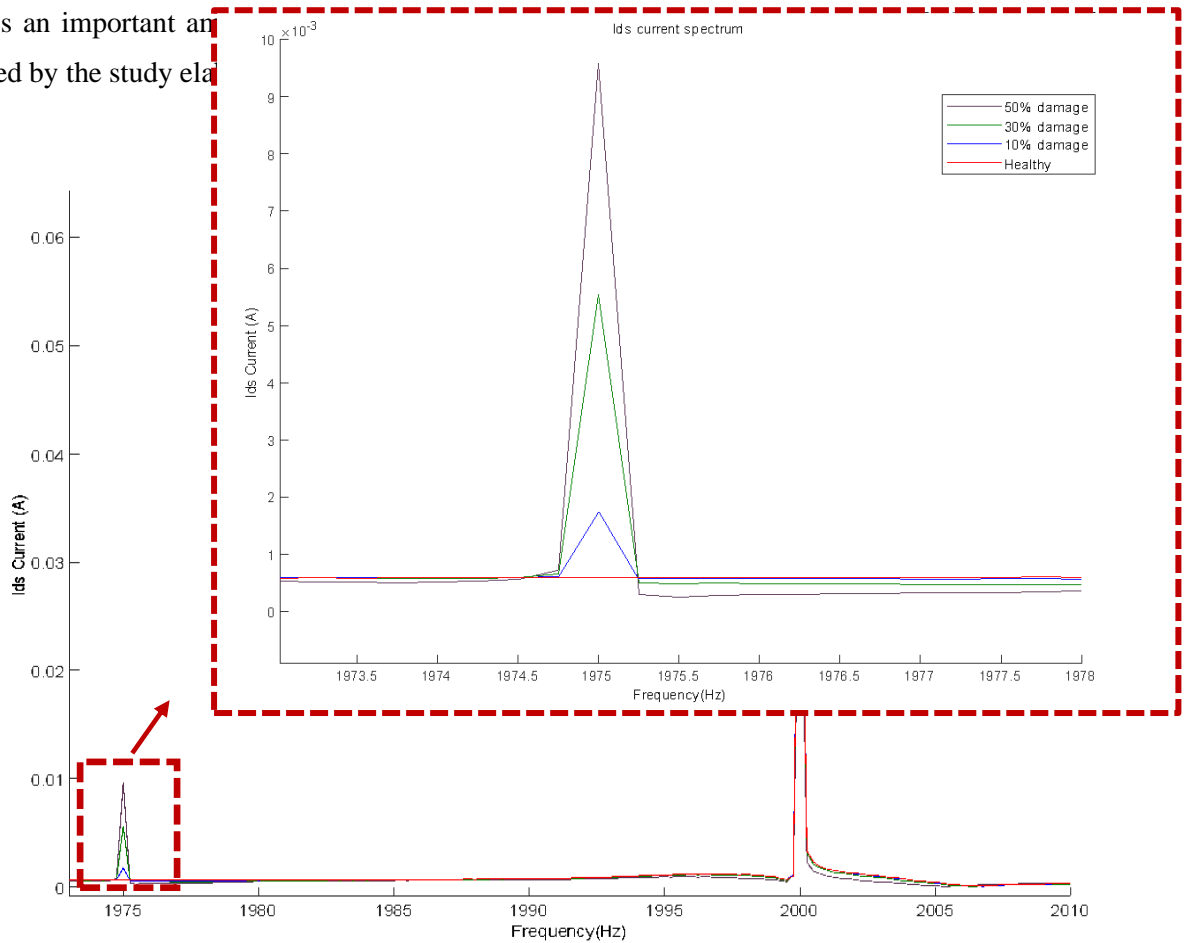


Figure.2.10. Frequency spectrum of the Stator current signal  $i_{ds}$  on the dq frame for defect's dimension

### 6.3.3. The impact of combined defects of the stator current

In this case study, two defects were included. One defect on the pinon tooth and another over the wheel tooth. Figure.2.11 presents the current spectrum of  $i_{ds}$ . Besides to the gear meshing frequency and its harmonics  $nF_{em}$ , additional lateral sidebands related to  $F_1$  and  $F_2$  appears. Moreover, another component, defining the coincidence of the meshing of both defects is observed. This frequency denoted by  $F_{co}$  is given by:

$$F_{co} = \frac{F_{em}}{LCM(Z_1, Z_2)} = 8.33\text{Hz} \quad (2.44)$$

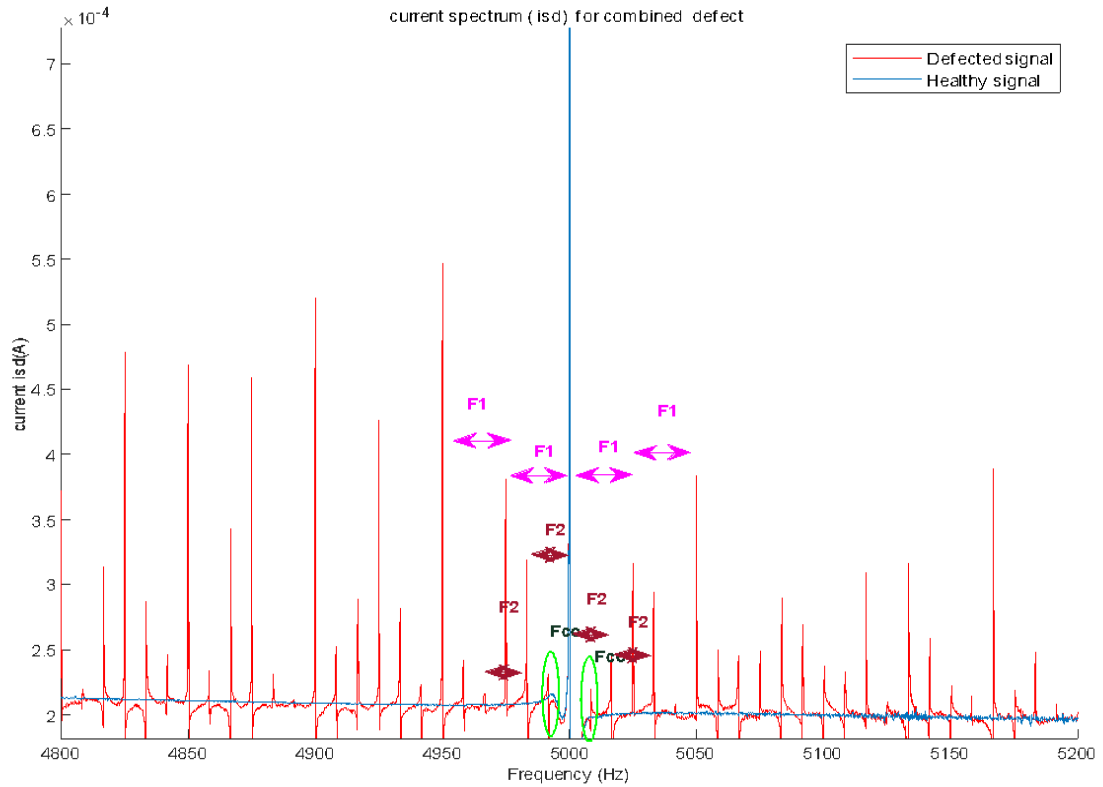


Figure.2.11. Frequency spectrum of the Stator current signal  $i_{ds}$  on the dq frame in healthy configuration and defected case (for combined defects)

## 7. Conclusion

The appearance of the tooth defect in a mechanical system impacts the gear meshing stiffness. This impact is generated as a load perturbation transmitted the electrical drive. The appearance of the key frequency of the defect in the current spectrum is related to the size and the severity of the impact and the location on the defect. The study has proved in simulations the sensitivity of the stator current to the mechanical defects by using Park transformation model and a dynamic model of simple stage of gears. The use of this example has aimed to validate the electro-mechanical model developed in the defect's detection.



# **Chapter 3:**

## **Experimental test benches**



## Chapter 3: Experimental test benches

### 1. Introduction

Gears are used in power transmission in different industrial domains depending of the uses. Planetary gears are considered used for power transmission due to their high efficiency and their significant transmitting power with large speed reductions or multiplications. Therefore, several research studies are devoted to these gears. Different developed models tried to investigate the condition monitoring of the gear transmissions as described in the first chapter. In order to have more credibility related to these models a detailed experimental validation is demanded. Test benches can be suitable tools to achieve experimental investigation on planetary gear. In this chapter, a back-to-back planetary gear test bench is used to validate the numerical model. Experiments will be mainly related to the stator current signature analysis technique.

So, in order to get used with the experimental tests and the instrumentation, tooling and tests were first elaborated on a simple low speed test bench. Then in a second place, the mechanical part of the planetary test bench is described. After all, instrumentation layout is presented and the developed alternatives for measurement are detailed.

### 2. Low-speed test bench

The study will be accomplished at a first place on an experimental test bench as illustrated in the figure.3.1. This test bench is composed of two parts: The mechanical system is defined in a pair of helical gears: ( $Z_1 = 60$  , and  $Z_2 = 30$  ) and a geared motor: a Bauer geared motor (Type: BG50-11D099A4-Tk-K311). The load is introduced by a compressed air brake connecting the output shafts.

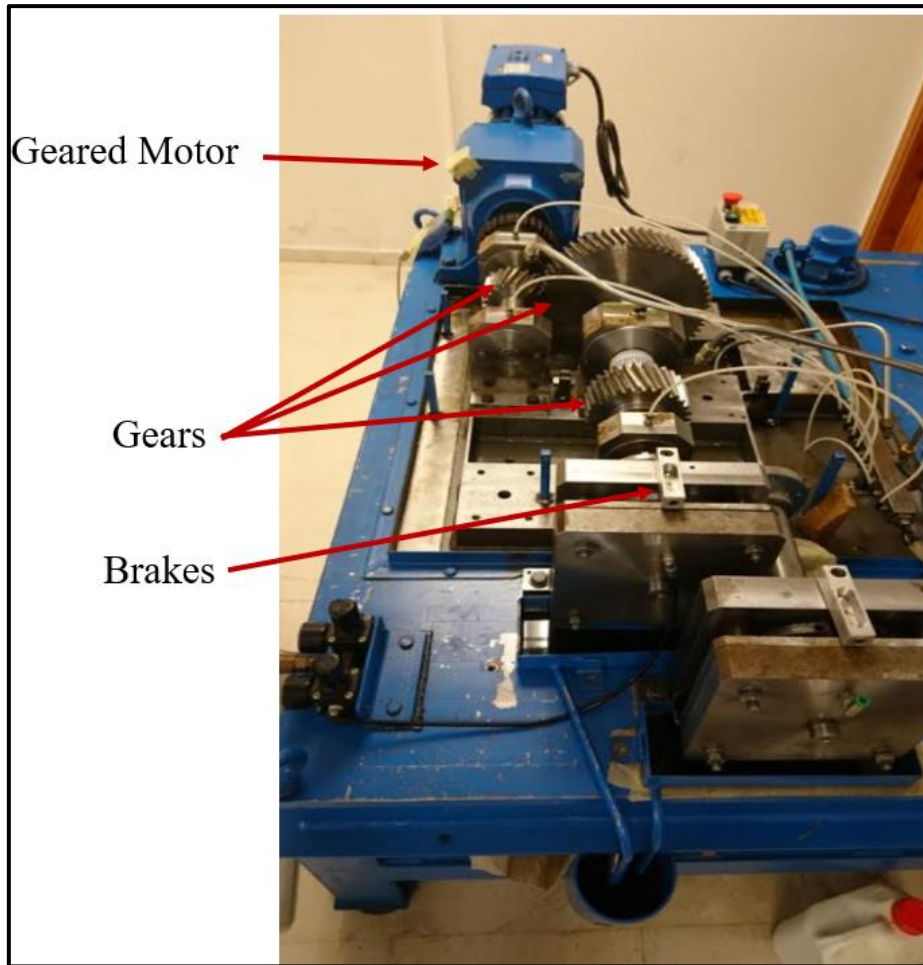


Figure.3.1.: The experimental test rig

The driving system is composed of a three-phase asynchronous motor (4 poles, 1,1Kw,  $f_e=50\text{Hz}$ , 1400rpm) and a double-stages gearbox. Both stages are formed of helical gears.

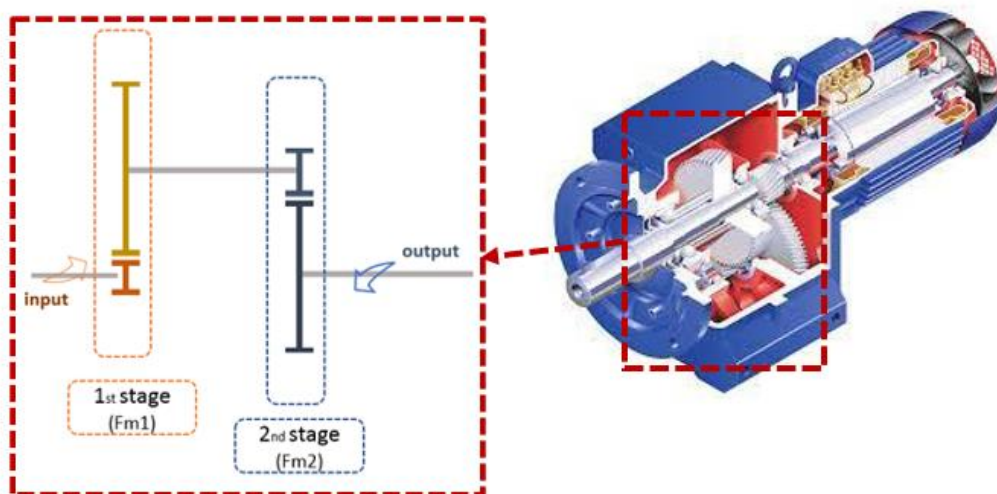


Figure.3.2: The geared motor structure [1]

Table.3.1 shows the mechanical parameters of the geared motor.

Table.3.1. The mechanical characteristics of the geared motor

	Teeth number		Reduction Ratio
	First stage	Second stage	
The Motor	$Z_{11}=10$	$Z_{21}=62$	47.02
	$Z_{12}=91$	$Z_{22}=12$	

The study on the low-speed test bench will take place for a motor frequency given 30 Hz, 840 rpm input to the geared system and 30rpm output to the mechanical system. For the mechanical system, the mechanism is illustrated in the figure.3.3.

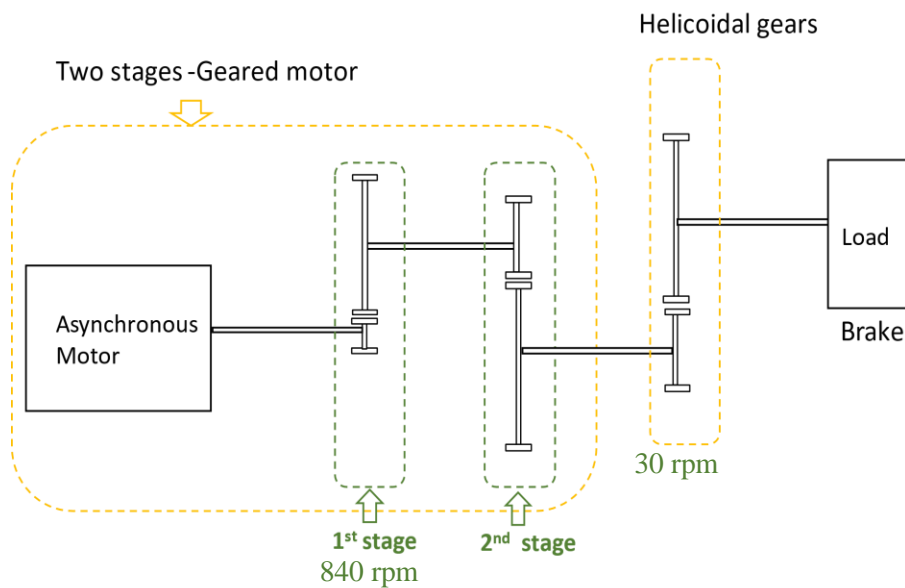


Figure.3.3: The low-speed test bench system

For the mechanical system described in the figure.3.3 the characteristics are presented below in table3.2.

Table 3.2. The Mechanical system Characteristics

Teeth number	Reduction Ratio
$Z_1=60$	2
$Z_2=30$	

### 3. Planetary gearbox testbench

The experimental investigation work is basically done on the planetary gearboxes, shown in figure.3.4. The test bench of double stage planetary gearboxes was developed in the university of Cantabria at the department of Structural and Mechanical engineering.

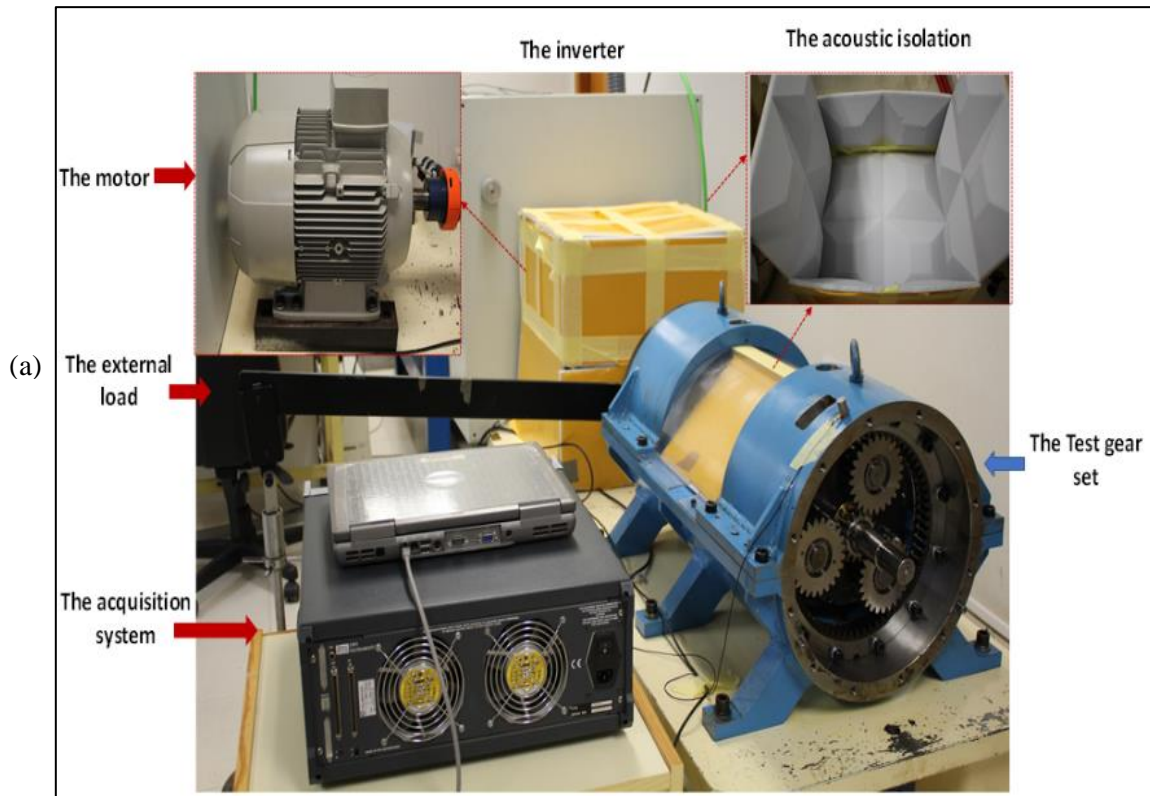
The test bench is composed of two parts. The driving part is a three-phase asynchronous motor. The mechanical part is structured as a back-to-back planetary gearbox which is basically composed of two identical stages of a planetary gearbox: a reaction gearbox (r) and test gearbox (t). Each gearbox is composed of three types of gears (table.3.3): A ring (R), a sun and a carrier (C) holding three planets (P).

Table.3.3: The mechanical system parameters

Gearbox		Component			
		Carrier	Planet	Ring	Sun
	<b>Count</b>	1	3	1	1
	<b>Teeth number</b>	--	24	65	16
	<b>Mass (kg)</b>	3.65	1.22	28.1	0.49

Each stage, as shown in figure.3.4 (b), is composed of an external ring, three planets fixed on a carrier and a sun which is the input gear. The back-to-back configuration offers a mechanical power circulation for energy efficiency. Both gearboxes are connected to each other through a rigid hollow shaft that holds both carriers and a second one that connects the sun of the reaction gearbox to the test sun [68]. The test gearbox is totally fixed, while the reaction gearbox is maintained free and connected to an external arm to introduce the load.

This arm allows an external load on the reaction ring. Depending on the rotation direction the load is applied by adding masses or using a jack. The layout of the testbench and the state of the gears allows a maximum torque 1100N.m [69] to avoid teeth bending. In all the operating conditions along the test, we count working in a range from 100N.m to 900N.m.



(b)



Figure.3.4: the experimental test bench (a) The experimental set (b) Load application

The mechanical system is driven by an asynchronous three phase SEIMENS motor, seen in the figure.3.4. The motor was controlled by a frequency inverter “MICROMASTER 440” located in the electrical cabinet connected to it as seen in the figure.3. 5. Different motor’s parameters are presented in the table.3.4.

Table.3.4: The parameters of the motor

<b>Motor</b>							
<b>Connection</b>	<b>Hz</b>	<b>Kw</b>	<b>Cos</b>	<b>Speed (rpm)</b>	<b>V</b>	<b>A</b>	<b>Poles</b>
<b>400 Triangle connected</b>	50	15	0.82	1460	380-420	30-30.2	4
<b>690 Y connected</b>	50	15	0.82	1460	660-725	17.4-17.5	4
<b>Inverter</b>							
	<b>V</b>		<b>A</b>		<b>Hz</b>		
<b>Input</b>	380-480		37		74-63		
<b>Output</b>	0-input		32		0-65Hz		

The inverter is used to control the speed frequency of the motor, magnitude, and direction. The inverter will be controlled by a SIEMENS Software STRATER. This software ensures the adjusting of the motor speed required and also provides the hand to track some of the motor's parameters.



Figure.3.5: The electrical cabinet

#### 4. Instrumentations

The aim of this research work is to establish a multidomain investigation of the dynamic behaviour of the planetary gears. Therefore, this study involves different physical parameters to be measured. The focus will be split between both electrical and mechanical signals. For the electrical part, the motor phase current is recorded in the first place.

This signal will be simultaneously tracked with the accelerations of the test gearbox and the acoustic pressure around the mechanical system. Hence, the figure.3.6 illustrates the disposition of each sensor

on the test bench. Tests were taken at different operating speeds and loads. This experimental rig layout seen below allows to easily obtain a multidomain study on the planetary gearbox.

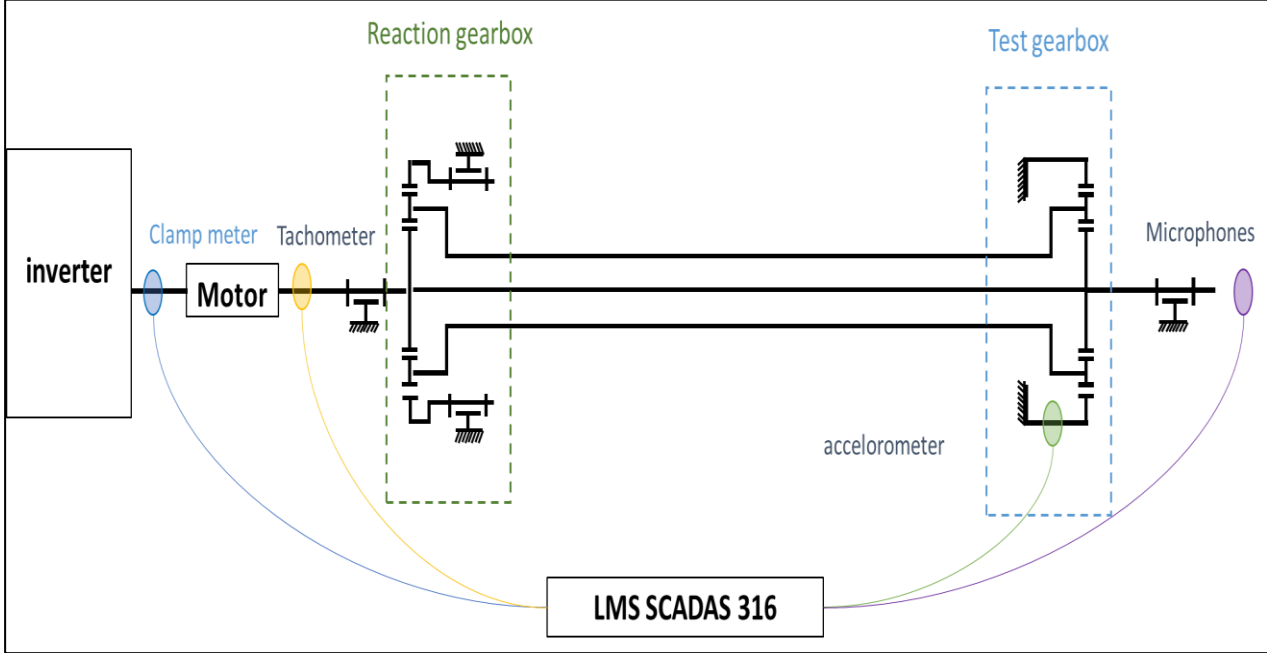


Figure.3.6: Placement of different sensors on the test bench

**4.1. Sensors**

Starting with the current measurements, clamp meters of type fluke **i200s ac with 10mA/V** sensitivity, were mounted on the input of the motor to measure the phase current as clarified in the figure.3.7(a). The bandwidth of the sensor is limited to [40Hz;10kHz] adapting the needs of the companies interested in this equipment. So, the accuracy specification revolves around the requirements for those distribution measurements. The interest of such sensors is mainly measuring the current signal along time in a motor phase. In fact, the alternating current through the wire creates a magnetic field which the meter uses to measure the current. The more current, the stronger the field.

On the other hand, to record the vibration signal of the system, a tri axial accelerometer with 127.02mV/g sensitivity was used. The accelerometer was disposed of as seen in the figure.3.7(b). Before mounting it on the ring of the test gearbox, this accelerometer was first calibrated using A “Brüel & Kjør” calibration exciter. Simultaneously, an optic tachometer type Compact VLS7 with pulse tapes was placed on the shaft connecting the motor to the gearbox to measure the angular velocity. The resolution is the frequency resolution of the data block. It is related to the frequency range and the number of lines in the block (Resolution = Bandwidth / Frequency lines). After that, we ranged the signals in the same onplet.

Finally, for the acoustic measurements, a sound intensity probe set seen in the figure.3.7(c) was installed. This probe is composed of Dual Preamplifier Type 2682, Sound Intensity Microphone Pair Types 4197

and 4178 and solid plastic spacer and an analyser. Besides a robust frame which holds the preamplifiers and matches microphones in the face-to-face configuration [70]. Two microphones, 0.16mV/Pa sensitivity each, were placed near the test gearbox in order to minimise the environment noise. Sound Intensity Calibrator Type 4297 was used for the sound-pressure calibration and pressure-residual intensity-index verification of both microphones.

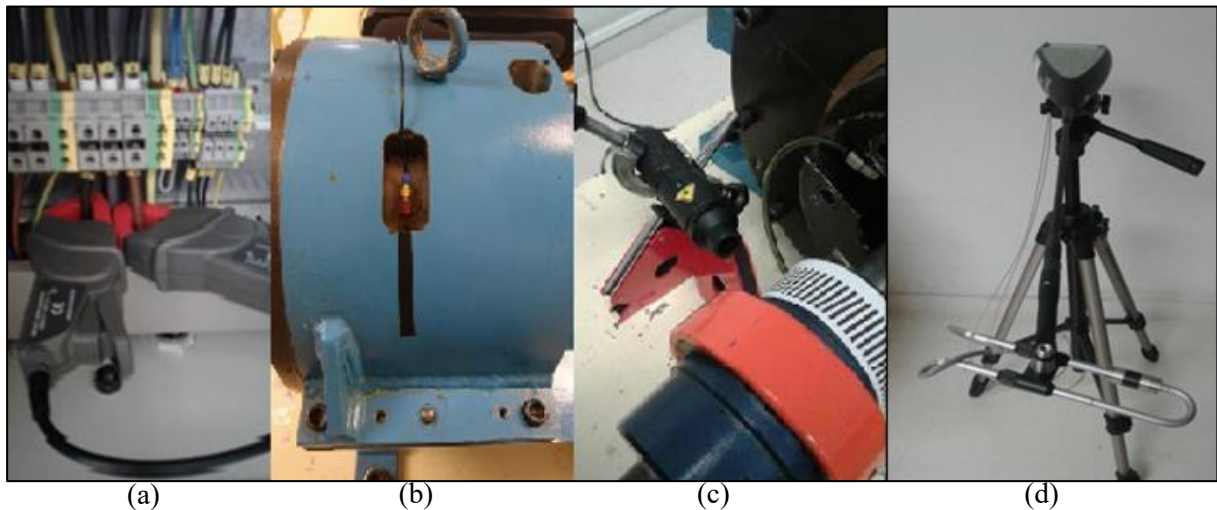


Figure.3.7: Sensors used in the test: (a) Clamps, (b) Accelerometer, (c) Tachometer and (d) Microphones

#### 4.2.Acquisition

For the data collection, all the sensors were connected to an LMS SCADAS316, as seen in the figure.3.6, monitored by LMS TestLab software. Measurements were taken in different operating conditions, varying load and speed each time. These different measurements are recorded simultaneously using a SCADAS Data Acquisition shown in the figure.3.8, which is controlled by the LMS testLab 15A module, LMS Test.Lab signature acquisition. Stator currents, angular displacement and vibrations signals and acoustic pressure were recorded at a rate of 64000 Hz and for each experiment a minimum of 300s was recorded. Once all the sensors are connected to the SCADAS, the LMS Test lab, all the parameters related to each sensor are included as seen in the figure.3.8(a) . For each physical channel, it is necessary to include the direction, measured quantity, appropriate units and the actual sensitivity after calibration.

For the planetary gearbox, experiments are taken in three stages: First, we will start investigating the motor state by taking current for the free motor in order to highlight the frequency related to the electrical device components. Second, the electromechanical impact on the motor current signal is investigated simultaneously with the vibrations level by tracking current, vibrations, and acoustic pressure for a healthy component set. Later defected components will be implemented to investigate the signals responses to these changes.

✓ Direction                      ✓ Parameter                      ✓ Calibration

(a)

PhysicalChannelId	OnOff	ChannelGroupId	Point	Direction	InputMode	Measured Quantity	Electrical Unit	Actual Sensitivity	
Tacho1	<input type="checkbox"/>	Tacho	Tacho1	None	Voltage DC				
Tacho2	<input checked="" type="checkbox"/>	Tacho	Tacho2	None	Voltage DC				
Input1	<input checked="" type="checkbox"/>	Other	voltageT	None	Voltage DC	Voltage	mV	100	mV/V
Input2	<input checked="" type="checkbox"/>	Other	current pHU	None	Voltage DC	Current	mV	10	mV/A
Input3	<input checked="" type="checkbox"/>	Vibration	accX	+X	ICP	Acceleration	mV	13.50797	mV/g
Input4	<input checked="" type="checkbox"/>	Vibration	accY	+Y	ICP	Acceleration	mV	13.94968	mV/g
Input5	<input checked="" type="checkbox"/>	Vibration	accW	+Z	ICP	Acceleration	mV	14.05896	mV/g
Input6	<input type="checkbox"/>	Vibration	Point6	None	Voltage AC	Acceleration	mV	100	mV/g
Input7	<input type="checkbox"/>	Vibration	Point7	None	Voltage AC	Acceleration	mV	100	mV/g
Input8	<input checked="" type="checkbox"/>	Other	current pHW	None	Voltage DC	Current	mV	10	mV/A
Input9	<input type="checkbox"/>	Vibration	Point9	None	Full bridge DC	Strain	mV	0.001	mV/ $\mu$ E
Input10	<input type="checkbox"/>	Vibration	Point10	None	Full bridge DC	Strain	mV	0.001	mV/ $\mu$ E
Input11	<input type="checkbox"/>	Vibration	Point11	None	Full bridge DC	Strain	mV	0.001	mV/ $\mu$ E
Input12	<input type="checkbox"/>	Vibration	Point12	None	Full bridge DC	Strain	mV	0.001	mV/ $\mu$ E

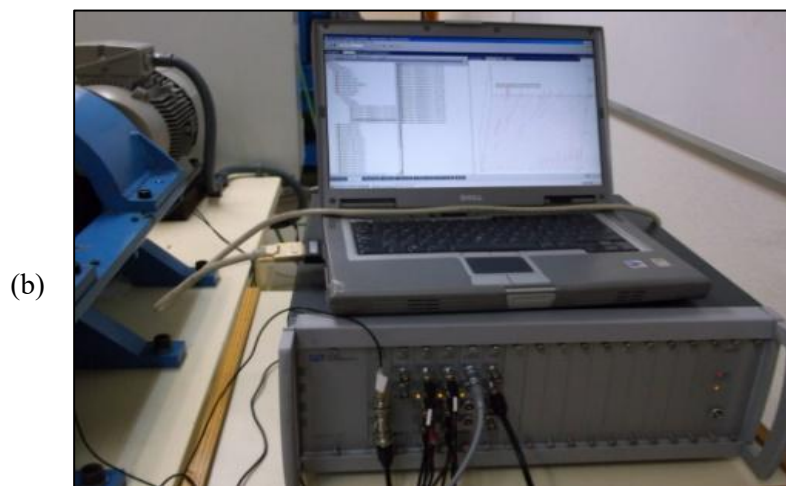


Figure.3.8: SCADAS Data acquisition: (a) input scheduling; (b) the SCADAS system managed by LMS Test Lab

## 5. Conclusion

This chapter presents the equipment used for the experimental investigations. The main test bench is a double-stages planetary test rig with a mechanical power recirculation. In order to build a multidisciplinary study, three sensors were implemented: an accelerometer to record the vibrations' signals, two microphones used to save the acoustic pressure issued by the sound around the test bench. And finally electrical clamp, defined to save the phase motor current. The study of the electromechanical correlation between the mechanical system and the motor was studied at first place on a low-speed test bench with spur gears.

Three gears configurations were defined: a gear set reference, which presents the healthy case. A degradation gear set: through this gearbox we will study the impact of the degradation phenomenon on the current motor signal. And finally, the defected gears set it forms the gearboxes with mechanical

defects formed on gears. These experimental measurements will validate the numerical model simulations of the planetary gearboxes test bench. This model will be developed in the next chapter.

**Chapter 4:**  
**Dynamic behaviour of a double stage  
planetary gearbox by the motor  
current signal**



# **Chapter 4: Dynamic behaviour of the double stage planetary gearbox by the motor current signal**

## **1. Introduction**

The numerical modelling of gears has been used in studying the dynamic behaviour and monitoring these systems. The multiphysics model described in chapter 2 will be extended to describe the planetary test bench seen in chapter.3. This chapter will be divided into two main parts. The first part describes the numerical model of the double stage planetary gearbox connected to an asynchronous motor (seen in the chapter.3). The second part presents the results of the simulations. In this chapter, MCSA is presented for a healthy set of gears.

## **2. Assumptions**

The driving machine used in the testbench is an asynchronous machine seen in chapter.3. The Park transformations developed in chapter.2 will be used to model the induction machine. The first step for a general modelling and characterising of the behaviour of any mechanism is identifying all its physical parameters. These parameters will be necessary involved in modelling and interpreting results.

### **2.1. Define parameters**

The investigations taken place in this work is based essentially on the impact due to the mechanical system on the driving machine. Therefore, it requires all the physical parameters of the motor. In order to obtain the specific electrical parameters, the datasheet of the motor present of the MICROMASTER database was used. The stator and rotor resistance are directly obtained from the software, and for the inductance we used the equivalent circuit seen in the figure.4.1. [69]

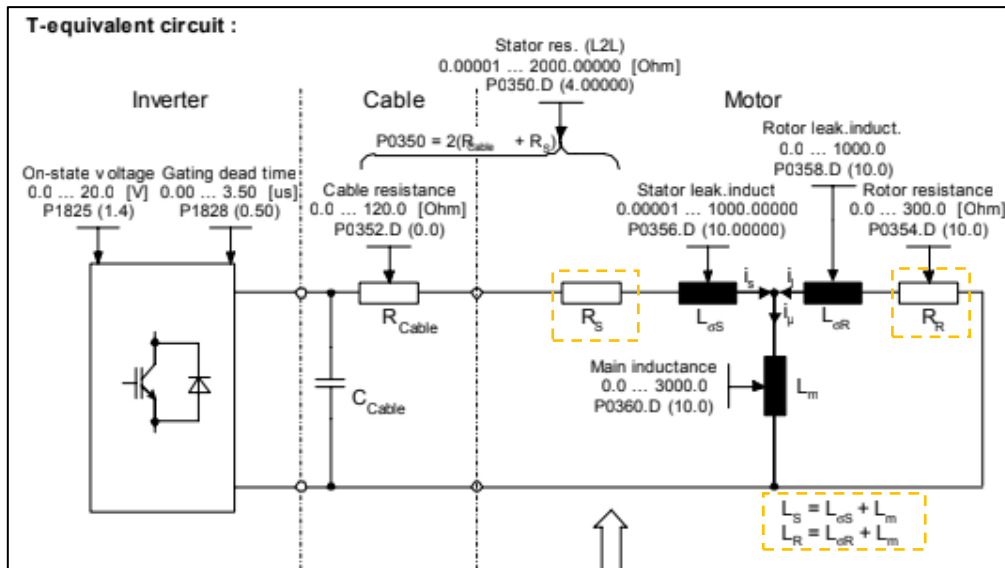


Figure.4.1. The T-equivalent circuit of asynchronous motor

The motor's parameters extracted from the MICROMASTER as defined in the table.4.1 seen below. These parameters will be used in the numerical model.

Table.4.1. The motor's parameters

Parameter	Value
$R_s$	9.172 $\Omega$
$R_r$	5.162 $\Omega$
$L_s$	0.115 H
$L_r$	0.0943 H
$L_m$	0.0943 H

For the mechanical part, an analytical model based on the real test rig is developed (figure.4.1). It is a mono-dimensional numerical model of the studied two planetary gearbox sets which are reaction planetary gearbox (r) and test planetary gearbox (t). A ring (r), a carrier (c), a sun (s) and three planets ( $p_1, p_2, p_3$ ) are the principal elements of each gear set.

As seen in the figure.4.2(c) the carrier held an equally spaced planet. For the reaction gearbox it is considered that the planet's phases ( $0, 3 2\pi, 3 4\pi$ ) count the test gear set ( $3 \pi, \pi, 3 5\pi$ ). This geometry details are considered in the numerical model. For the connection between both stages, the connecting shafts will be modelled by torsional stiffness.

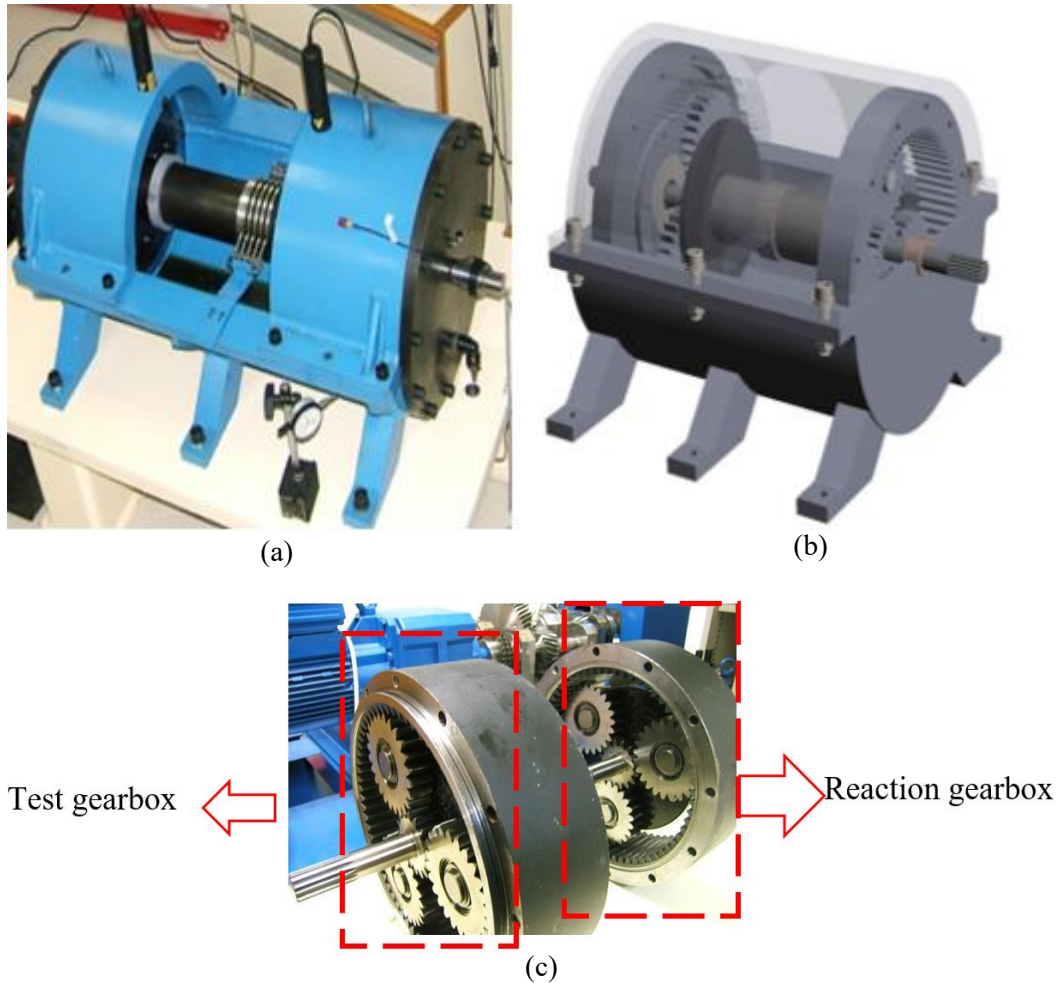


Figure.4.2.: The double stage gearbox system (a): experimental test rig; (b): numerical model of the system and (c) disposal of the planets on the carrier

## 2.2.Key frequencies

For planetary gears, the transmission ratio depends on the fixed gear. In our case, we define  $R_{sc}$  the transmission ratio, where the ring is held fixed ( $\omega_r = 0$ ), the sun is considered the system's input and the carrier is the output [70].

$$R_{sc} = \frac{N_s}{N_c} = \frac{Z_s + Z_r}{Z_s} \quad (4.1)$$

In the same context, we define the gear ratio of the sun and the planet which is given by:

$$R_{sp} = \frac{N_s}{N_p} = \frac{Z_p}{Z_s} \quad (4.2)$$

Where;  $N_i$  represents the speed velocity (rpm) of the  $i^{th}$  gear.

Each gear in the system is seen in the spectrum by its key frequency. It identifies the impact of the oscillations due to its displacement. The table.4.2 presents the characteristic frequencies for the test

bench. For an initial situation, the motor's frequency is given 50Hz with a rotational speed equal to 1490rpm.

Table.4.2: key frequencies in planetary gearbox

Frequencies	Expression	Value (Hz)
Frequency motor $F_{motor}$	---	50
Sun frequency $F_{sun}$	$F_{sun} = \frac{N}{60}$	24.9
Carrier frequency $F_{carrier}$	$F_{carrier} = \frac{F_s}{R_{sc}}$	4.93
Planet passing $F_{pp}$	$F_{pp} = 3F_{carrier}$	14.79
Planet frequency $F_{planet}$	$F_{planet} = R_{sp}F_{sun}$	37.35
Sun frequency with respect to the carrier $F_{sc}$	$F_{sc} = F_{sun} - F_{carrier}$	19.97
planet frequency with respect to the carrier $F_{pc}$	$F_{pc} = \frac{F_{sc}}{R_{sp}}$	13.31
Mesh frequency $F_{mesh}$	$F_{mesh} = Z_r F_{carrier}$	320.07

### 3. Numerical model of the planetary testbench

The model of the back-to-back planetary gear used in the coming part is based on that developed by Lin and Parker [71]. In the work of Ahmed et al. [70], a model has been presented of a torsional model of double stage gearbox. The model was used to study the dynamic behaviour of the mechanical system.

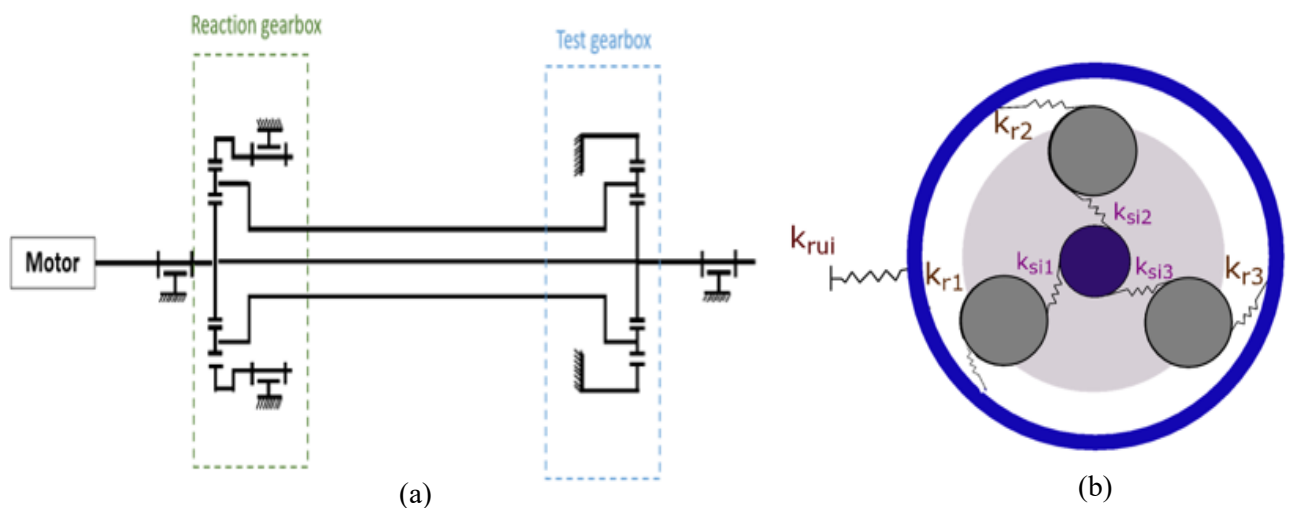


Figure.4.5: Numerical model of the test bench: (a) kinematic and (b) dynamic model

The first model used is a torsional model which defines each component by one unique torsional degree of freedom.

The system's equation of motion for back-to-back planetary gear with 3 planets is given by:

$$M\ddot{q} + C\dot{q} + (K(t) + K_c)q = F(t) \quad (4.3)$$

M represents the mass matrix.

$$M = \text{diag}\left(\frac{I_{cr}}{r_{cr}} + Nm_{pr}, \frac{I_{rr}}{r_{rr}}, \frac{I_{sr}}{r_{sr}}, \frac{I_{1r}}{r_{1r}}, \frac{I_{2r}}{r_{2r}}, \frac{I_{3r}}{r_{3r}}, \frac{I_{ct}}{r_{ct}} + Nm_{pt}, \frac{I_{rt}}{r_{rt}}, \frac{I_{st}}{r_{st}}, \frac{I_{1r}}{r_{1r}}, \frac{I_{2r}}{r_{2r}}, \frac{I_{3r}}{r_{3r}}\right) \quad (4.4)$$

Where  $I_{ij}$  refers to inertia of each component and  $r_{ij}$  is the base radius of i, j component. And C refers to the damping matrix. C is taken as a Rayleigh damping. The mesh stiffness of the system is given by the matrix both  $K(t) = \text{diag}(K_s, K_r)$  and  $K_c$  the coupling matrix between each gearbox.

Where  $K_r$  and  $K_s$  refers respectively to the ring mesh stiffness matrix and sun mesh stiffness which are expressed as:

$$K_r(t) = \begin{bmatrix} \sum_{i=1}^3 (K_{sri}(t) + K_{rri}(t)) & -\sum_{i=1}^3 K_{rri}(t) & -\sum_{i=1}^3 K_{rri}(t) & K_{rr1}(t) - K_{sr1}(t) & K_{rr2}(t) - K_{sr2}(t) & K_{rr3}(t) - K_{sr3}(t) \\ -\sum_{i=1}^3 K_{rri}(t) & \sum_{i=1}^3 K_{rri}(t) & 0 & -K_{rr1}(t) & -K_{rr2}(t) & -K_{rr3}(t) \\ -\sum_{i=1}^3 K_{sri}(t) & 0 & \sum_{i=1}^3 K_{sri}(t) & K_{sr1}(t) & K_{sr2}(t) & K_{sr3}(t) \\ K_{rr1}(t) - K_{sr1}(t) & -K_{sr3}(t) & K_{sr1}(t) & K_{sr1}(t) + K_{rr1}(t) & 0 & 0 \\ K_{rr2}(t) - K_{sr2}(t) & -K_{rr2}(t) & K_{sr2}(t) & 0 & K_{sr2}(t) + K_{rr2}(t) & 0 \\ K_{rr3}(t) - K_{sr3}(t) & -K_{rr3}(t) & K_{sr3}(t) & 0 & 0 & K_{sr3}(t) + K_{rr3}(t) \end{bmatrix} \quad (4.5)$$

$$K_t(t) = \begin{bmatrix} \sum_{i=1}^3 (K_{sti}(t) + K_{rti}(t)) & -\sum_{i=1}^3 K_{rti}(t) & -\sum_{i=1}^3 K_{rti}(t) & K_{rt1}(t) - K_{st1}(t) & K_{rt2}(t) - K_{st2}(t) & K_{rt3}(t) - K_{st3}(t) \\ -\sum_{i=1}^3 K_{rti}(t) & \sum_{i=1}^3 K_{rji}(t) & 0 & -K_{rt1}(t) & -K_{rt2}(t) & -K_{rt3}(t) \\ -\sum_{i=1}^3 K_{sti}(t) & 0 & \sum_{i=1}^3 K_{sti}(t) & K_{st1}(t) & K_{st2}(t) & K_{st3}(t) \\ K_{rt1}(t) - K_{st1}(t) & -K_{st3}(t) & K_{st1}(t) & K_{sj1}(t) + K_{rj1}(t) & 0 & 0 \\ K_{rt2}(t) - K_{st2}(t) & -K_{rt2}(t) & K_{st2}(t) & 0 & K_{st2}(t) + K_{rt2}(t) & 0 \\ K_{rt3}(t) - K_{st3}(t) & -K_{rt3}(t) & K_{st3}(t) & 0 & 0 & K_{st3}(t) + K_{rt3}(t) \end{bmatrix} \quad (4.6)$$

And

$$K_c = \begin{bmatrix} k_c & 0 & 0 & 0 & 0 & 0 & -k_c & 0 & 0 & 0 & 0 & 0 \\ 0 & k_{rtu} & 0 & 0 & 0 & 0 & 0 & 0 & 0 & 0 & 0 & 0 \\ 0 & 0 & k_s & 0 & 0 & 0 & 0 & 0 & -k_s & 0 & 0 & 0 \\ 0 & 0 & 0 & 0 & 0 & 0 & 0 & 0 & 0 & 0 & 0 & 0 \\ 0 & 0 & 0 & 0 & 0 & 0 & 0 & 0 & 0 & 0 & 0 & 0 \\ -k_c & 0 & 0 & 0 & 0 & 0 & k_c & 0 & 0 & 0 & 0 & 0 \\ 0 & 0 & 0 & 0 & 0 & 0 & 0 & k_{rtu} & 0 & 0 & 0 & 0 \\ 0 & 0 & 0 & 0 & 0 & 0 & 0 & 0 & k_s & 0 & 0 & 0 \\ 0 & 0 & -k_s & 0 & 0 & 0 & 0 & 0 & 0 & 0 & 0 & 0 \\ 0 & 0 & 0 & 0 & 0 & 0 & 0 & 0 & 0 & 0 & 0 & 0 \\ 0 & 0 & 0 & 0 & 0 & 0 & 0 & 0 & 0 & 0 & 0 & 0 \end{bmatrix} \quad (4.7)$$

Q(t) is the degree of freedom vector expressed by:

$$q(t) = \{u_{cr} \ u_{rr} \ u_{sr} \ u_{1r} \ u_{2r} \ u_{3r} \ u_{ct} \ u_{rt} \ u_{st} \ u_{1t} \ u_{2t} \ u_{3t}\}^T \quad (4.8)$$

The figure.4.2, illustrates a numerical schema of the test bench and clarifies the connection between both gearboxes and all the corresponding parameters are presented in detail in Tab.3. The connecting shafts are modelled by torsional stiffness given by  $k_s$  and  $k_c$ . Where  $k_s$  is given to the stiffness of the shaft connecting the suns and  $k_c$  for the hollow shaft connecting carriers. Seen that, the reaction ring is free, its torsional stiffness  $K_{rru}$  equals to zero, although, the test ring is not completely clamped so a high torsional stiffness  $K_{rtu}$  is given.

We consider the rotational coordinates are given by;  $u_{ij} = r_{ij}\theta_{ij}$ .

Where  $i=r, c, s, 1, 2, 3$ . Also  $r$  is the base radius and  $\theta$  are the rotational components.

The torsional model described of the double stage planetary gearbox is connected to the electrical modelled as developed already in (2.41). The resolution of the equation of motion is achieved using the step-by-step implicit Runge Kutta ode4.

## **4. The impact of the mechanical behaviour on the current signal**

The electromechanical model presents the impact of the mechanical system on the simulated current. The current  $i_{ds}$  is presented in both the temporal and frequency domain. After all, an inverse of Park Transformation is used on the simulated current  $i_{ds}$  to obtain the motor phase current.

### **4.1. Temporal domain response**

The direct-quadrature-zero transformation is a mathematical transformation used to simplify the analysis of a three phased motor. This method uses the three phases current presented in a sinusoidal signal to obtain a constant current, involving different electrical parameters. In this context, this approach objective is to investigate the electro-mechanical interaction between the driving machine and the mechanical system.

The study of the defect impact on the current signal will start first by interpreting the temporal evolution of the current  $i_{ds}$  in different working cases.

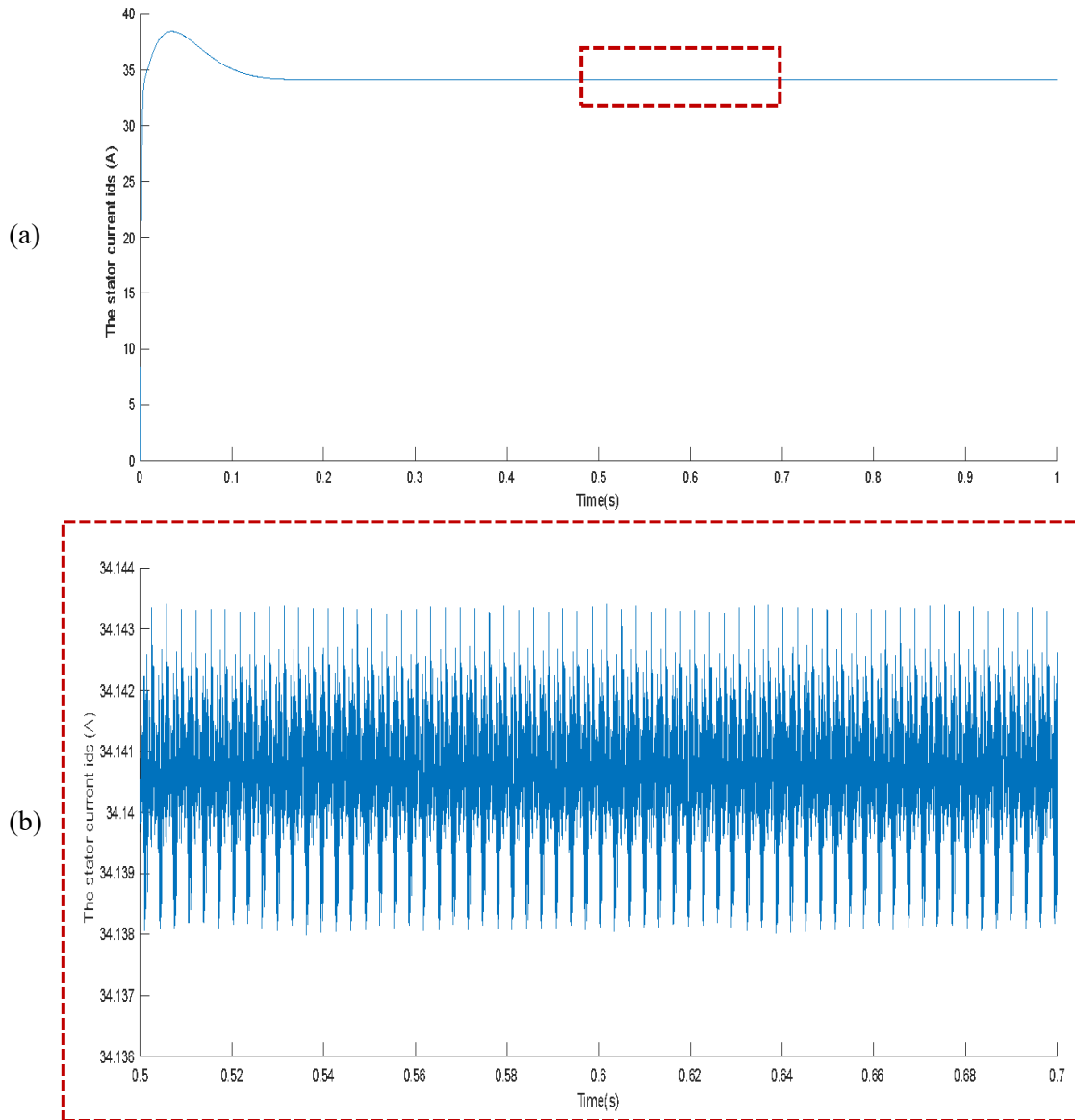


Figure.4.6: Current signal for healthy configuration: (a): The current signal in [0s,1s] and (b): Zoom of the current signal in [0.5s,0.7s]

Figure.4.6 illustrates the temporal evolution of the stator current  $i_{ds}$  obtained from the Park Transformation. The current signal is divided into two parts. The steady state which is the concern of this study and the transitional regime (1) that represents the run up of the motor. For this approach only results seen in the steady state are representative.

The appearance of the meshing frequency in the current  $i_{ds}$  is explained mathematically by the transmission of the sun velocity's signal as explained in the electromechanical interaction in equation (2.41). On the other hand, the meshing phenomena is transmitted to the motor as a load fluctuation which will affect the speed of the shaft and produce vibrations each time the planet accomplishes one relative

revolution. Hence, the simulated stator current obtained by the equivalent circuit is sensitive to the electro-mechanical interaction between the asynchronous motor and the gearboxes.

$$\text{Where } T_{mesh} = \frac{1}{F_{mesh}}$$

#### 4.2. Frequency domain responses

For the numerical model, in the ideal case, the motor is not supposed to present any behavioural imperfections, then deliver a perfect sinusoidal current. Therefore, the Frequency Spectrum of the phase Current is dominated only by the electrical frequency. For the healthy configuration, we applied the Fast Fourier Transformation (FFT) on the temporal signal seen in Figure.4.6 to obtain the frequency spectrum. It's Clearer in figure.4.7 which shows that the current spectrum  $i_{ds}$  is dominated only by the gear meshing frequency and its harmonics.

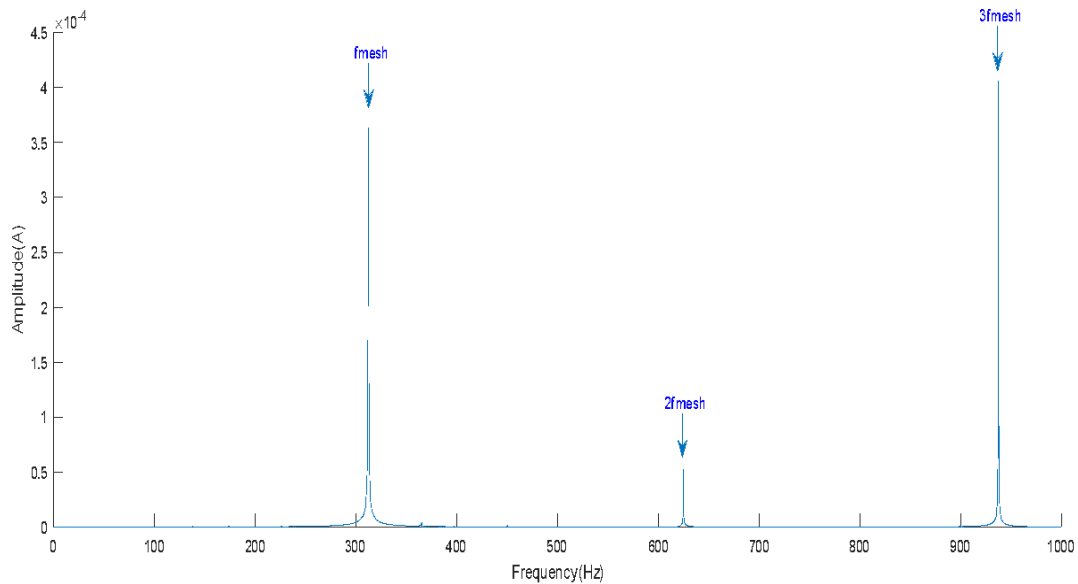


Figure.4.7: The Frequency Spectrum of the  $i_{ds}$  Current in the healthy configuration

To visualize the impact of the electromechanical interaction the inverse Park transformation has been used. The inverse Park transformation was applied on the simulated current  $i_{ds}$  to obtain the phase current. Correspondingly, Figure.4.8 illustrates the phase current frequency spectrum, which is dominated by the electrical frequency given as 50Hz in these simulations. Therefore, to highlight the frequency with low amplitude, Hanning window was used to plot the coming simulation results for the phase current. Besides, in the same figure it was noticed the appearance of the additional peaks related to the meshing frequency, which is given by the expression:

$$|f \pm n f_{mesh}| \quad (4.8)$$

Where  $n \in N^*$ ,

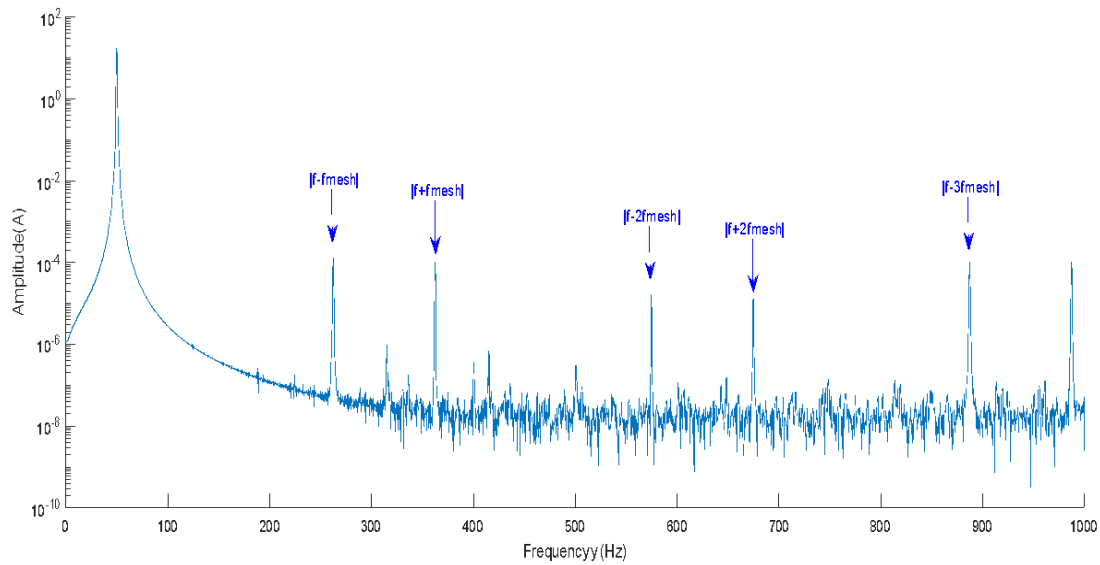


Figure.4.8: The Frequency Spectrum of a phase current in the healthy configuration

The torque oscillations can exist even in the healthy case because of space and time harmonics, this is what explains the related meshing frequency's harmonics appearance in the spectrum of the phase current simulated and shown in figure .4.8.

## 5. Conclusion

The mechanical system seen in chapter.3 composed of a planetary test bench of two stages of gears and an asynchronous machine was modelled based on the multiphysics numerical approach defined in chapter.2. The electrical model developed in the chapter.2 were used to describes the behaviour of the asynchronous motor of the test bench. For the double stage system, a torsional model was developed.

In the motor current frequency spectrum of the  $i_{ds}$ , the electromechanical interaction is seen throughout the dominance of the gear meshing frequency and its harmonics. The motor current signal shows that the load perturbation resulting from the meshing phenomena is totally seen in the appearance of the gear meshing frequency in the motor current signal. The inverse Park transformation was applied on current signal  $i_{ds}$  to presents the impact of the mechanical system on the phase current. These results of the numerical simulations will be exposed to a qualitative comparison to experimental measurement in the coming chapter.



## **Chapter 5:**

**The multiphysics investigations on  
the experimental testbench: motor  
current signal, vibrations level and  
acoustic pressure**



## **Chapter 5: The Multiphysics investigations on the experimental testbench: motor stator current signal, vibrations level and acoustic pressure**

### **1. Introduction**

In the previous chapters, a numerical investigation of the electromechanical interaction between an asynchronous motor and gearboxes was elaborated and two numerical models were used. In this chapter, the impact of the electromechanical system on the current signal will be investigated experimentally. The study will be divided mostly in two parts: the first part is orientated to the low-speed test bench. The specification in this part is the geared motor used. In this first part, the main target is to test the sensitivity of the electric clamp to mechanical perturbation and mainly the meshing phenomena.

The second part presents the study done on the double stages' planetary gearbox. Monitoring the planetary gearbox was performed through investigating the motor current signal, the vibration level and the acoustic pressure generated by the testbench. This part aims to present a comparative study between these signals to investigate the gears states and to highlight the sensitivity of the motor current signature to gears defects.

### **2. The phase Current response to the Low speed testbench**

In this study, the motor frequency was maintained to 30Hz ,18rpm. Two configurations were taken into consideration. The first configuration refers to a free motor. The figure.5.1, presents the current signal for a free motor. This signal was tracked in order to establish a reference situation and identify all the electrical system related frequencies in the current frequency spectrum.

## 2.1.The current signal for Free motor:

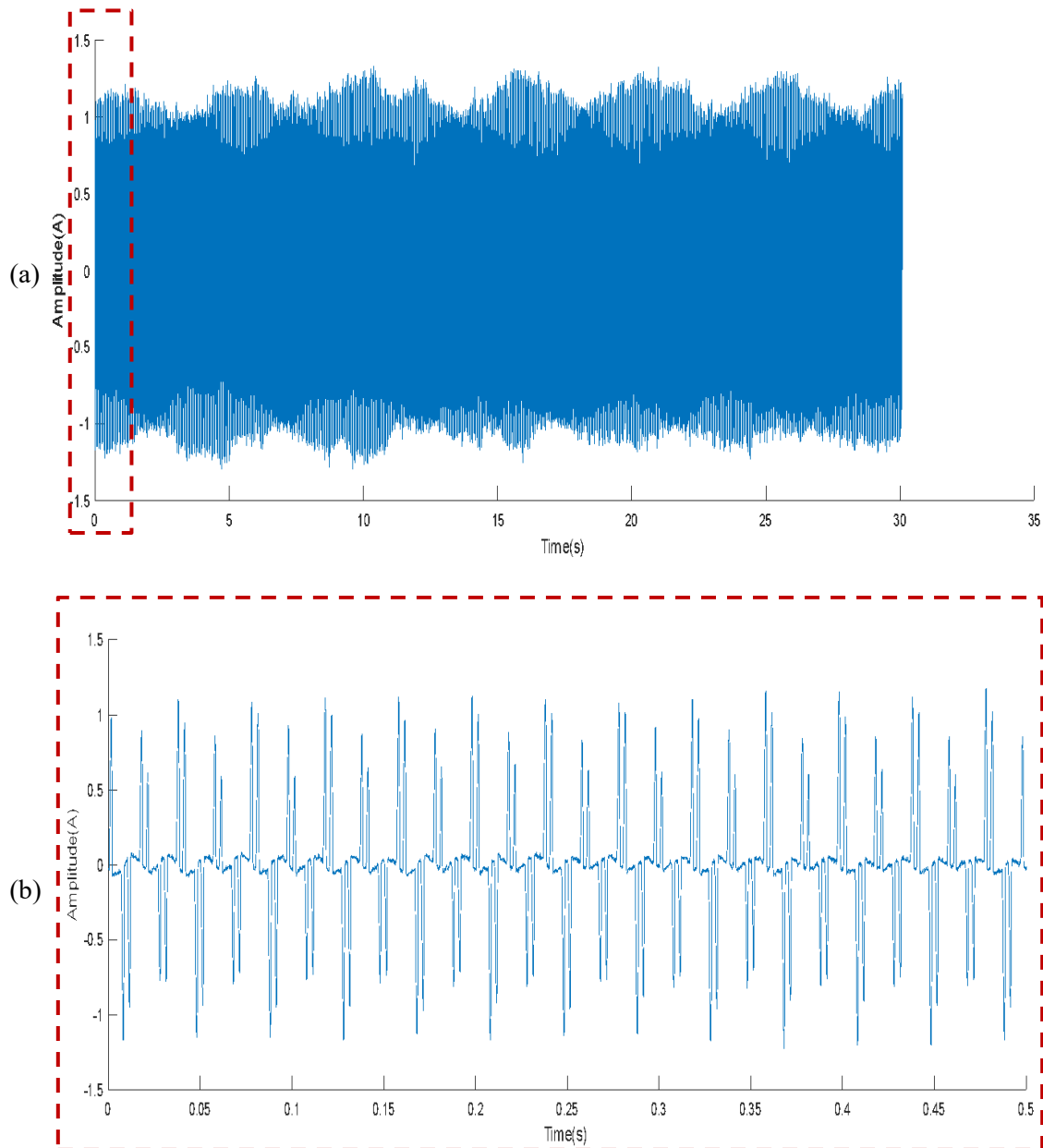


Figure.5.1: The current signal of a free motor: (a) in [0s,35s] and (b) zoom of the current signal in [0s,0.5s]

The figure.5.1 presents the current evolution in the temporal domain. The current signal seen is periodic, so to define the components frequencies Fast Fourier Transformation (FFT) is used. After applying the Fast Fourier Transform on the temporal signal, the figure.5.2 illustrates the current frequency spectrum for a free motor. It is seen that the current spectrum is dominated by the supply frequency given by 50Hz. With lateral sidebands related to the mechanical rotating frequency of the geared system. Meanwhile in order to accentuate the appearance of the mechanical system's signature in the measured current figure.5.2 showing the same results in the logarithm scale. It is totally seen the appearance of additional frequency besides the previous one explained. In the figure 5.2 the use of a logarithmic

scale has provided better data visualization and has made it easier to spot patterns and identify different components. The current spectrum is dominated by the supply frequency and its harmonics.

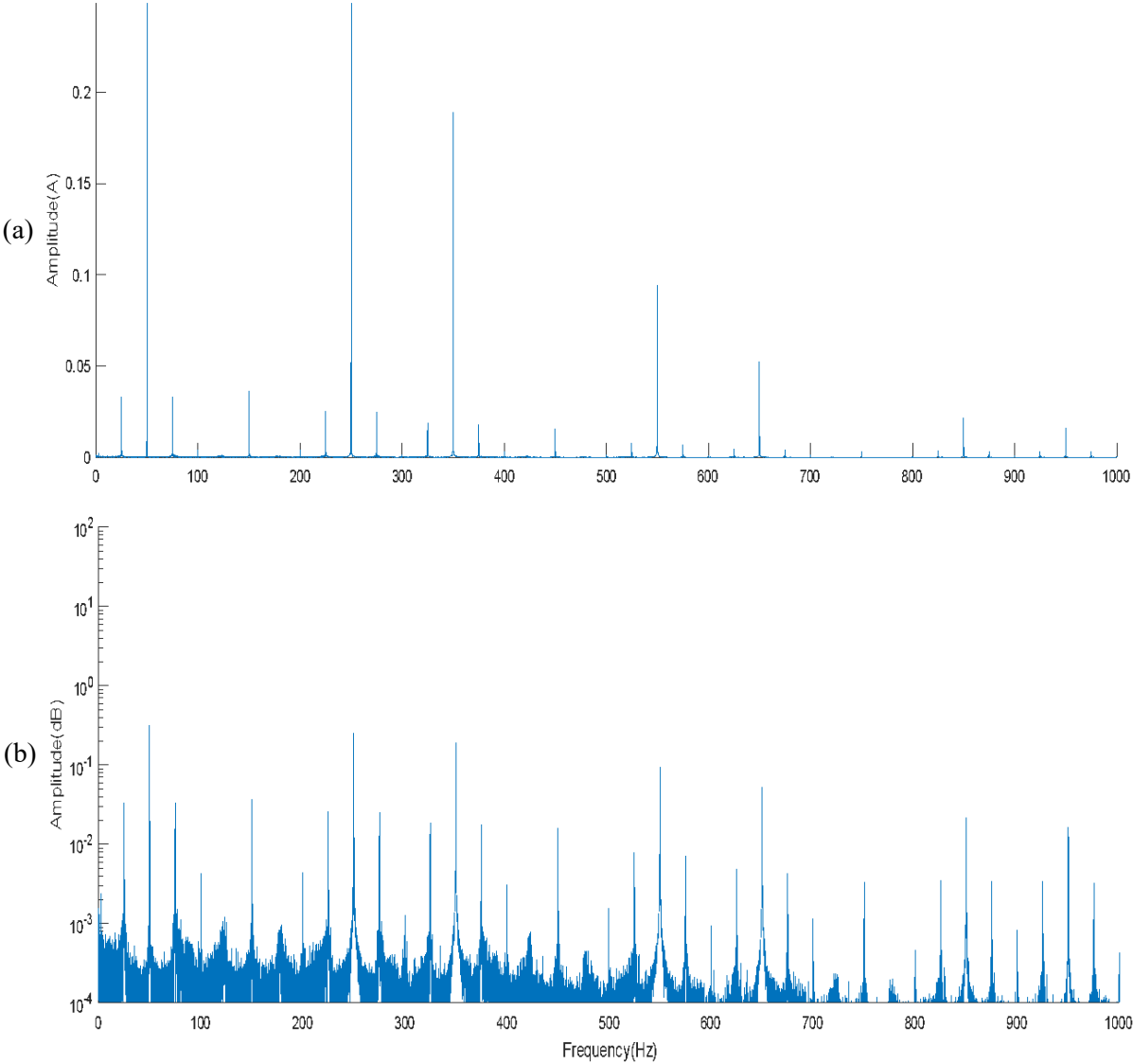


Figure.5.2: The frequency spectrum of the current signal for free motor

linear scale (b) logarithmic scale

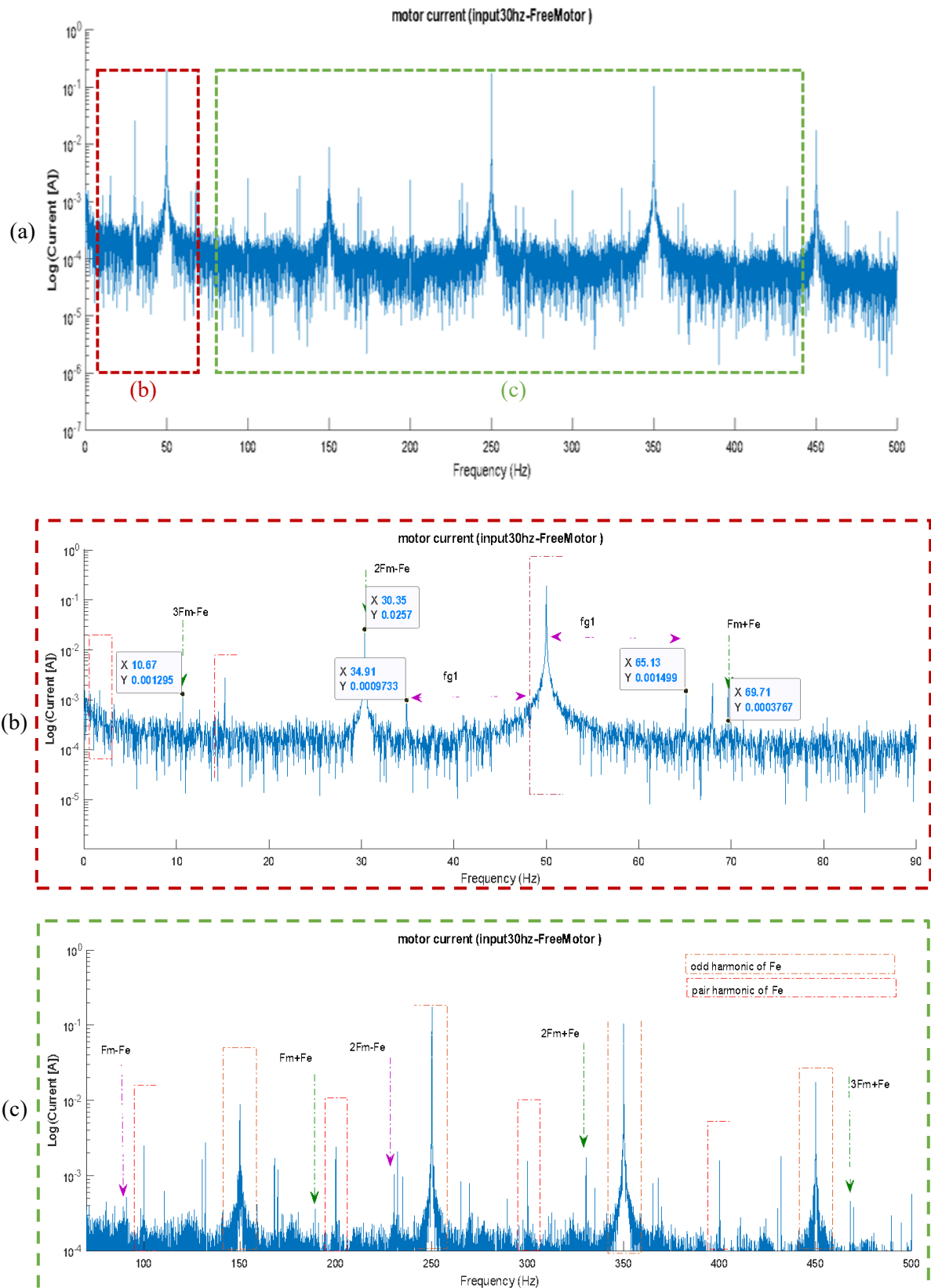


Figure.5.3: The current frequency spectrum highlighting the impact of the gearbox connected to the motor. (a) : [0Hz, 500Hz] ; (b)[0Hz,90Hz] ; (c)[90Hz,500Hz]

Besides to the frequencies seen in the figure 5.2 related to the electrical machine, the figure.5.3 presents the current frequency spectrum with emphasizing the electromechanical contact.

It is seen in the figure.5.3 that the connection of the gearbox to the motor impacts the current signal by the presence of the gear meshing frequency of each stage. Whenever there is a load fluctuation, a change in speed occurs thus changing the per unit slip, which subsequently causes changes in sidebands across the line frequency  $f_e$ . The figure.5.3(c) highlights the appearance of the mechanical impact of the gears through the gear meshing frequency. The peaks seen in the current frequency spectrum are presenting the relate gear meshing frequency as given in the expression:

$$f_{ri} = |f_e \pm mf_{mi}| \quad (5.1)$$

Where:  $i$  refers to whether the 1<sup>st</sup> or the 2<sup>nd</sup> stage of the integrated gearbox and  $m \in N$

Even though, with a weak amplitude, even related mechanical frequencies can be seen in the figure.6(b), and those frequencies are given by:

$$|f_e \pm mf_{m1} \pm nf_{m2} \pm pf_{g1}| \quad (5.2)$$

Where:  $m, n, p \in N$

## 2.2.The current signal after coupling the motor to the gears

The figure.5.4 presents a brief comparison between the frequency spectrum of the current signal for free motor (drawn in blue) and for a motor connected to the mechanical system, pair of helicoidal gears (presented in green). Besides to the related frequency seen in the figure.5.3, it is totally foreseen the appearance of additional frequencies related to the rotating frequencies and the meshing frequency as well.

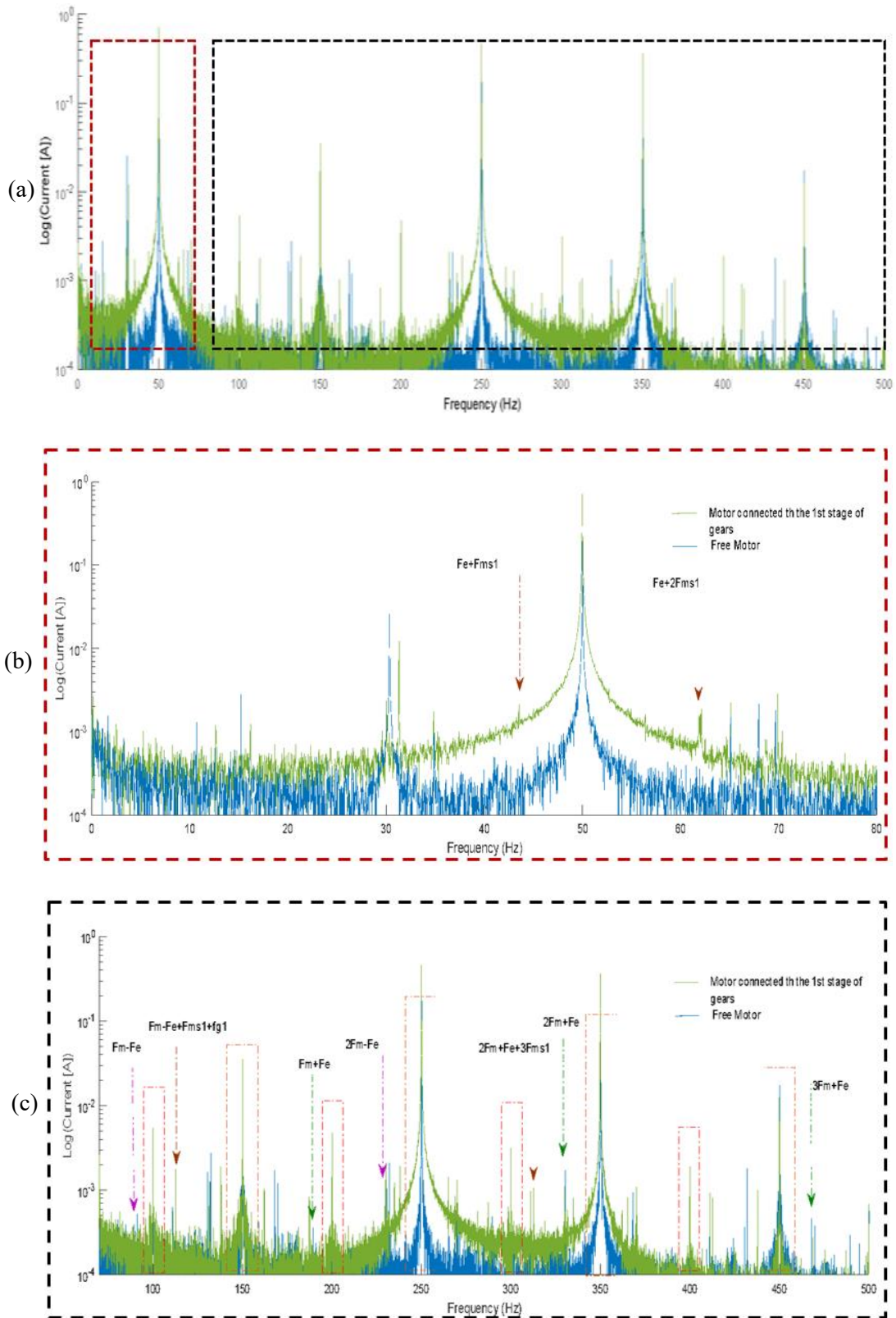


Figure.5.4: The current spectrum while the motor is connected to the helical pair of gears.

Where  $F_{ms1}$  is the meshing frequency of the mechanical system.

The figure.5.4(b) presents the appearance of peaks in the significant frequencies  $F_e + F_{mesh}$  and  $F_e + 2F_{mesh}$ . In fact, the illustration of this last measurement has for objective to emphasise the sensitivity of the electrical signals in mechanical connections detection as shown in the figure.5.4(c). Also, it is seen the increase of the amplitude of all the peaks related the related-mechanical frequencies which was related to the high load introduced for the second configuration.

### **3. Multiphysics study of the behaviour of the Planetary gearbox testbench**

For the planetary gearbox testbench, a Multiphysics study took place during the experimental tests. The comparison study aims to define the sensitivity of the motor current signature method in the monitoring uses in the planetary gearbox. Tests were done in different operating conditions of load and speed. However, the results that will be shared in this part were elaborated simultaneously for supply frequency given 50Hz ,1490rpm and 300N.m as external load.

#### **3.1.The motor phase current signal**

In order to track the impact of the dynamic behaviour of the planetary gearbox on the current signal, we defined first an initial signal that corresponds to the phase current signal before coupling the asynchronous motor to the mechanical system.

##### **3.1.1. Current signal for Free motor**

In the ideal case, the current of one phase is considered perfectly sinusoidal. Therefore, it presents a lot of imperfections which can be related to the sector or the power supply [72]. Figure.5.5 below illustrates the frequency spectrum for free motors, showing the fundamental frequency (line frequency) at 50Hz. Besides the fundamental frequency, we notice the presence of the harmonics (2<sup>nd</sup> ,3<sup>rd</sup> ,4<sup>th</sup> and 5<sup>th</sup>). These harmonics are probably related to variation of motor load, inertia, torque, supply voltage, or speed oscillation of motor [68].

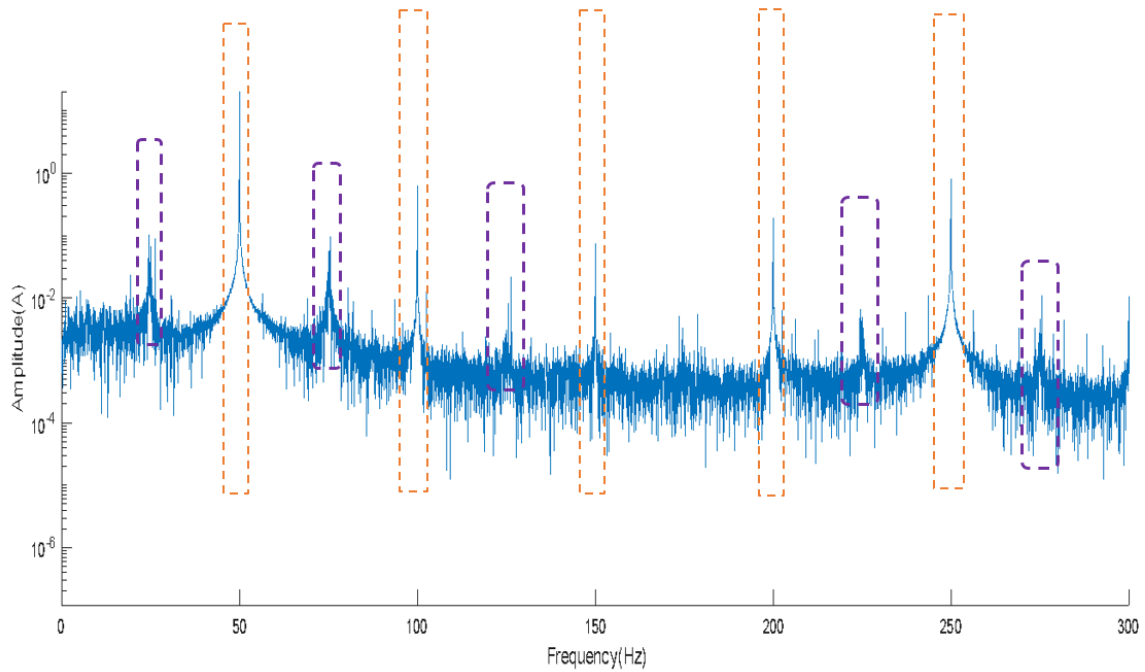


Figure.5.5: The frequency spectrum of the current signal for free motor

Within the same context, besides the supply frequency and its harmonics, the current spectrum in figure.5.5 shows additional frequencies with important amplitudes. Although the motor is, theoretically, supposed to be well built; its assembly is impossible without getting a minimum residual eccentricity. In addition, the process of alignment of motor and load will never be perfect. Hence, additional forces will appear increasing the eccentricity of the rotor. On the other hand, the state of wear and the characteristics of the bearing seat will also influence the position of the rotor within the static housing. The combination of all these events will lead to an eccentricity phenomenon, which involve static and dynamic eccentricity. The coexistence of static and dynamic eccentricity will give rise to harmonics (25.5Hz and 74.5Hz) given by the equation (17) for  $n=1$  even in healthy motors [69].

$$f_{ecc} = f_e \pm n f_r \quad (5.3)$$

Where  $n=1,2,3,\dots$

It has been demonstrated experimentally that if the amplitude of these harmonics is over 50 dB smaller than the fundamental frequency component amplitude, the rotor may be considered healthy [70].

### 3.1.2. The impact of the planetary gearbox on measurements

Figure.5.6 shows the impact of the gearboxes on the spectra of the current signal. The results are plotted for the free motor (in blue) and for the current after connecting the motor to the test bench (in red). The comparison between the current signals confirms the presence of additional peaks which correspond to key frequencies of the planetary gearboxes. For a supply frequency given 50Hz, 1460rpm.

The existence of the mechanical frequencies in the motor current signal is seen as a modulation of the supply frequency (given 50Hz). The figure5.6(b) shows components related to gear meshing frequency:  $|f_e \pm f_{mesh}|$ . The amplitude of the related meshing frequency is not important ( $2.10^{-3}A$ ) comparing the rest of peaks mechanical frequency. This emphasises the fact that the motor current signature analysis is a technique that detects more low frequencies. Likewise, figure5.6(c) shows sidebands around the fundamental frequency which confirms the influence of each mechanical component. The fact that carrier frequency and its harmonics have noticeable amplitude at:  $|f_e \pm nf_c|, n \in N$  is explained by the effect of carrier gravity [73].

In addition, the movements of the sun are transmitted through the input shaft to the motor affecting the current signal as well. This is well observed by the presence of sun related frequencies:  $|f_e \pm f_s|$ . Hence, we notice the presence of the relative planet frequency  $|f_e \pm f_{pc}|$  with an important amplitude. In fact, the presence of this frequency is related to some mounting problems in one of the planets. These frequencies are confirmed by vibrations' signals obtained simultaneously while measuring the current signals

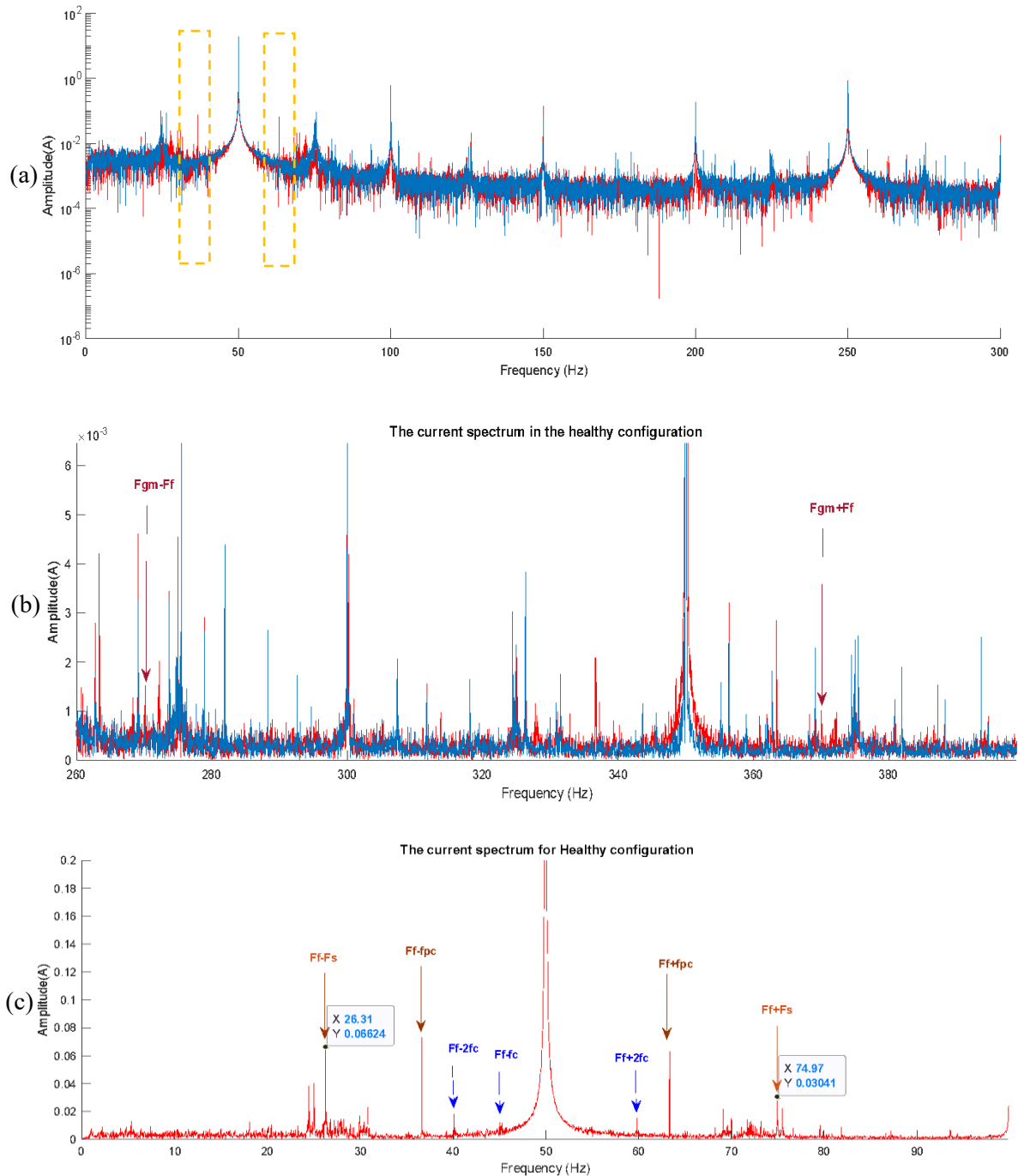


Figure.5.6: The frequency spectrum current signal (blue: for free motor, red: the motor is already connected to the planetary gearbox) ;(a) Zoom in frequency range [0Hz;300Hz] (b) Zoom in frequency range [260Hz;400Hz] (c) Current signal in the presence of defect [0hz;100hz]

### 3.2.The vibrations signal

The phase current signal was recorded simultaneously with the acceleration of the test ring. The accelerometer was fixed as seen in the figure.3.4 on the test ring. The figure.5.7 presents the vibrations

level on the test ring. The frequency spectrum shows the appearance of the gear meshing frequency  $F_{mesh} = 320.6\text{Hz}$ .

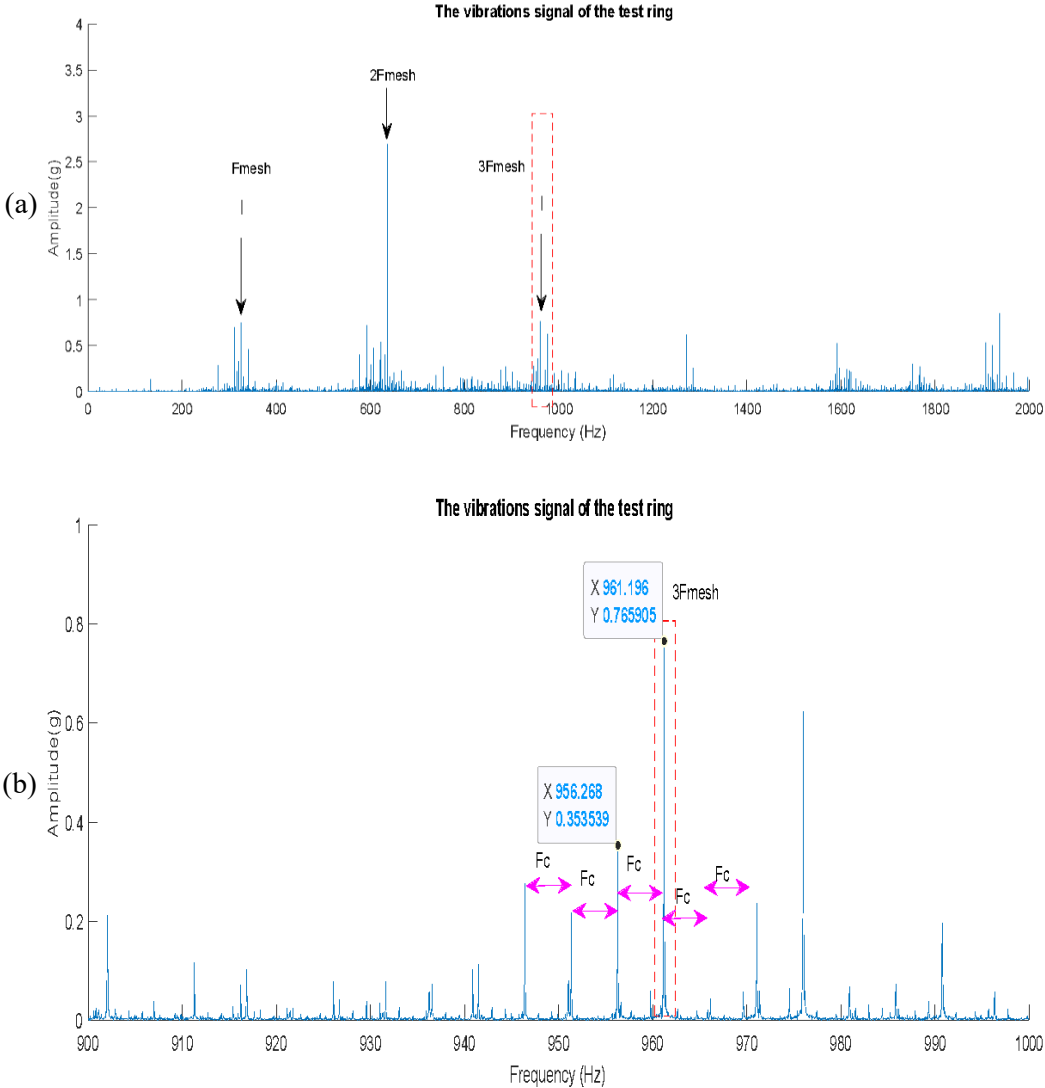


Figure.5.7: The frequency spectrum of the vibrations signals: (a) The frequency spectrum in [0Hz, 2000Hz] and (b) Zoom of the frequency spectrum of the vibrations signal in [900Hz,1000Hz]

The spectrum above seen in the figure.5.7 (b) presents the appearance of the carrier frequency excited by the mesh frequency and its harmonics. The appearance of the carrier frequency, its modulation and its harmonics can be related to a possible misalignment error on shaft connecting carriers. Also, sidebands around mesh frequency and its harmonics are observed.

### 3.3.The Acoustic pressure of the mechanical system

The acoustic pressure of the mechanical system was measured at the same time with the vibrations signals seen above. In figure.5.8, the frequency spectrum of the acoustic pressure is recorded using microphone1. The motor was isolated using Foam to minimise the sound level related to the electrical device.

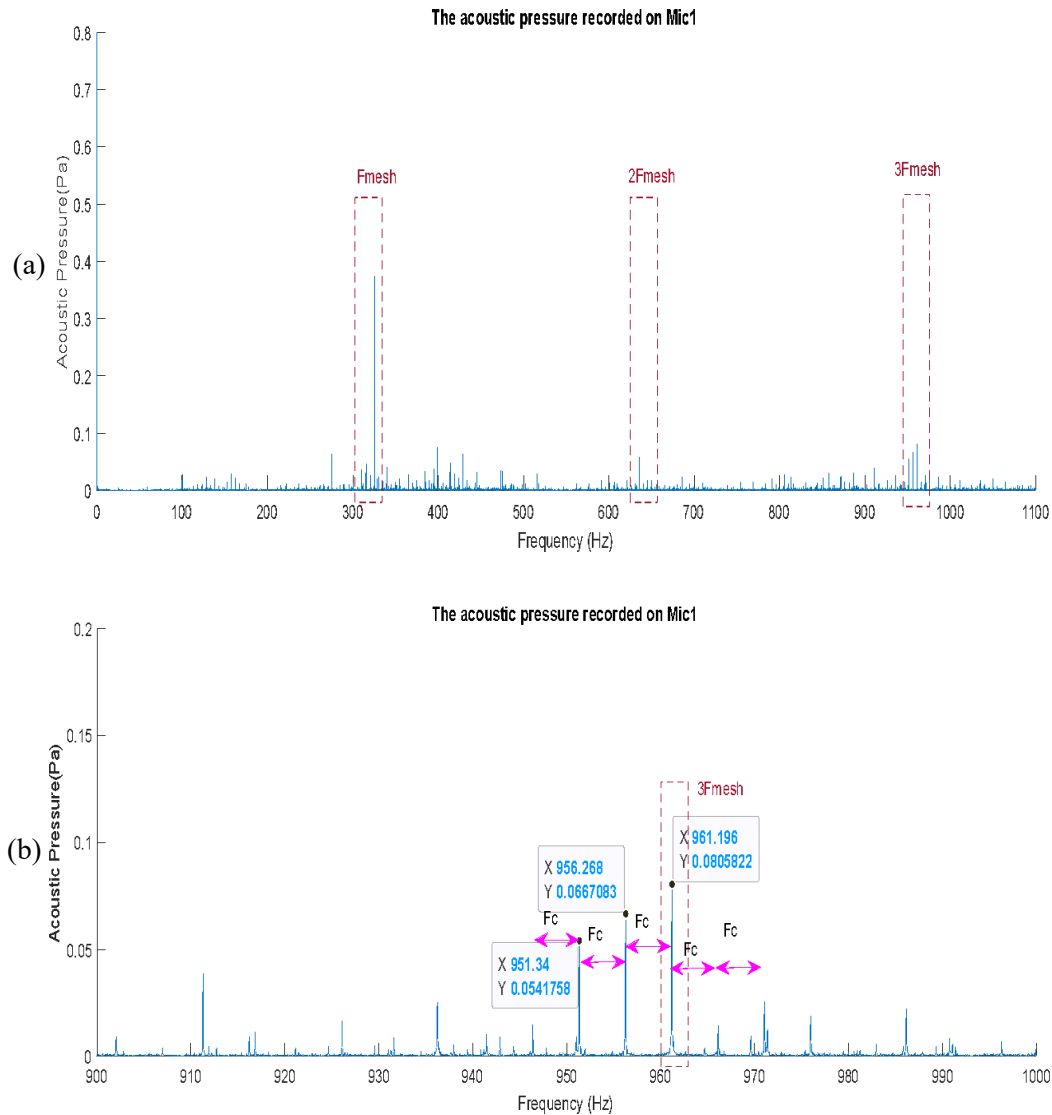


Figure.5.8: The frequency spectrum of the acoustic pressure: (a) the signal in [0Hz,1100Hz] and (b) Zoom of the acoustic pressure spectrum in [900Hz, 1100Hz]

As observed in the vibrations level, the frequency spectrum seen in the figure.5.8, the signal is dominated by the gear meshing frequency and its harmonics. Also, the appearance of the carrier frequency in sidebands of the meshing frequency are related to the periodic movement of the carrier. The acoustic pressure is considered a performed tool in detecting the planetary gearbox dynamic behaviour. As proved by Pablo *et al.* [74], the pressure acoustic is a significant signal in highlighting the meshing frequencies better than the intensity.

#### 4. Conclusion

In this chapter, the experimental results were taken in order to study the impact of the gear meshing phenomena on the Phase current signal. It was totally foreseen that the impact of the mechanical behaviour on the phase current is seen in two parts. First by the appearance of the key frequencies of the

carrier and the planets. Second the meshing frequency appears as modulation to the supply frequency. On the other hand, the current signal outcome was compared to the vibrations level and the acoustic pressure measured simultaneously. It has been proven in this chapter, that the electric clamps are efficient to investigate the dynamic behaviour of the planetary gearbox.



## **Chapter 6:**

# **The impact of gears defect of the dynamic behaviour of the planetary gearbox and the electro-mechanical interaction**



# **Chapter 6: The impact of the gears defect on the planetary gearbox's dynamic behaviour**

## **1. Introduction**

In the previous chapter, an investigation on the impact of the mechanical model on the current signal was elaborated. The response of the phase current to the behaviour of the mechanical system was presented by means of numerical simulations and experimental measurements. The work seen was a preliminary Multiphysics interaction between the electrical device, seen as an induction machine and the planetary gearbox. Therefore, in this chapter, gear teeth defect will be implemented. First, numerical results will be visualized after introducing the defect. Later, experimental measurement of the phase current, the vibrations level and the acoustic pressure will be shown in order to present a deep qualitative comparison between experimental and numerical outcomes.

## **2. Numerical study of the tooth crack on the motor current signal**

The appearance of any geometric defect impacts the behaviour of the mechanical system and generates a functioning perturbation. The mesh stiffness of the gear system will decrease gradually with the surface crack propagation [75].

### **2.1. Numerical modelling of Tooth crack**

The teeth defect directly impacts the gear meshing frequency. In this case, it presents a decrease of the amplitude of the meshing stiffness periodically with angular frequency  $\omega_{def} = \frac{2\pi}{T_{def}}$ . This decrease is explained by the loss of contact while the defected tooth meshes and on the localisation of the defect. The impact of the defect is affected mainly by the number of times the defected tooth meshes. The figure.6.1 presents the impact of the teeth defect on the planet gear in the planetary gearbox system presented in the chapter.3.

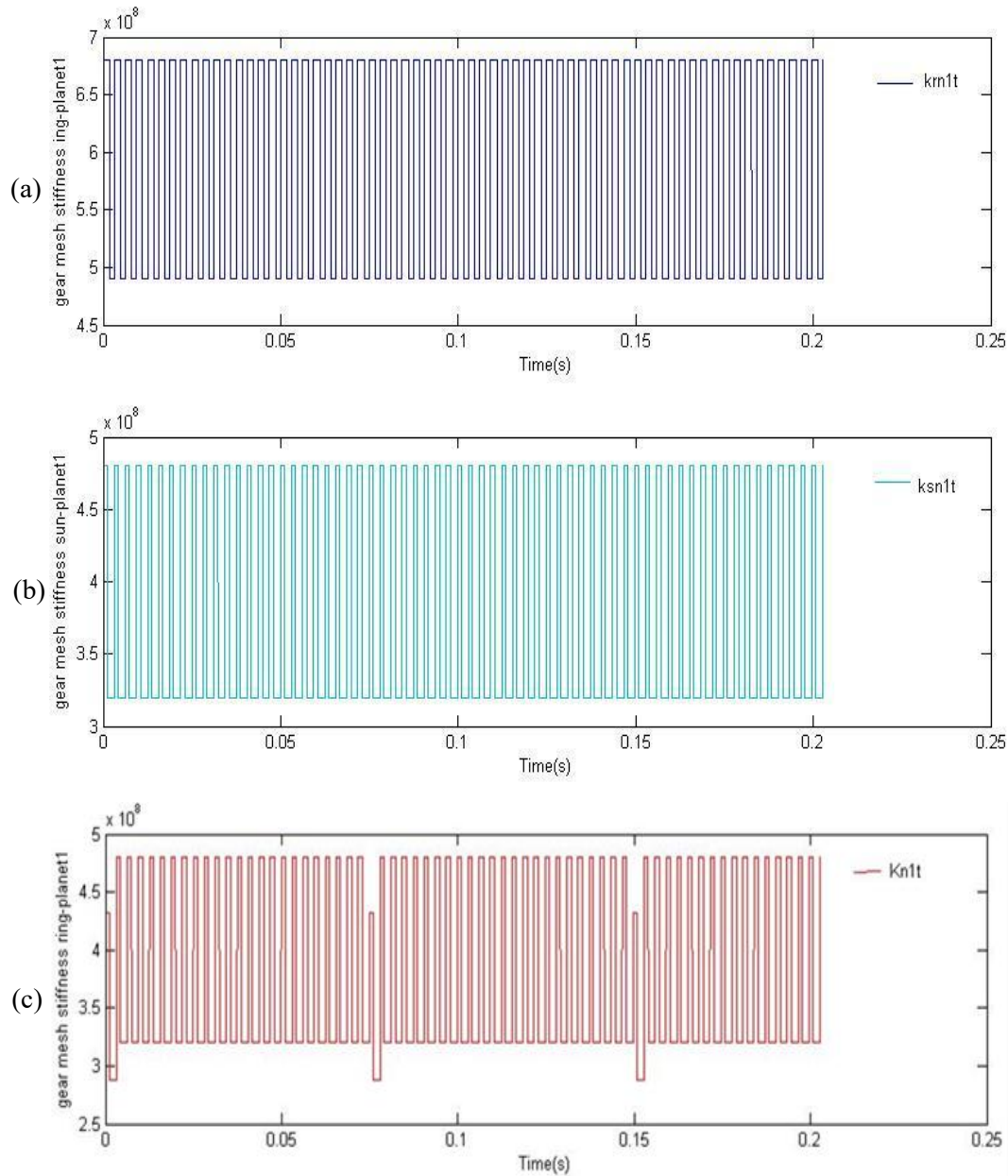


Figure.6.1: The gear meshing frequency: (a)The gear meshing stiffness for the healthy configuration ring-planet1 ; (b) The gear meshing stiffness for the healthy configuration sun-planet1; (b) The impact of the tooth defect on the gear meshing stiffness ring-planet1

## 2.2.Motor current signal response in the presence of tooth crack in planetary gearbox: Temporal response

In this part, the simulated current signal will be presented in the defected configuration. The crack will be placed each time differently on a gear in order to observe the sensitivity of the model to different localisation of defect.

### 2.2.1. Sun defect

The crack is supposed to be implemented on the sun. Besides to the fluctuation seen in the current signal due to the gear meshing, figure.6.2 shows clearly the presence of variety in amplitude of the stator current  $i_{ds}$  in the presence of sun tooth defects. The time variation shows current modulation with periodicity  $T_{ds}$  given by:

$$T_{ds} = \frac{1}{F_{ds}} \quad (6.1)$$

$$F_{ds} = N(f_s - f_c) = \frac{Nz_r}{z_r + z_s} f_s \quad (6.2)$$

where:  $f_s$  is the sun frequency and  $f_c$  is the carrier frequency and  $F_{ds}$  is the defect of the sun. Meshing defected teeth generate additional load which makes the system partially overloaded. Therefore, the increase of the current amplitude when the defected tooth gets in contact each time is explained.

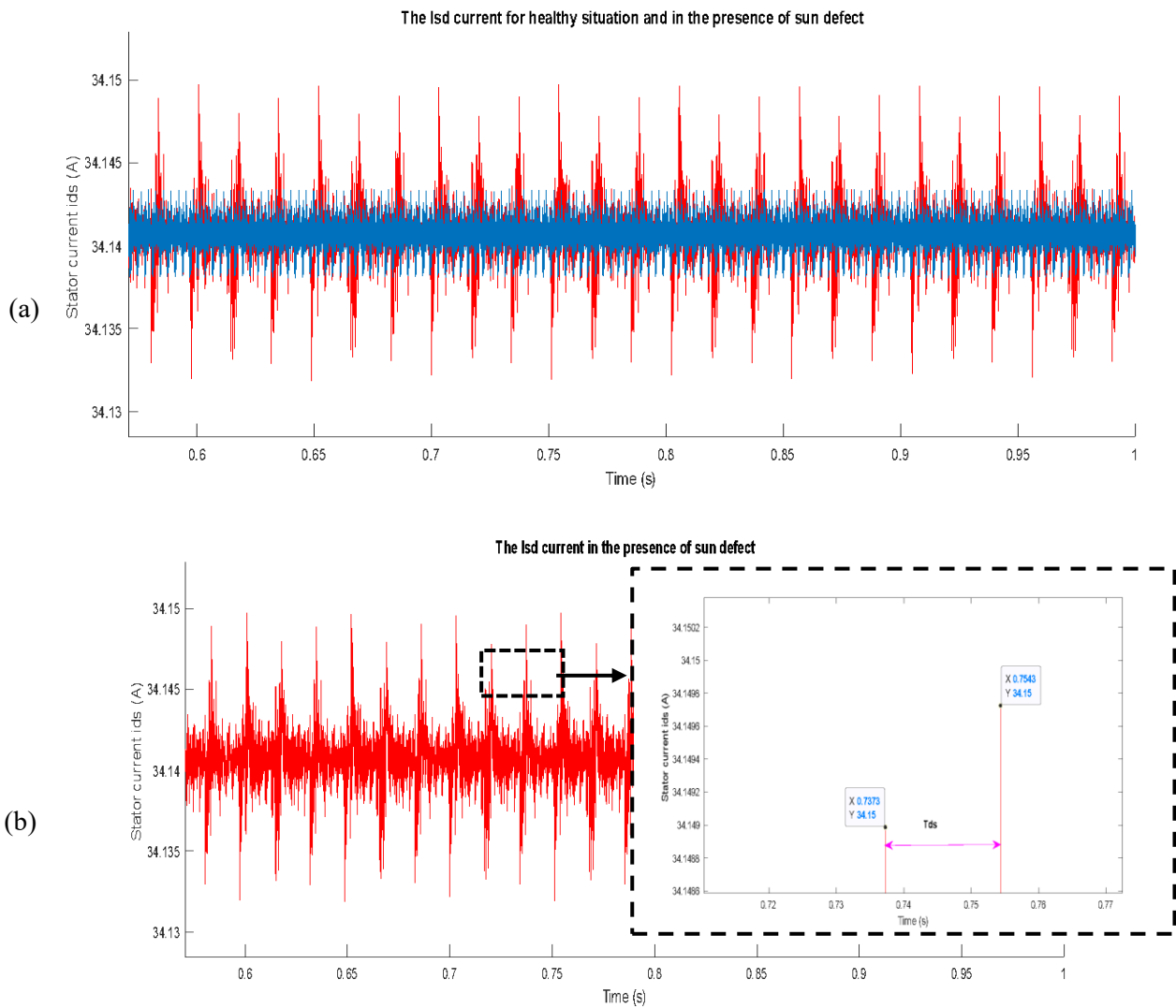


Figure.6.2. Temporal evolution of the current signal  $i_{ds}$  (a): Comparison between the healthy configuration and the defected case, (b): Current signal in the presence of sun defect

### 2.2.2. Planet defect

The impact of the planet defect on the signal depends on its localization. Therefore, two different cases are assumed: The defect is present in one side of the planet, or it is present in both sides. The defected side of the damaged tooth that gets in contact with the sun presents a modulation in the recorded signals once each revolution of the planet  $T_{dp}$  as illustrated in the figure.6.3. So, the defect on the planet would be seen by its frequency given by:

$$T_{dp} = \frac{1}{F_{dp}} \quad (6.3)$$

$$F_{dp} = \frac{F_m}{z_p} = \frac{z_s z_r}{z_p(z_r + z_s)} f_s \quad (6.4)$$

The same defect is applied from both sides of the same tooth. When the sun is in contact with the surface A, this contact will produce a modulation in the current signals as it was explained in the case of a tooth defect from one side so that the defect A will appear each  $T_{dp}$  [76].

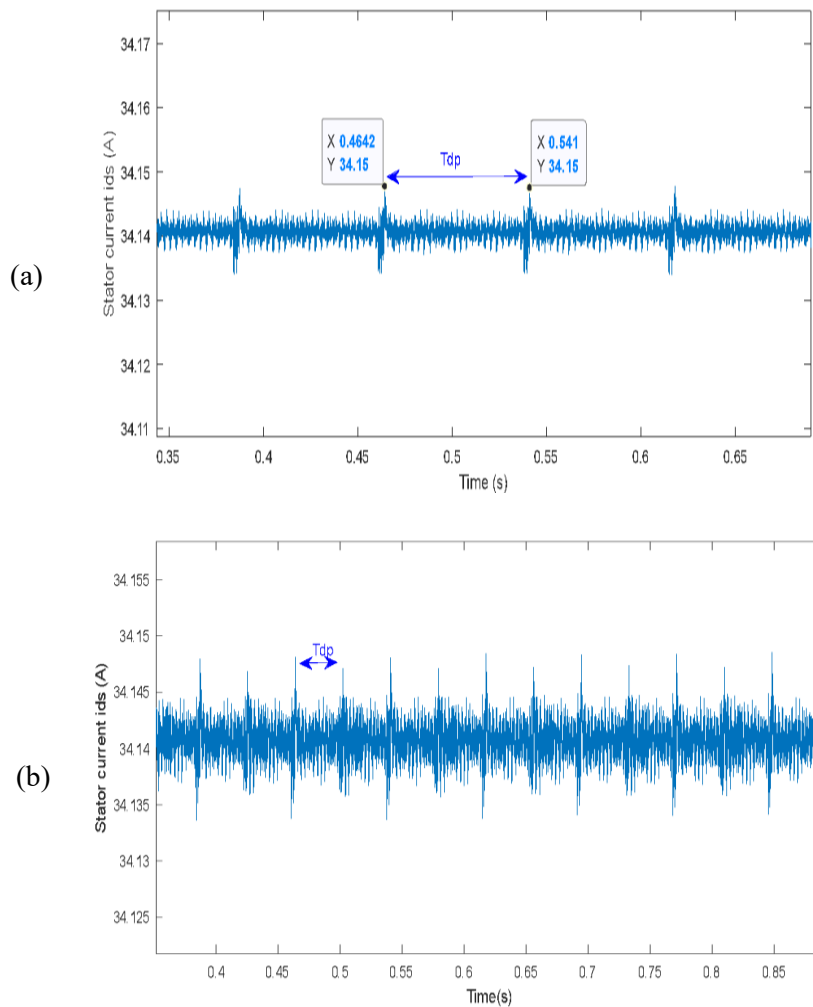


Figure.6.3: Temporal evolution of the current signal  $I_{ds}$  for planet defect; (a): the current signal for one face defect; (b): the current signal for double face defect

After a half of revolution of the planet, the defected tooth will be in contact with the ring tooth but with the surface B this time, which will be seen itself in the current spectrum by the same frequency. Although both defects will not provide peaks with the same amplitude as it is shown in the figure.6.3(b), in one revolution of the planet the tooth defect is signed twice as it is given by:

$$F_{dp} = 2 \frac{F_m}{z_p} = 2 \frac{z_s z_r}{z_p(z_r + z_s)} f_s \tag{6.5}$$

**2.3.The frequency spectrum of the stator current in the presence of tooth defect**

For the numerical model, in the ideal case, the motor is not supposed to present any behavioural imperfections, then deliver a perfect sinusoidal current. Therefore, the Frequency Spectrum of the phase Current is dominated only by the electrical frequency.

**2.3.1. The impact of the Planet Defect on the frequency spectrum:**

Figure.4.12 presents the frequency spectrum of the current signal in the presence of a planet defect. It is seen that besides to the appearance of the gear meshing frequency and its harmonics, figure.4.12 illustrates the appearance of additional frequencies due to the defect included in n the defect in the frequency spectrum of the  $i_{ds}$  current.

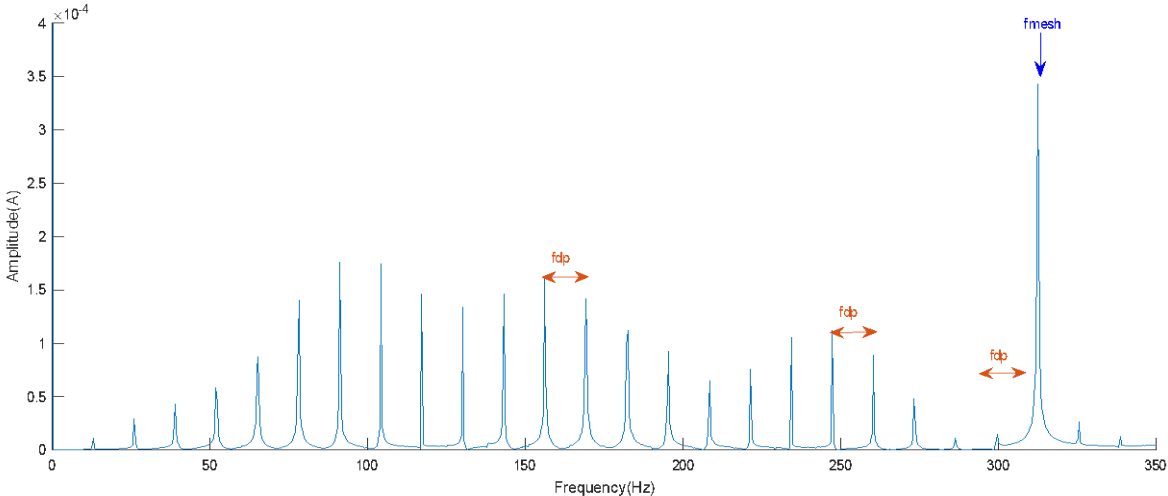


Figure.6.4: The Frequency Spectrum in of the Ids Current in the presence of planet defect

Thomson has shown in [77], that the appearance of a defect in the mechanical system produces a load fluctuation, which causes some speed oscillations that modulate the current input. In that regard, Figure.6.5 presents the phase current obtained from the current shown above. In fact, the vibrations produced by a defect of a mechanical component acts on the induction machine as a torque ripple  $\Delta T_i(t)$  which would produce a speed ripple  $\Delta \omega_i(t)$ .

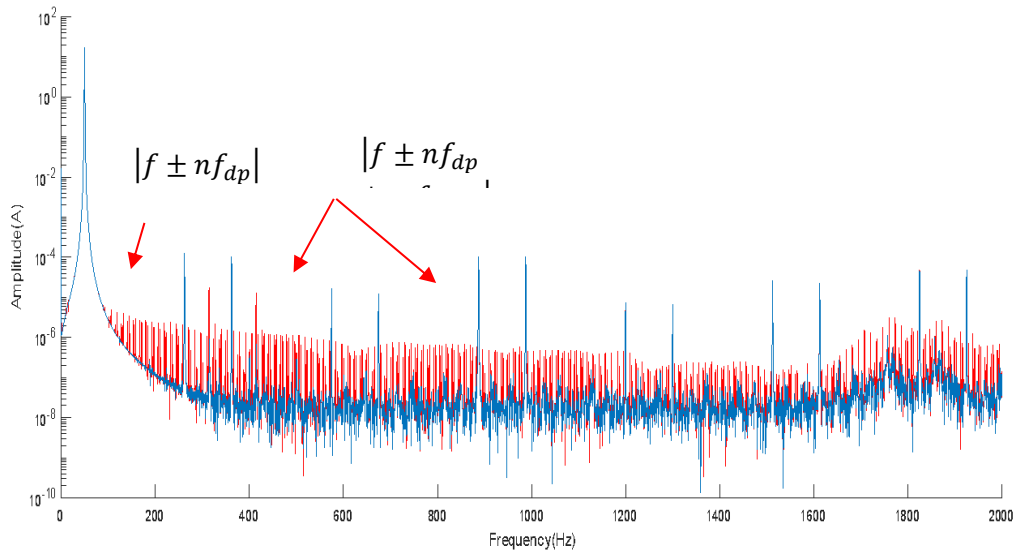


Figure.6.5: The Frequency Spectrum of the phase Current in the presence of planet defect (Red: in the presence of the defect; Blue for the healthy configuration) (numerical simulations)

Hence, the consequent mechanical angular variation will generate an angular fluctuation in the magnetic flux of the device and since the induction machines are considered symmetrical systems because of the magnetic rotating field, the appearance of any anomaly will impact the symmetrical properties. The planet defect affects the phase current by modulating the electric frequency. Therefore, we justify the appearance of the related defect frequency modulated by the supply frequency and modulated by the mesh frequency.

$$|f \pm n f_{dp}| \tag{6.6}$$

$$|f \pm n f_{dp} \pm m f_{mesh}| \tag{6.7}$$

### 3. The experimental study of the impact of gears defect

The experimental measurements were taken place in order to present a qualitative comparison between the results found numerically and the real outcome from measurements. Also, the impact of tooth defect on the current signal will be compared to the vibrations level in order to highlight the sensitivity of the phase current to the condition monitoring of the planetary gearbox.

#### 3.1.The implementation of the teeth defects in planetary gearbox testbench

The experimental measurement was taken according to the geometrical status of the gears set. Hence, in this part different configurations are exposed as seen below:

- **A reference set of gears seen in the figure.6.6:** this configuration presents the gearboxes in healthy conditions. This state will be a reference in the experimental measurements.
- **A degradation set of gears:** For this configuration new manufactured gears were used without any surface treatment. These gears were runed for forty hours to ameliorate the surface rugosity of the planets. This operation had generated a micro pitting as seen in the figure.6.6. This configuration will be used to study the effect of the degradation of the current signal.
- **The defected set of gears:** The study taken place in this work is based essentially on tracking the impact of gears defects on different phenomena. Therefore, in this state of gears we will introduce different gear defects to highlight the sensitivity of the motor current, the vibrations signal in recording any geometrical perturbation in the mechanical system. Defects were made artificially by electro erosion. The first defect is a pitting introduced on the root of one of the planets. The cut was done along the length of the tooth, with a depth and a width equal respectively to 2mm and 5mm. The second defect is implemented on the sun as seen in figure. a crack was introduced of depth of 3mm.

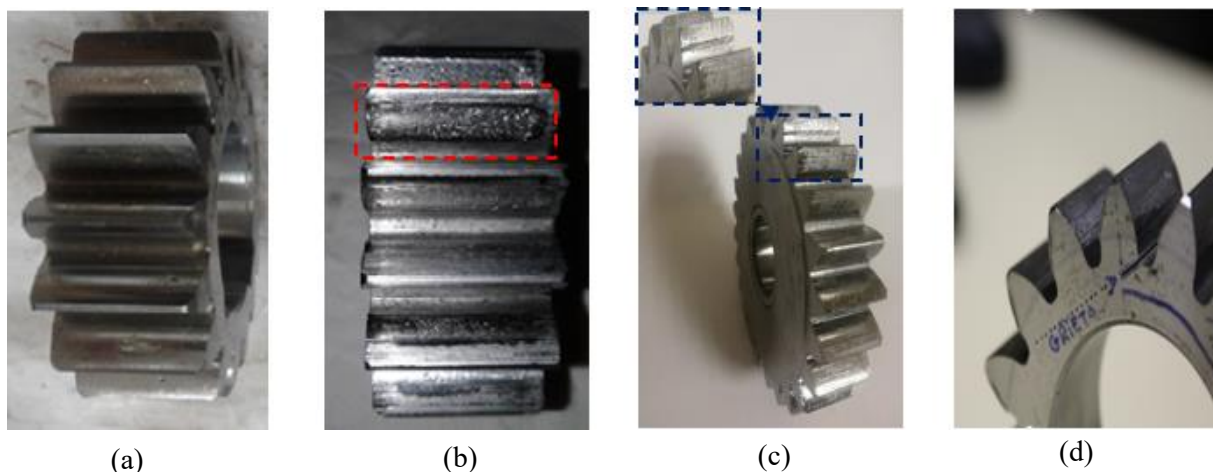


Figure.6.6: Different gears defects: (a) Healthy configuration, (b) wear degradation, (c) planet defect and (d) sun defect

### **3.2.The impact of the tooth defect on the MCSA, Vibration's level and the acoustic pressure to gears tooth crack**

After implementing the teeth defect on gears, different measurements have been taken. The motor frequency was maintained at 50Hz. The phase current signal will be compared to the acoustic pressure and to the vibrations level. The objective beyond this comparison is to highlight the sensitivity of the current clamps in detecting teeth defects.

### 3.2.1. The impact of the planet defect on the temporal measurement

In this section, the effect of a crack on different measured signals is studied. Figure.6.8 presents the current, vibration and acoustic pressure signals for this defect. The impact of this defect can be observed with different degrees of clearness for the 3 signals.

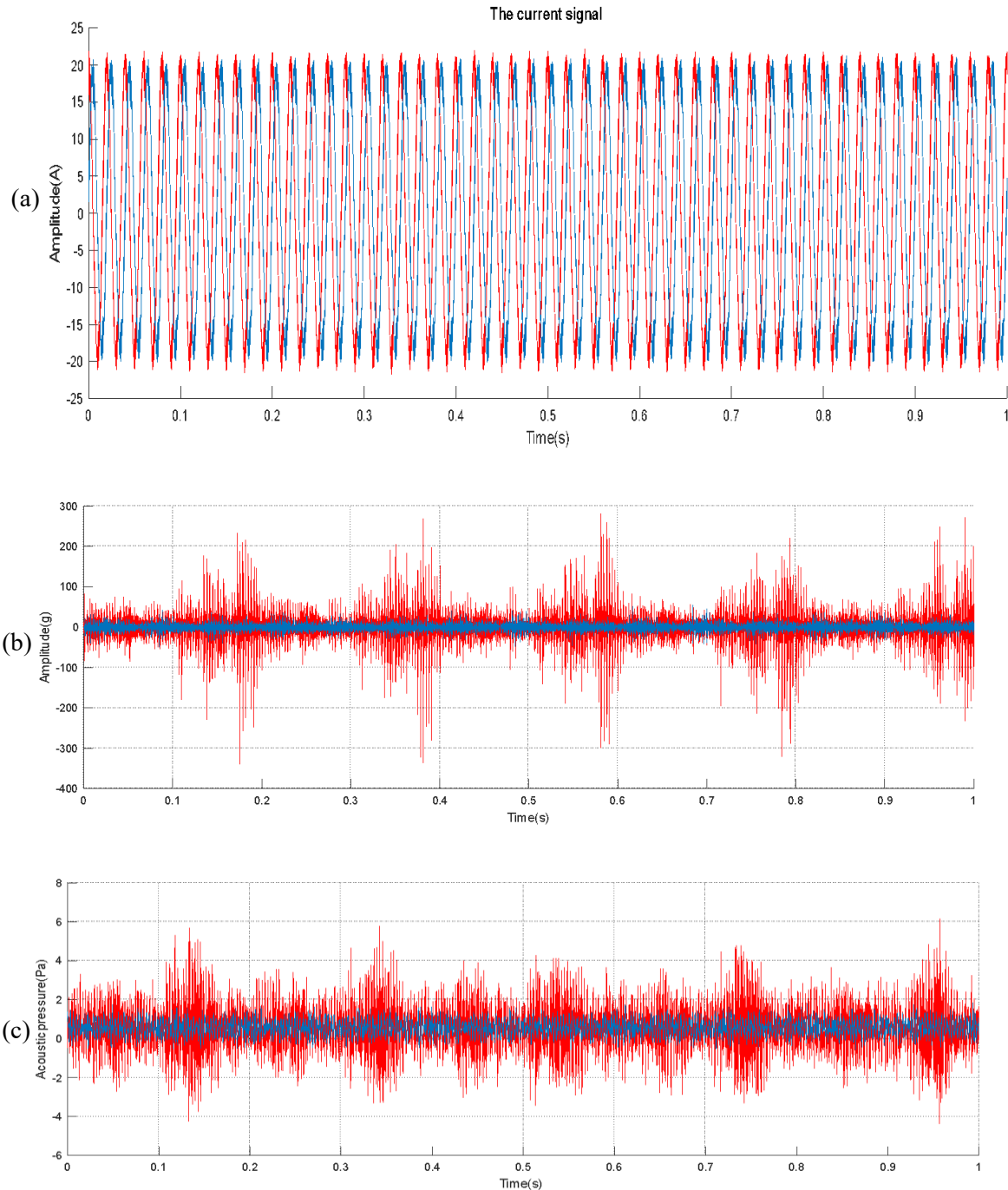


Figure.6.7: Temporal signal of the measurements (Red: Signal in the presence of defect; Blue: Healthy configuration): (a)The current signal; (b) The vibration signal of the test gearbox; (c) The acoustic pressure

Introducing the planet defect has impacted the vibrations signals and the acoustic pressure as highly seen in the figure.6.7 for the signal in the temporal domain by the increase of the amplitude periodically. However, the impact of the planet defect on the current time signal as shown is barely visible in the motor current temporal evolution in the figure.6.7. Therefore, in order to go deeper in the investigations and check the frequency content of the signals, spectra are studied.

**3.2.2. The signals in the frequency domain**

Figure.6.8 depicts a comparison between two spectra of current time signals shown in the last section for the healthy and defected cases to highlight the impact of the planet tooth defect on the current signal.

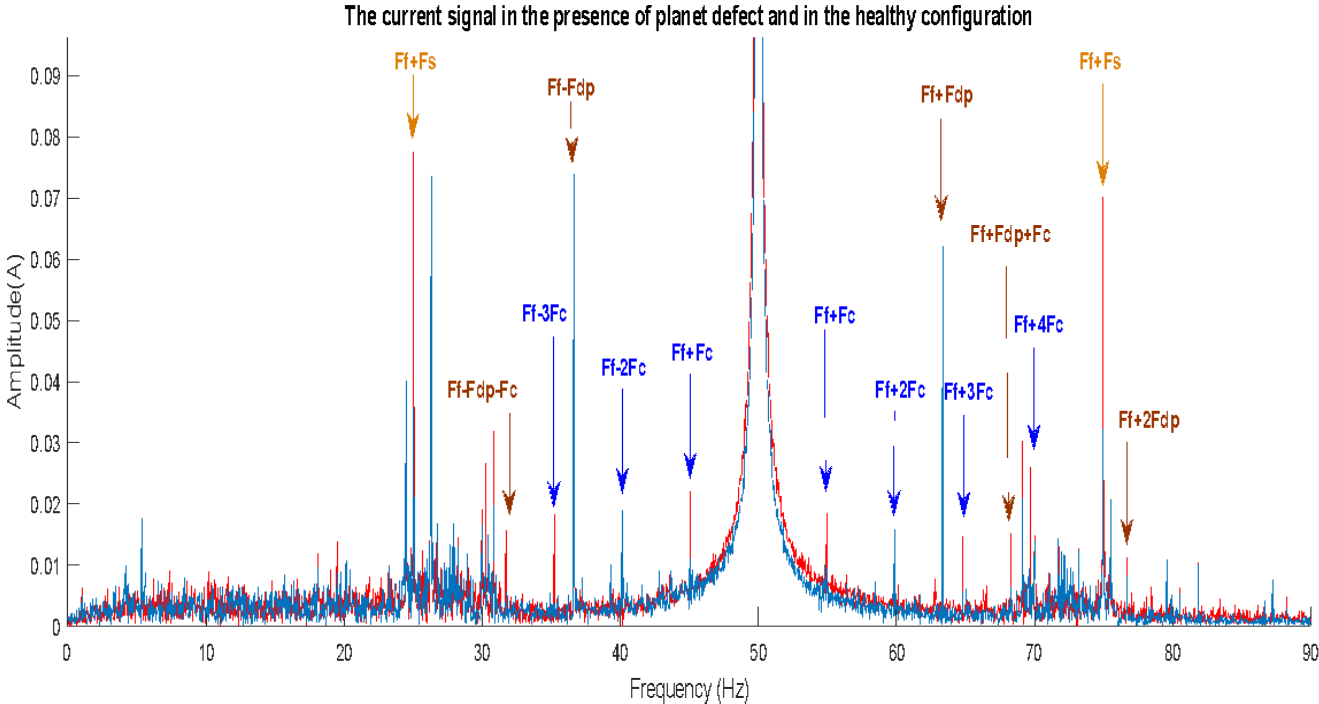


Figure.6.8: The current spectrum in the presence of the planet defect (Red: Defected configuration; Blue: Healthy configuration)

The pitting included on the planet has affected the current signals by increasing the amplitude of some frequency components besides to other frequencies that emerge. The changes in the amplitude of some frequencies such as the components related to sun frequency ( $f_e \pm f_s$ ) after including the pitting is more consistent in MCSA. Furthermore, additional frequencies are noticed, as seen in Table.6.1, due to the presence of tooth defect located at:  $|f_e \pm n f_c \pm p f_{dp}|$ ; where: (  $p=0$  and  $n=1,3,4$  or  $p=1$  and  $n=1$  or;  $n=0$  and  $p=2$ ). The defect of the planet tooth also affects the distance between planet-ring and planet-sun. This influence impacts the movement of the carrier which explains the emergence of the frequencies related to the carrier and its harmonics in the current spectrum (figure.6.8).

Table.6.1: Frequencies (in Hz) for each combination of the expression:

p	n	0	-1	1	-2	2	-3	3	-4	4
0			45.07	54.93	40.14	59.86	35.22	64.78		69.71
-1			31.72							
1				68.28						
2		76.7								

Hence, to justify the results obtained by the current signals, vibrations and acoustic pressure spectra will be presented. Figure.6.9 illustrates the spectra of vibration, recorded by the accelerometer along the Z axis and acoustic pressure signals in both healthy and defected configurations. Vibration spectra are dominated by the gear meshing frequency (320.43Hz) and its harmonics. As clearly noticed in the zoom in the figure 6.10(c), it is noticed the increase of the component related to defect frequency and the amplitude of peak frequency (13.35Hz) related to the frequency defect.

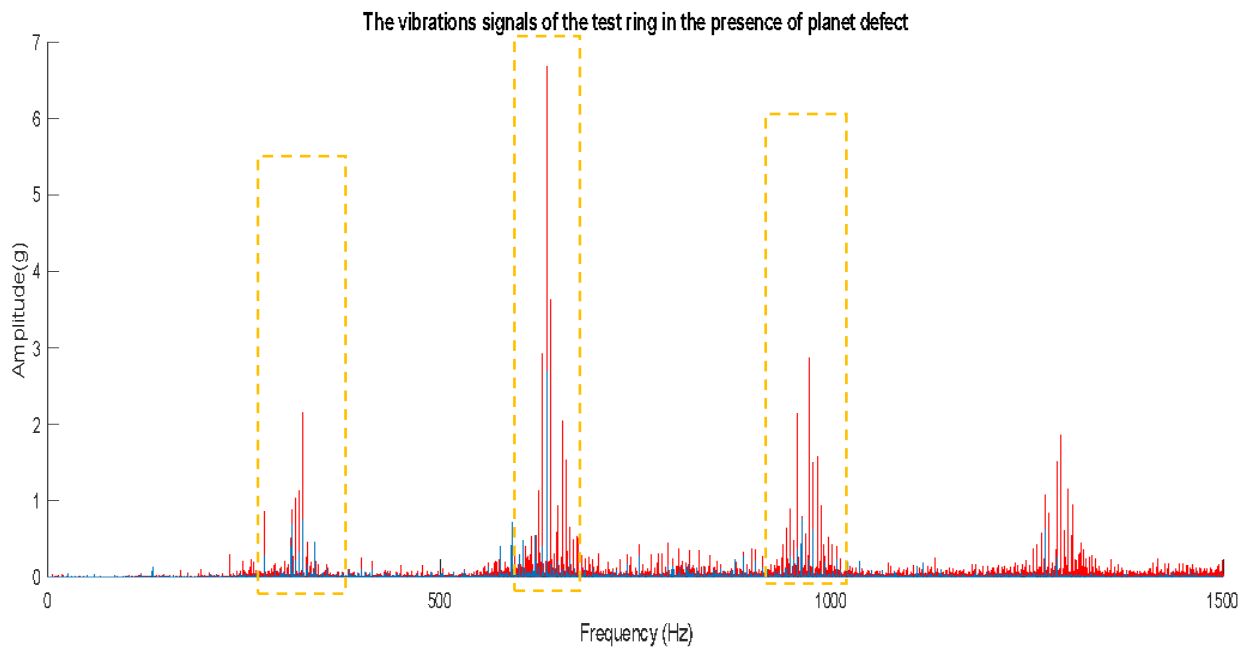


Figure.6.9: Comparing between the vibration's frequency spectrum for healthy configuration and in the presence of planet defect

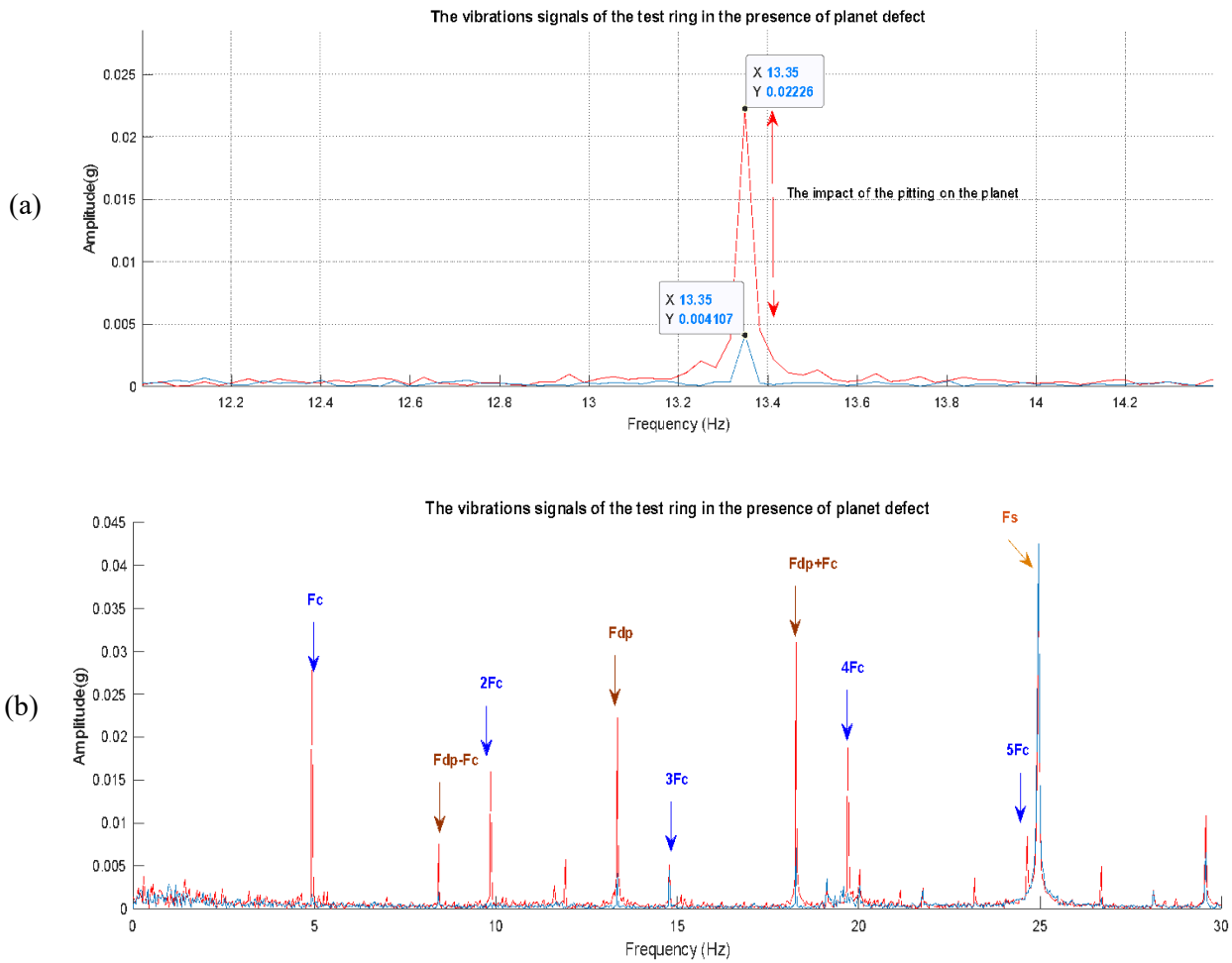


Figure.6.11: The vibrations spectrum in the presence of planet defect in a frequency range [0Hz,30Hz]  
 (a): The vibrations signals in [0,14.5Hz] ;(b): The vibrations signals in [0,30Hz]

In the figure.6.11, the red spectrum corresponds to the frequency spectrum of the vibrations signal in the presence of the tooth crack on the planet. It is noticed that after the implementation of the teeth defect on the planet the frequency  $F_{dp} = 13.48Hz$  appearance with an important amplitude (0.0226g) comparing with the rotational frequency's amplitude (0.045g) (figure.6.11(a)). Also, the appearance of the defect's frequency was accompanied with the carrier frequency and its harmonics.

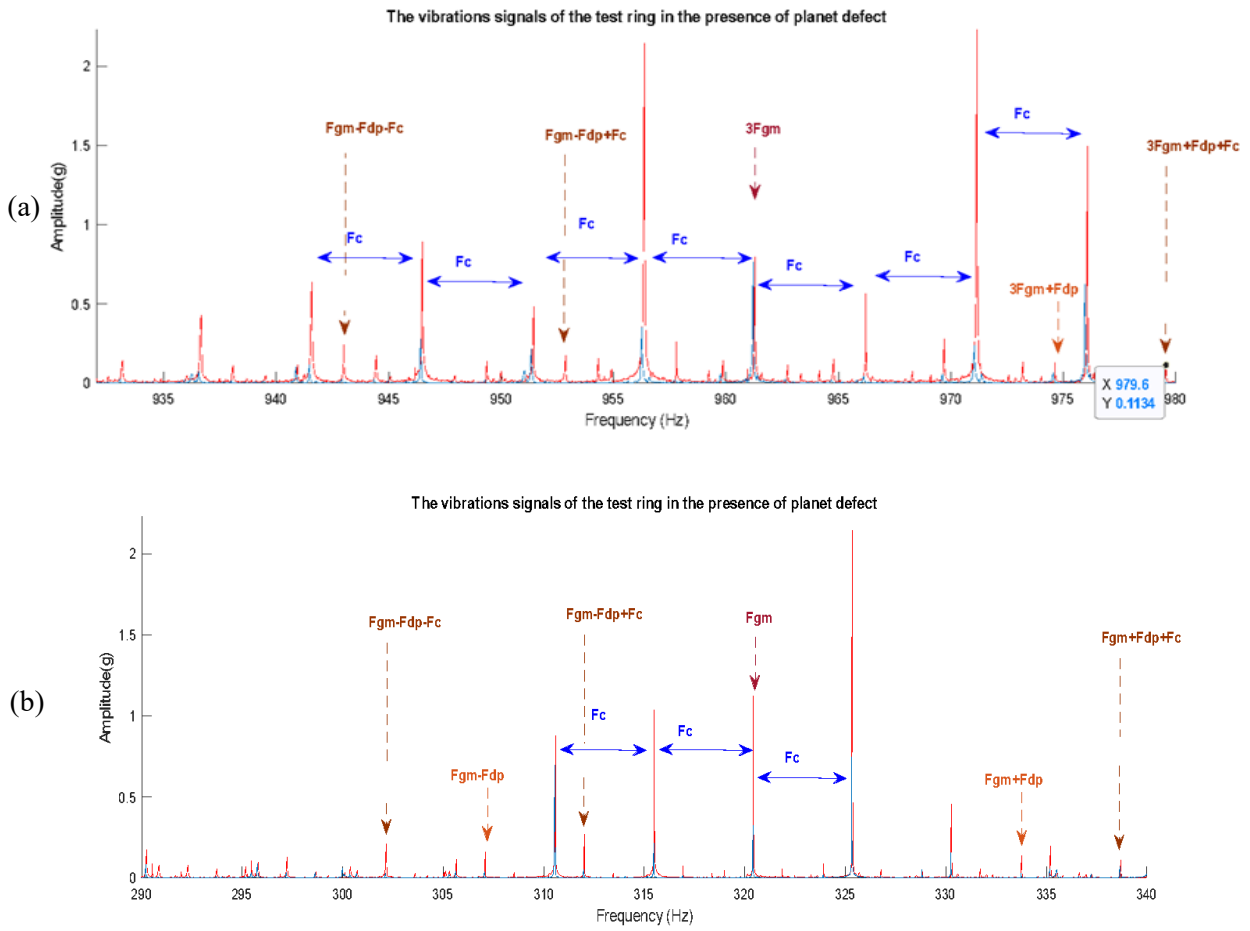


Figure.6.12: The vibrations spectrum in the presence of planet defect in the frequency range [250Hz, 980Hz]

The impact of the tooth defect is also seen in the sidebands around the gear meshing frequency and its harmonics. The gear mesh frequency is modulated by the frequency of the defected planet as seen in the figure.6.12 and the frequency of the carrier multiplied by three that corresponds to number of planets. The amplitude of sidebands of the defect are considered low due to the geometry of the crack implemented.

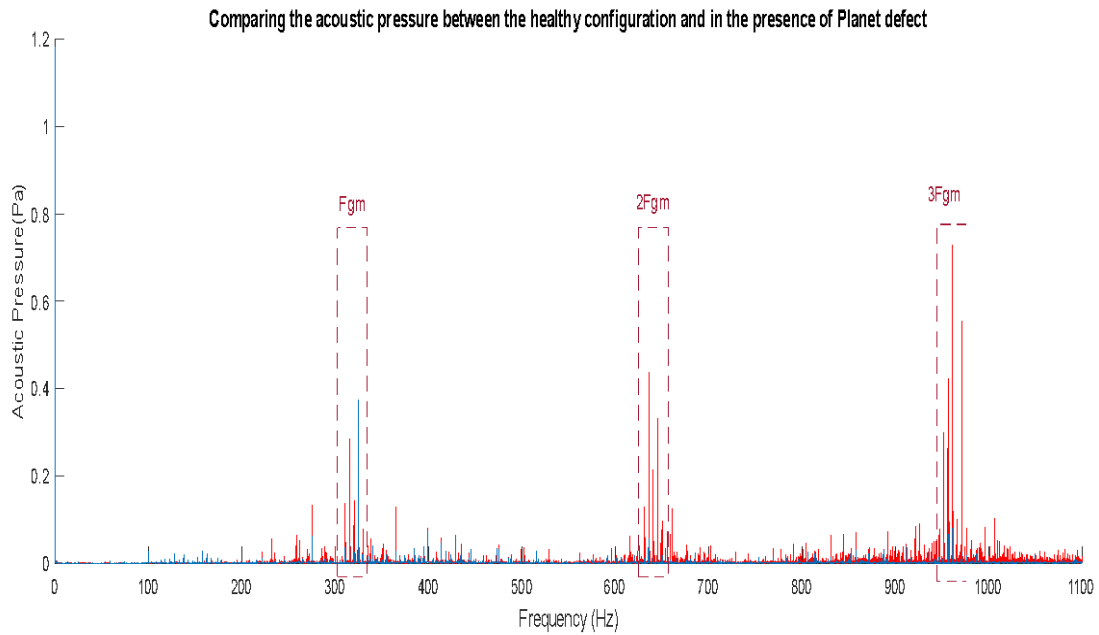


Figure.6.13: the acoustic pressure spectrum (blue: healthy configuration; Red: the presence of planet defect)

Figure.6.14 shows the impact of tooth defect on the acoustic pressure by comparing the signals in the healthy configuration and in the presence of a planet defect. The figure.6.14(a) illustrates the appearance of the pitting frequency ( $F_{dp} = 13.35\text{Hz}$ ). The figure highlights that the impact of the pitting on the vibrations is more significant ( $5 \text{ times } 5 \cdot 10^{-3}$ ), then the impact recorded by the microphones ( $5 \cdot 10^{-3}$ ). This contrast is inversely explained by the distance separating the accelerometer and the microphones to the defected gear. Literally this distance impacts the attenuation of the defect's signature and as consequence the amplitude of its frequency in the frequency spectra.

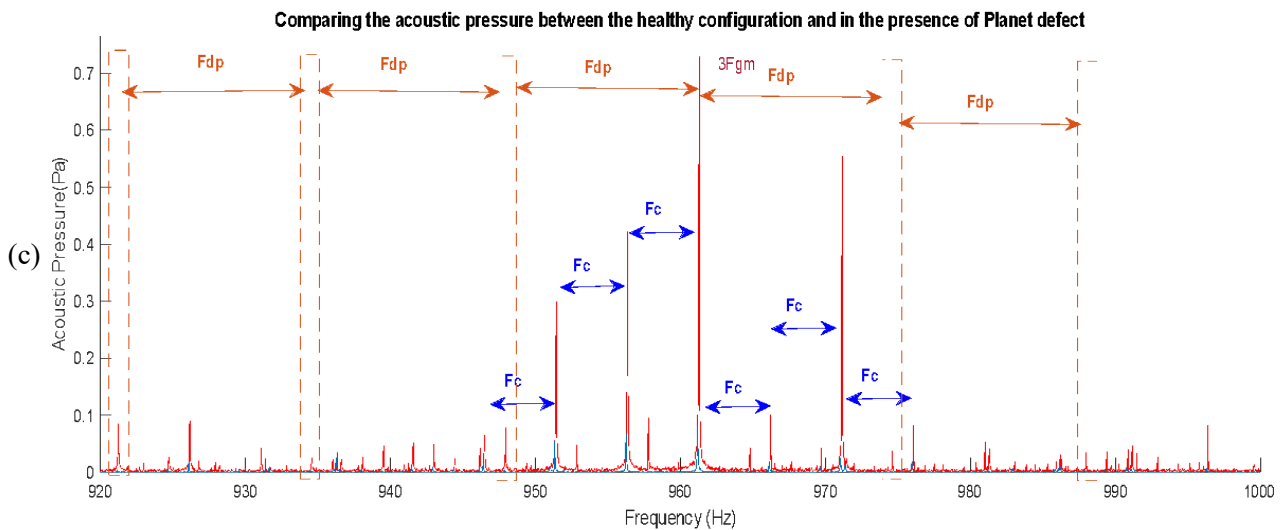
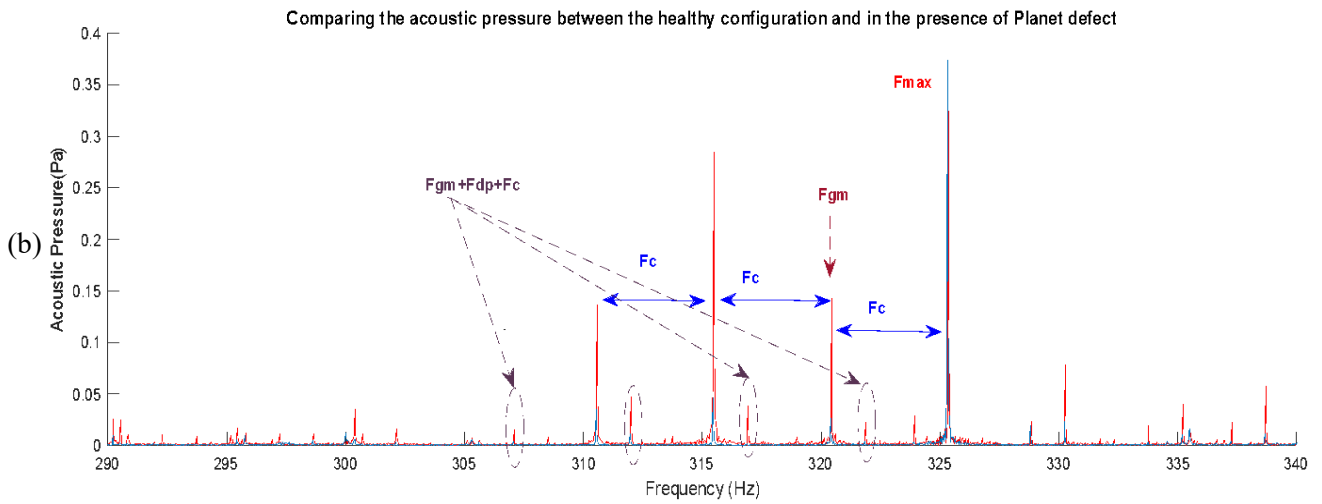
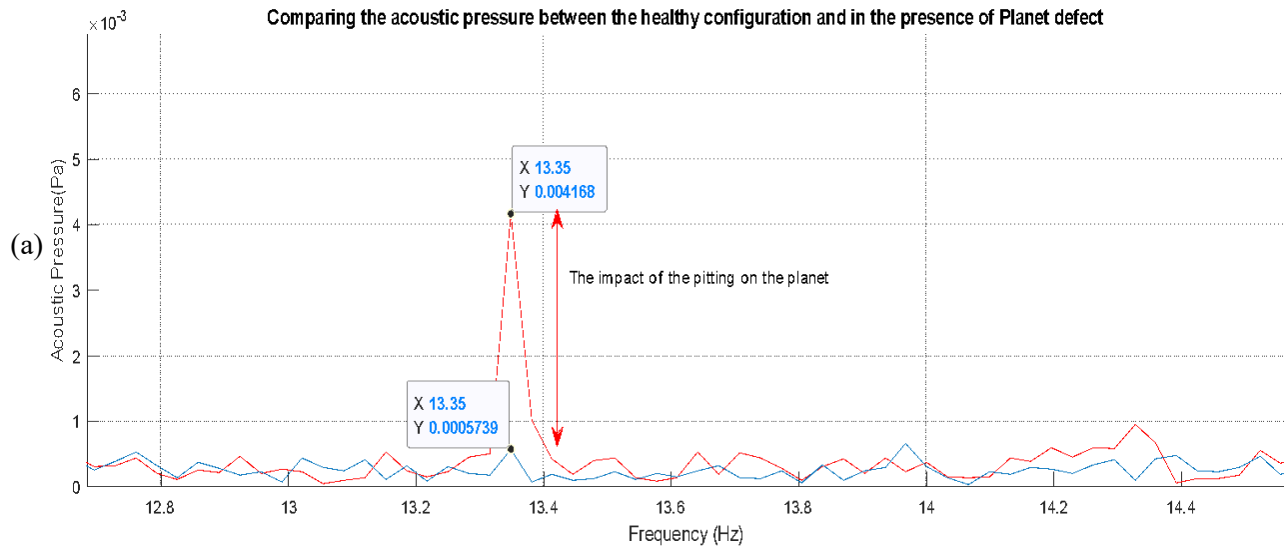


Figure.6.14: The acoustic pressure spectrum in the presence of planet defect. (a): The acoustic pressure in [12Hz, 14.5] ;(b) : The acoustic pressure in[220Hz, 340Hz]; (c) : The acoustic radiation in [920Hz, 1000Hz]

In the figure.6.11(b), also in figure.14(c), the spectrum shows that not only the defect frequency is point up by the planet pitting but also it had highlighted the appearance of the carrier frequency and its harmonics ( $nF_c$ ,  $n=\{1,2,3,\dots\}$ ). On the experimental spectra the appearance of the carrier frequencies and its harmonics are related to the gravity of the carrier as an additional source of vibrations. Indeed, the pitting can increase the relative displacement between the carrier and ring gear, which implies that more force is received by the accelerometer. thus, gravity is more accentuated as a periodic excitation source in the case of defected configuration.

However, in both figures 6.12(a) and .6.14(b) , both the vibrations signals and the acoustic pressure, the impact of the planet pitting is enhanced by the appearance of other sidebands given by  $|F_{mesh} \pm nF_c \pm pF_{dp}|$ . Finally ,in the same spectra comparing between the healthy configuration and the current spectrum in the presence of the planet pitting, we notice the increase of the amplitude related to the carrier frequency  $mF_{mesh} \pm nF_c$  ( i.e.: 921Hz, 931Hz..).

### 3.2.3. Combined defects in the test gearbox

In this section, two types of defects are introduced simultaneously (crack on one tooth of the sun gear and pitting on one tooth of the planets). The figure.6.17 presents the current spectrum in different configurations of the gears. The current signals illustrated in the figure.6.17 investigate the impact of the type, placement, and dimensions of the defect on the motor current.

In Figure.6.17, four configurations are presented: (1) The reference plots which corresponds to healthy set of gears, (2) Spectra in the presence of defected planet, (3) Spectra in the presence of sun crack and finally (4) Current frequency spectrum with both defects. In the figure.6.17 the current spectrum in green is recorded in the presence of the sun pitting considered a local defect. When the local fault meshes with one of the planet gears, the vibration signal is modulated by an impulse signal. Therefore, When the local fault exits the meshing area, the vibration signal returns to its normal condition. However, the impact of the vibrations accrue from the sun pitting is observed in the current spectrum by the related characteristic frequency  $F_f + F_{ds}$  (110Hz). When the sun has a local defect, it meshes with the three planets therefore its appearance in the current spectrum is enhanced each time of the rotating sun frequency relative to the carrier  $F_f + F_{sc} - F_{ds}$  (expl:80Hz)

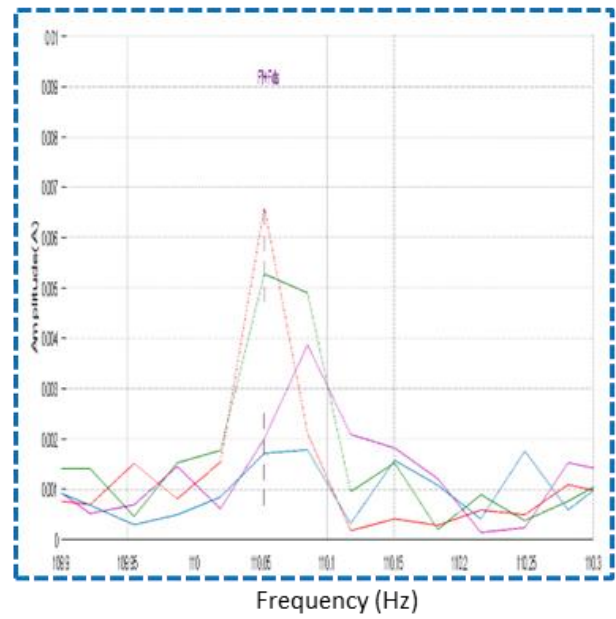
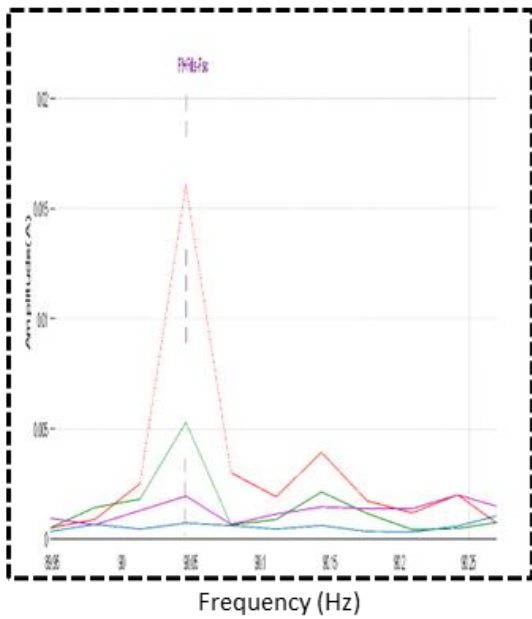
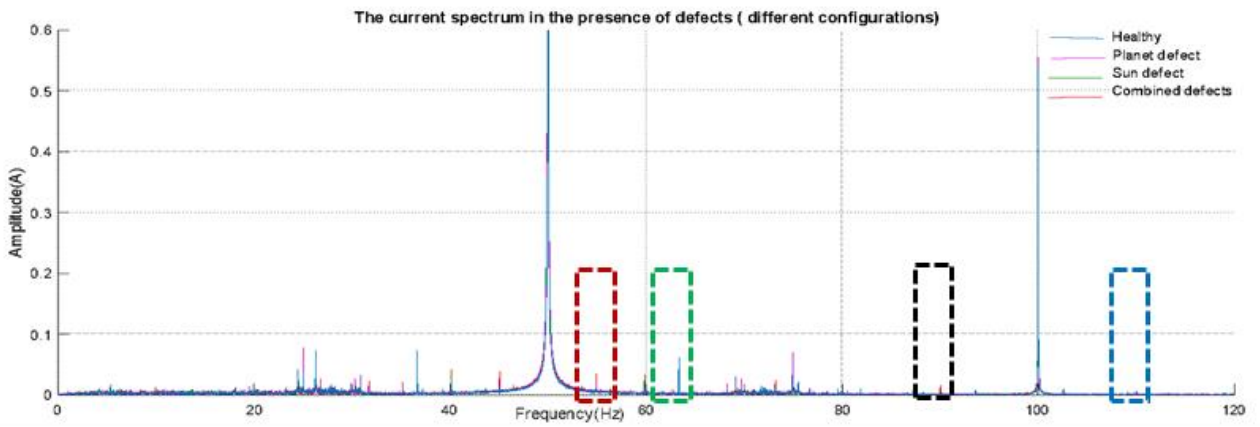
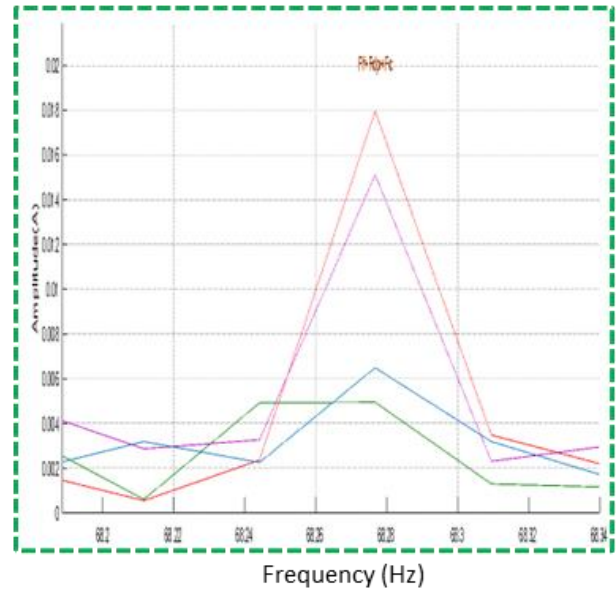
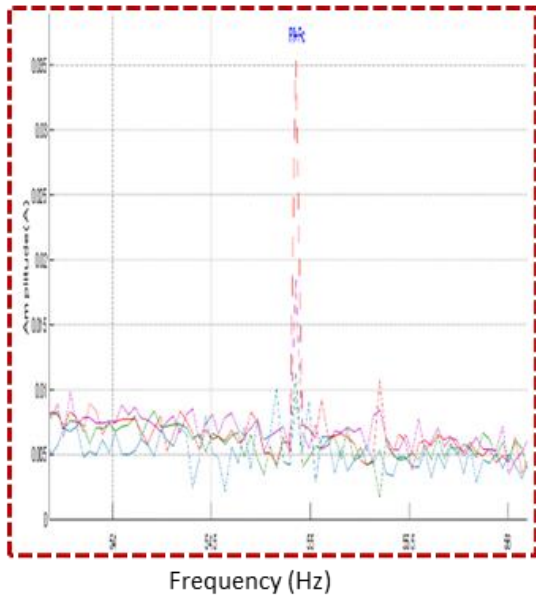


Figure.6.17: The current spectrum in the presence of combined defect

In the same figure, the spectrum presents the impact of the co-existing of the sun pitting and the planet defect on the current signal. Both figures.6.17 demonstrates that the presence at both defects enhance the amplitude of the related frequencies of each defect demonstrated above. We notice the increase of the amplitude of the peak related to the carrier frequency  $F_f + F_c$ . This frequency can be explained by the contact between both defects which can generate an additional source of vibration and impact the spectra consequently. Besides to the sensitivity of the MCSA to the local of the tooth defect, Table.6.2 presents the impact of the size and location of the defect on the increase of the corresponding frequency.

Table.6.2: The impact of the size and the location of defect of the increase of the current amplitude

Defect location	Defect depth (mm)	The percentage of the increase of the amplitude of the current signal in the corresponding frequency			
		$F_f + F_c$	$F_f + F_c + F_{dp}$	$F_f + F_{ds}$	$F_f + F_{sc} + F_{ds}$
The sun	5			90%	66%
The planet	2	56%	53%		

The coexisting of the teeth defect introduced on the sun and the planet crack enhances the current signal response. According to the Table.6.2, the current signal is sensitive enough to the localization of the source’s perturbation. In the same table we notice that the defect’s size impacts the amplitude of the related peaks.

#### 4. The wear degradation phenomena impact of the phase current signal

The work will be divided in two parts. In the first part degradation observation of non-treated gears that was runed under important load that generate wear loss of the planet and the sun gears was done. The vibration and current spectra are analysed for this case. The second part is dedicated to deep tracking of wear development for nine successive hours running time using current and vibrations measurements. Finally, the main conclusions for this degradation study will be presented.

##### 4.1.The degradation states

Generally, there are two types of wear defect: uniform and non-uniform. Uniform wear refers to the ideal case where all teeth are worn identically. This kind of gear wear results in an increase in the average working surface deviation and will manifest in increases in the amplitudes of tooth meshing harmonics. For the Non-uniform wear, the gears teeth are worn differently. In opposite to uniform wear, it will affect both the average working surface deviation and tooth space width. Depending on the conditions, the tooth-to-tooth differences might either increase or decrease [78].

In this part, the back -to back planetary gearbox is runed for forty hours under different speed conditions and loading from 300N.m to 900N.m. For these operations conditions and having non-treated tooth

flanks, a wear is generated as shown in figure6.18. Therefore, an investigation was based on recorded signal later to track this phenomenon impact.

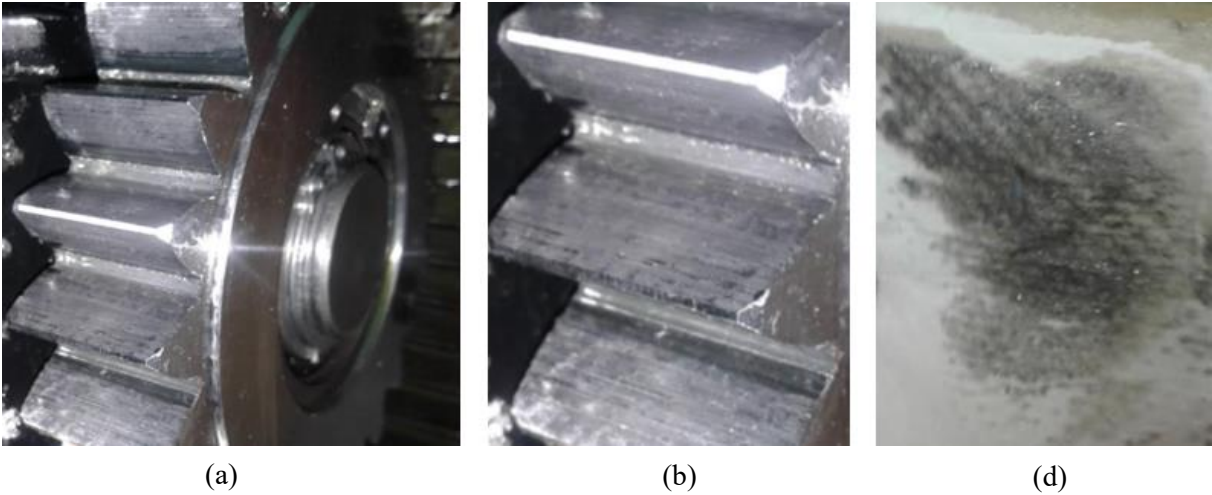


Figure.6.18: The reference set and after degradation set.(a):The sun ; (b) : zoom of the degradation impact ; (c) the wear in the lubricant

The work presented in this part, is done exclusively on the experimental testbench described in **chapter 2**. In this study, we used new manufactured gears without any surface treatment. These gears were ran for **forty hours** to improve the surface roughness of the planets. This operation had generated micro Pitting appearance as seen in figure6.18. The effect of this degradation on the current signal is investigated. Within the same context, the degradation study is focused also on the wear developed on teeth sun.

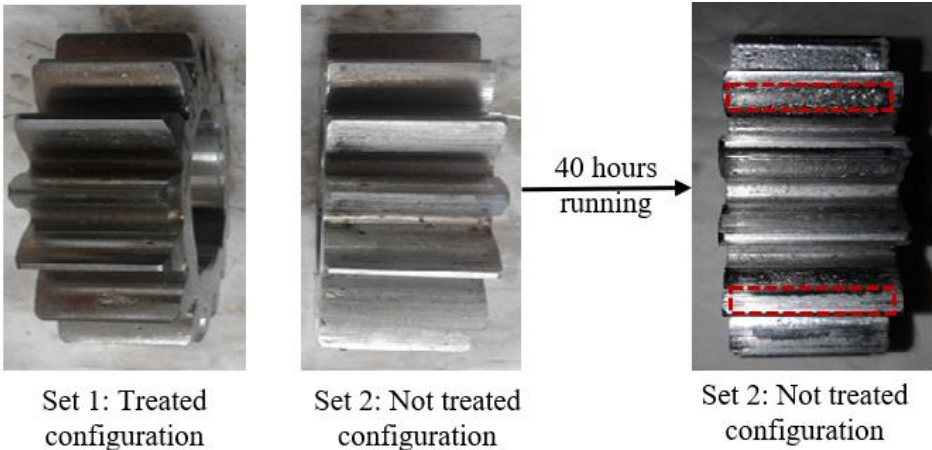


Figure.6.19: The reference set and the degradation set.

**4.2.The impact of the wear degradation on the current spectrum**

The figure.6.20 presents the spectrum of the current measured for two configurations: the first spectrum in blue defines the current frequency components at the begging the experiments. The second spectrum in red is related to the current signal after **40hours** of running.

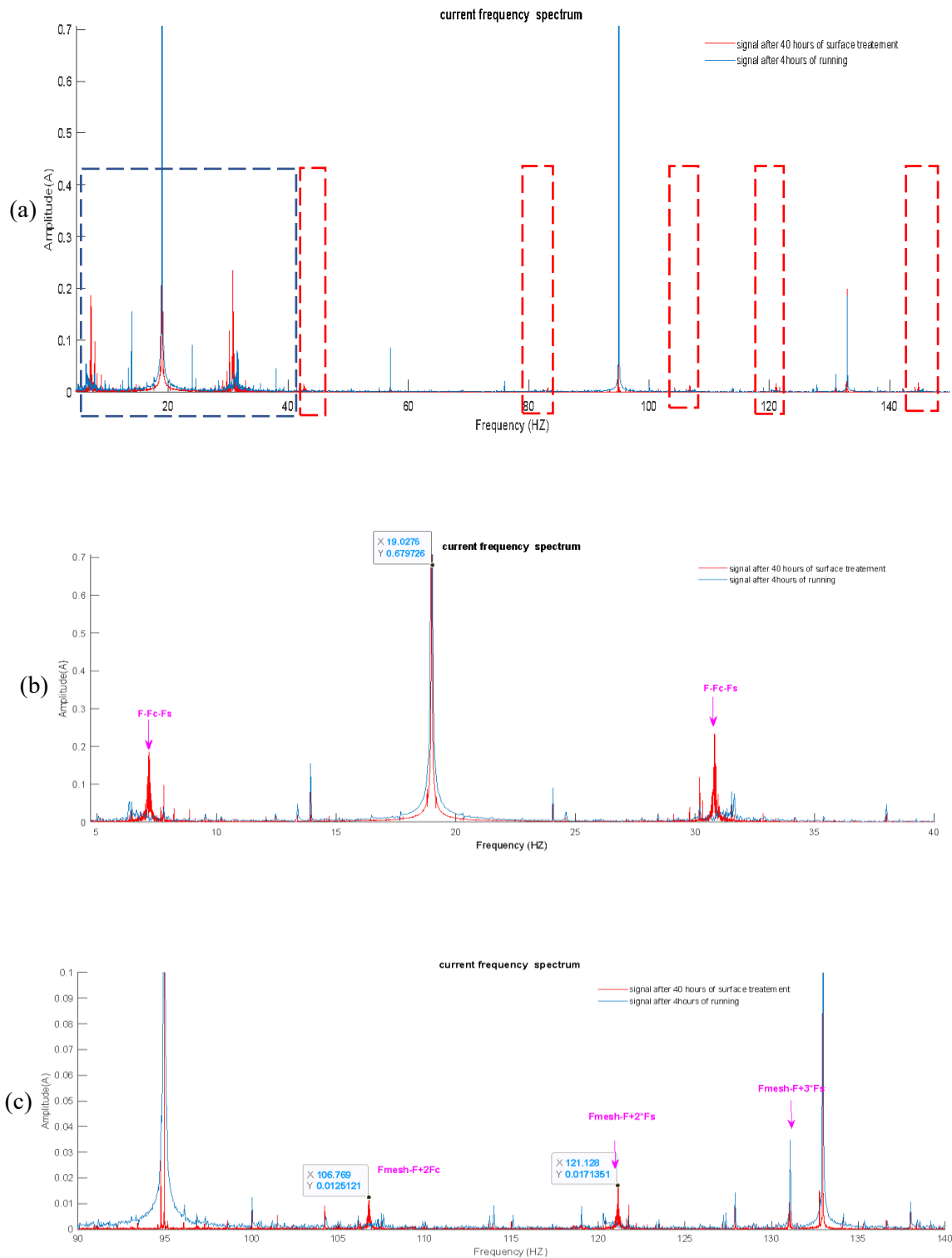


Figure.6.20: The Current signal comparing between the current after 40hours of running and 4 hours  
 (a): [0Hz; 150Hz]; (b): [4Hz; 40Hz] ; (c) [90Hz; 140Hz]

Totally foreseen, the current frequency spectrum illustrates the appearance of additional peaks and the increase of the current amplitude in others characteristic frequencies.

In forty hours of surface aggression, the impact on the current signals is registered by the related sun frequency  $f_s$  and the carrier frequency components. In the current signal, as explained in chapter 3, a frequency related to the motor frequency should be observed. The gear’s wear loss is considered as a major failure mode that generate a decrease of the contact surface between teeth. The direct results of gear wear include dynamic transmission error, power transmission losses, and high vibration and noise levels [78]. Severe wear can also cause uneven load distributions. This load distribution generates imperfections and perturbation in the current signals which explains the results above. These imperfections in sun gear impact the sun-planet contact and by then the carrier “movement. The degradation of the wear surface is considered as a distributed damage to the gear teeth. For distributed damage case, the characteristic frequency of a faulty gear in planetary gearboxes is defined as the relative rotating frequency of the faulty gear with respect to the sun carrier, because the distributed gear damage modulates gear meshing vibration at a period equal to the damaged gear rotating cycle relative to the planer carrier. This impact will be periodically generated. this impact is seen in the frequency spectrum by, the app<sup>2</sup>earance of the  $F_{mesh} - F + 2F_s$ ,  $F_{mesh} - F + 2F_c$ ,  $F + F_s - F_c$  and  $F + F_s - F_c$  seen in the figure 6.20. where  $F_s - F_c$  represents the sun carrier frequency.

**4.3.Kurtosis**

In order to study continuously the evolution impact of the wear aggression on current, the kurtosis of the current time signal was used. The Kurtosis represents the flattening rates of the distribution of a signal Kurtosis is a measure of peaks, and it is a good indicator of signal impulsiveness in the context of fault detection for rotating components. The figure.6.21 illustrates the evolution of the kurtosis of the current signal per time. The kurtosis scale presents below the corresponding parameter of each current signal.

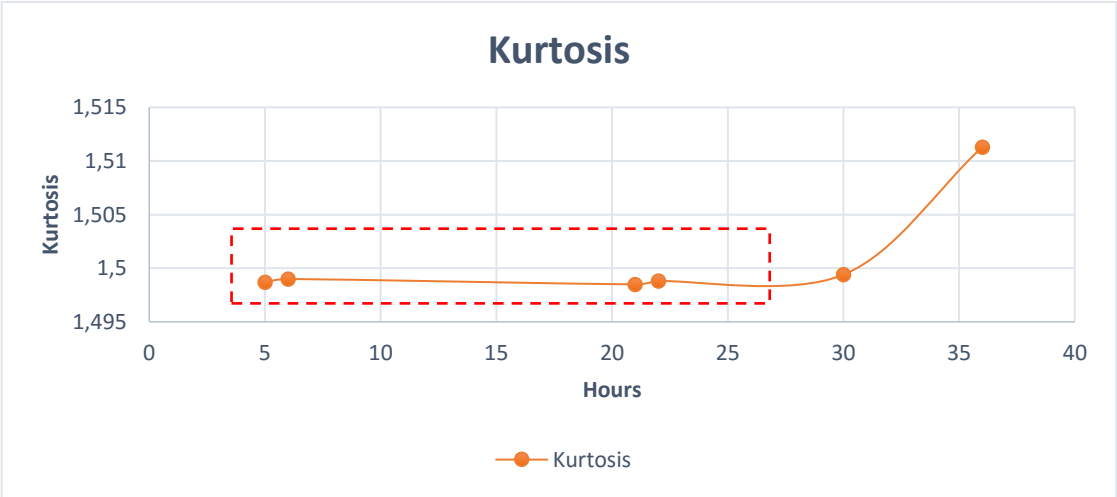


Figure.6.21. The Kurtosis evolution for the 40 hours test

In the figure.6.21, the kurtosis increases which is totally explained by the appearance of micro-pitting due the wear development on the gears. The interpretation of these parameters has generated the doubt about how sensitive of the current signal to the wear detection in the gear system is.

#### 4.4.The impact of sun teeth wears on current signals

In this part of study, we changed the sun in the reaction gearbox by a new sun as seen in the figure.6.22. The figure6.22(a) shows the tested sun in the healthy configuration at the beginning of the test. Meanwhile figure6.22(b) zoomed the scratches caused by the continuous the running of the system. [79]. In this part we track the impact of the sun surface wear evolution on the current signal and the vibrations level. The test will be performed for **9 hours**. Signals are recorded simultaneously along the tests with controlling each hour the mass evolution of the sun and the temperature of the oil used as lubricant. Instruments will be mounted as mentioned in chapter3.

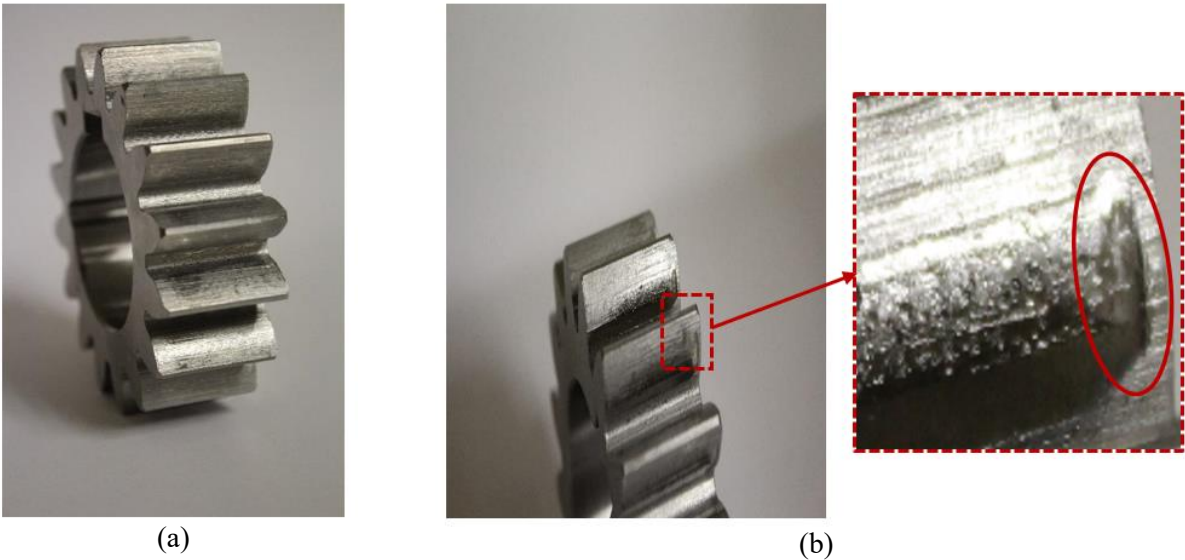


Figure.6.22.: The sun surface during the test (a): The sun in the healthy configuration; (b): the sun after the intensive test

Table.6.3 presents the follow up of the sun mass. The figure.6.23 shows the remarkable amount of material lost during the first three hours. This impact is related somehow to the increase of the shaft speed from 280 rpm to 570 rpm and varying load from 100N.m to 600N.m.

Table.6.3. The hourly evolution of the sun's mass

Hours	Mass (g)	Remarks
0	400,91	Initial state before test
1	400,36	
2	399,76	Increasing the speed (20Hz)
3	399,73	
4	399,73	
5	399,68	Increasing the load (Mass:60Kg)
6	399,68	
7	399,65	
8	399,64	
9	399,61	

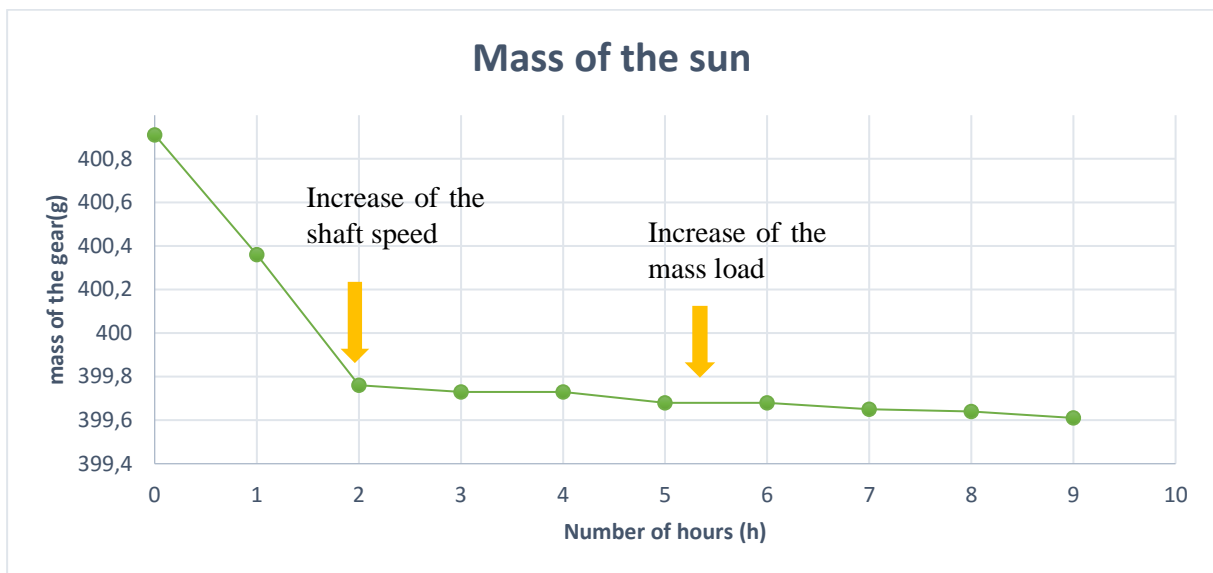


Figure.6.23: Sun mass evolution during the test

## 5. The vibrations signals in the presence of the wear degradation

As mentioned by Chongqing Hu et al. in [80], the effects of gear wear on vibration signals can be explained in terms of its influence on Transmission Error (TE). Considering that the gear supporting system and the gear operating conditions are invariant, gear wear will be the main source of changes in transmission error and vibration signals.

The vibration signal along X+ is measured, as shown in the chapter.3. The first figure.6.24 is the envelop temporal s of both signals after one our running and after 9 hours. The red signature shows the

appearance of an additional component to vibrations signal in nine hours comparing to the signal recorded after one hour of treatment. Below, the temporal results shows that nine-hour surface treatment can Impact the vibrations signals. The figure 6.24 presented the envelop signal of the acceleration (+X). This signal was recorded by the accelerometer mounted on the reaction gearbox. We illustrate below an overview of the difference between a temporal evolution of the vibration after one hour of loading system and after nine hours. It can be observed from figure 6.24 that the increase of load leads to an increase of vibration level with the appearance of periodic components.

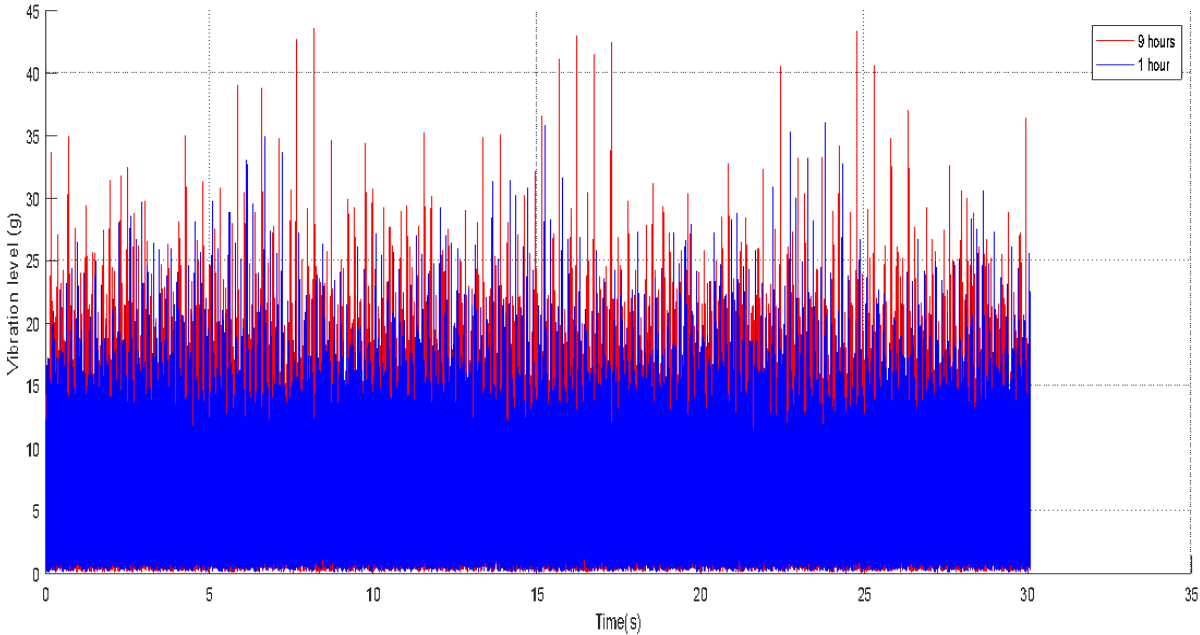


Figure.6.24: Comparison between vibration signals at the first hour and the ninth hour

- **Frequency spectrum**

Figure 6.24 presents the frequency spectrum of the vibration’s signals for the time periods (1 and 9 hours). Figure 6.25 show clearly the increase in the amplitude of the gear meshing frequency that goes from 1.4g to 2g due the surface damage after 9 hours. This result is expected since distributed defect generates higher amplitudes of mesh frequency components. The degradation in the sun is seen by the appearance of the sub frequencies  $f_s$  (9.47Hz) and  $f_s + f_c$  (11.76Hz) in the vibration’s frequency spectrum.

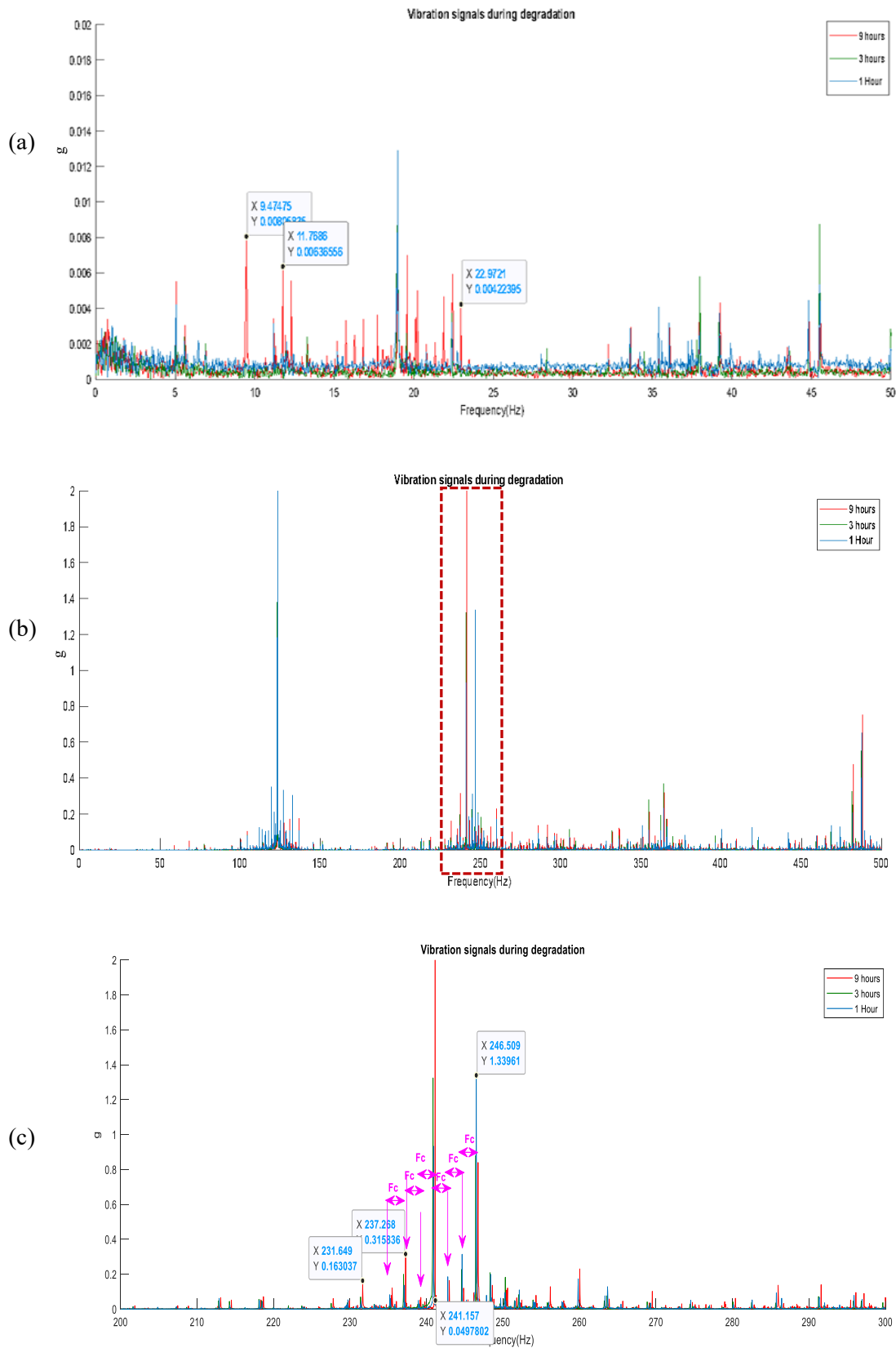


Figure.6.25: The vibrations frequency spectrum; (a): Zoom of the frequency spectrum of the vibrations signal in [0Hz,50Hz] ; (b) The frequency spectrum of the vibrations signal in [0Hz,500Hz]; (b) The frequency spectrum of the vibrations signal in [200Hz,300Hz]

Uniform wear tends to give a double-scalloped wear pattern on each tooth, because there is a pure rolling action for contact at the pitch circles and sliding for contact on either side. Hence, the first important highlight of the wear degradation will be mainly the increase in the second harmonic of the tooth mesh frequency as seen in the figure 6.25. This increase of amplitude is explained by the fact that the effect of degradation must be greater than the tooth deflection to be more noticeable [81]. As wear develops, the profile will deteriorate more generally, and all harmonics of tooth mesh frequency will increase.

**5.1. The current signals**

Figure6.26 shows the difference between the envelope current signal at the initial test and after 10 hours. There is no clear impact on the current after the wear loss of the sun. Therefore, the current time signal is not a good indicator to identify the degradation process.

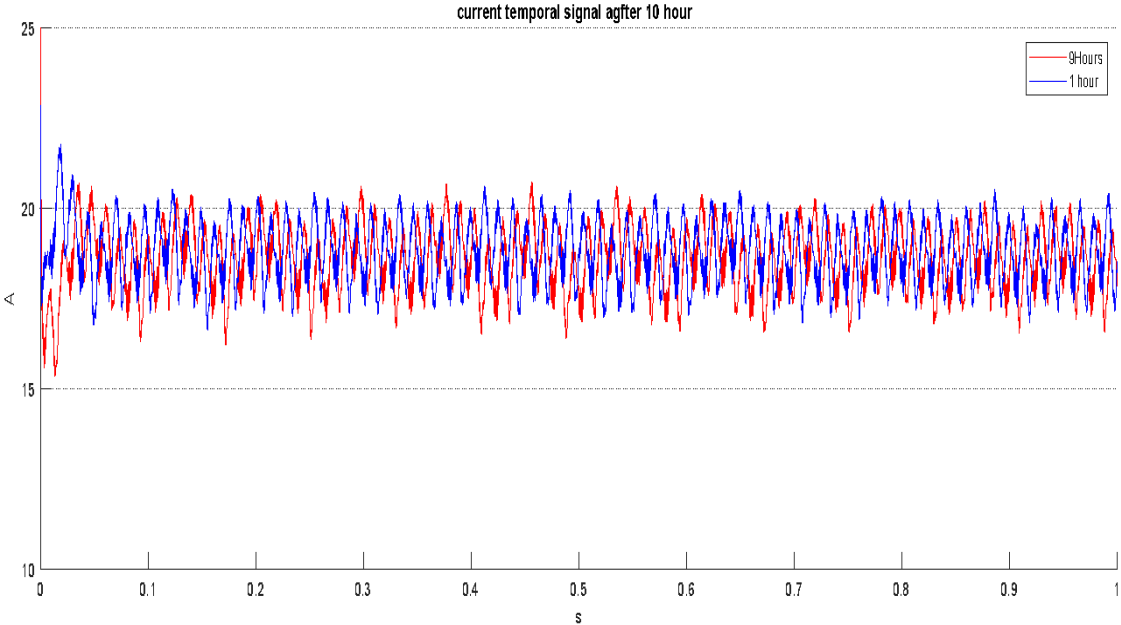


Figure.6.26: The vibrations frequency spectrum

- **Frequency spectrum**

Figure.6.27 illustrate a comparison between the current spectrum in correlation with the surface major degradation. After 9 running hours, besides to an insignificant amplitude increase in the sidebands of the motor frequency, we cannot notice any substantial impact on the last signal that can be related to the wear development. This fact can be related to the minimal mass degradation generated in the sun and to the attenuation of the wear loss impact before reaching the electrical clamp. The mass degradation of the sun would create a fluctuation in the sun shaft torque. and as developed in the chapter.3 it will generate a frequency modulation and amplitude modulation in the motor current.

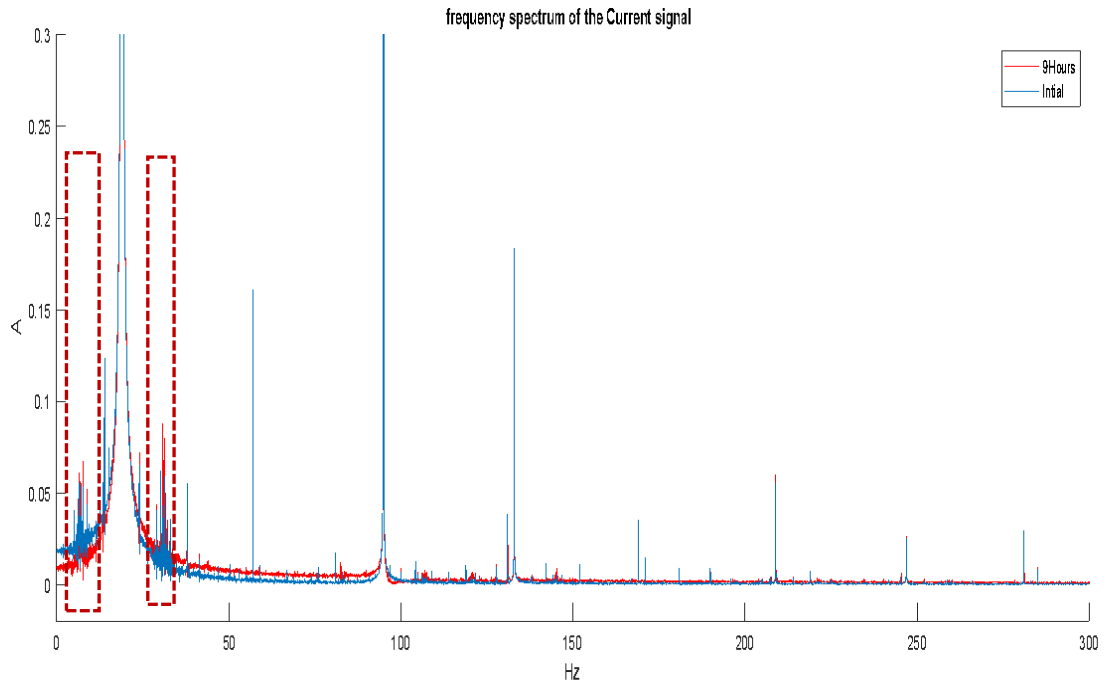


Figure.6.27: Comparison between the current signal initial test and after 3 hours of running system.

## Conclusion

In this chapter, the Multiphysics study done throughout the numerical model has been used in the gears monitoring. The current signal has highlighted the impact of different type of gears defect on the motor current signal. By the MCSA, it has been shown that investigating the motor's state can be significant to report the dynamic status and the state of planetary gears. However, this condition monitoring study was followed by two relevant proofs. First, besides to simulations experimental tests measurements were presented. Different gears defects were implemented on the double stage planetary gearbox test bench. These operating tests were meant to highlight the sensitivity of the electric clamp to gears defects.

On the other side, a multiphysics comparison has taken place. The MCSA were compared to both vibrations' signals and acoustic radiations. The crack implemented on the tooth of the gear was seen in all the signals by its key frequency. Also, the motor current signal has shown a sensitivity to the combined defects. In this case, each defect appears in the frequency when meshing with a corresponding healthy tooth. The coincidence of two defected teeth impacting the meshing phenomena and generates the appearance of a new defect's frequency. Finally, this research work was concluded with the efficiency of the MCSA to geometric defect on gears.

## General Conclusion

Finally, in this part of thesis general conclusion will be presented. In this first part of this Thesis memory, the main objective was studying the dynamic behaviour of the planetary gearbox by analyzing the electrical response of the asynchronous motor driven this bench in different operating conditions. In the industrial domains, it is important to have the access to a tool that describes the behaviour of the gears system taking into consideration its complexity. Within this context, the main objective of this research was to study the sensitivity of the current signal to the electromechanical interaction. This objective was established in both experimental and numerical simulations.

However, the work in this thesis was divided into two main parts. A deep numerical modelling of an electromechanical system form by an asynchronous machine and gear system. For the trained system, we used park transformation to model the asynchronous motor which is an analytical method that aims to transform the three phased motor and a bi-phased system. This method facilitates tracking the stator current and to easily seen any external perturbation.

For the mechanical part, two different systems were used. First, the numerical development was done using a simple spur gears system with four degrees of freedom per gear. The aim beyond this model was mainly to approve the electrical model of the driven machine and to validate that the model is sensitive to any type of load perturbation. Later gears defect in this system were implemented to highlight the sensitivity of the current signal to gears defects.

Later, the electrical model was connected to a torsional model of a back-to-back planetary gearbox system. The system was composed of two identical planetary gearboxes. In this system, different operating conditions were simulated, for healthy configurations: gears were considered healthy, and the system were considered in ideal cases. Later different defects have been introduced. Using a torsional mechanical and a bi-phased motor of an asynchronous machine, a multidomain model has been elaborated. This electromechanical system has approved that the current signal is a performing non-destructive tooling to detect teeth defects.

In order to approve that current is an efficient tool to detect mechanical anomalies, an experimental study has taken place. The experiments have aimed to justify all the numerical simulations founding. Also, for the experimental measurement two different systems were exposed to study. The first part illustrates a low speed testbench formed of spur gears connected and a geared motor. In this part of work, we studied the impact of gear meshing on the current signal recorded using electrical clampers. These first measurements were taken in order to justify and validate the choice of the electrical clamp. Second, the main experimental investigations were taken for a back-to-back planetary gearbox system driven by an asynchronous motor.

In this part of study, different signals were recorded. the motor current signature, were taken simultaneously with vibrations signal and acoustic pressure. Recording different parameters at the same time, was used to validate each technical and highlights its sensitivity to electromechanical interaction. The experimental measurements were taken for healthy system and in the presence of teeth defects. It was seen that in the case of gears crack, defect key frequency appears in the vibration signals and acoustic pressure frequency. Meanwhile, for the motor current signature analysis, the key frequency of the defect was highlighted as a modulated frequency by the supply frequency.

The last part of this thesis has drilled more with system monitoring to study the impact of wear degradation the current signals. In this part, a comparative study has taken place to show the limitation of this method and the role of different techniques in detecting defects in rotating systems. The current signal has shown an incapability to track the wear degradation. This ascertainment can be explained by the attenuation of the impact's signal propagation from the mechanical system to the motor.

### **The future work:**

For the future work, an analysis of the dynamic behaviour of the planetary gear transmission should be achieved in non-stationary conditions. For the numerical studies, we can enhance our research by a numerical model with more degrees of freedom. The numerical model elaborated, can be used to study the impact of the wear degradation on the motor current signal. On the other hand, the experimental tests taken can be followed by a non-stationary condition. These different conditions can be involved in studying the impact of defect on the current signal and acoustic pressure.

## Scientific Publications

This work has contributed to one research article published and five international conferences papers :

### Journal papers:

Boudhraa, S., del Rincon, A. F., Chaari, F., Haddar, M., & Viadero, F. (2021). Tooth defect detection in planetary gears by the current signature analysis: numerical modelling and experimental measurements. *Comptes Rendus. Mécanique*, 349(2), 275-298.

### International conferences papers:

#### Cmmno18:

Boudhraa, S., del Rincón, A. F., Chaari, F., Haddar, M., & Rueda, F. V. (2018, June). Default Detection in a Back-to-Back Planetary Gearbox Through Current and Vibration Signals. In *International Conference on Condition Monitoring of Machinery in Non-Stationary Operation* (pp. 189-197). Springer, Cham.

#### ICAV20:

S. Boudhraa, A. Hammami, A. F. D. Rinacon, F. Chaari, F. V. Rueda, M. Haddar, (March 2021). The impact of gear tooth defect on the current signal of an asynchronous motor. In the international conference on Acoustics and Vibrations.

#### A3M18:

Impact of torsional vibrations of a planetary gearbox on the current of an asynchronous machine

#### Indus 4.0:

Safa Boudhraa Alfonso Fernandez del Rincon Mohamed Amine Ben Souf Fakhher Chaari Mohamed Haddar Fernando Viadero. (May 2019). Investigating the Electro-mechanical Interaction Between Helicoidal Gears and an Asynchronous Geared Motor. in *Smart Monitoring of Rotating Machinery for Industry 4.0*



## References

- [1]: Feki, N. (2012). Modélisation électro-mécanique de transmissions par engrenages: Applications à la détection et au suivi des avaries (Doctoral dissertation, Lyon, INSA).
- [2]: Kamal, B. (2015). Conception de la commande d'une machine asynchrone. Departement de l'Electrotechnique, Université des Sciences et de la Technologie d'Oran. Master: 139.
- [3]: Zhu, G., McDonald, B. A., & Wang, K. (2010). Modeling and analysis of coupled inductors in power converters. *IEEE transactions on Power Electronics*, 26(5), 1355-1363.
- [4]: J. Perho, "Reluctance network for analysing induction machines," Ph.D. dissertation, Helsinki Univ. Technology, Helsinki, Finland, 2002
- [5]: Fourati, A., Bourdon, A., Feki, N., Rémond, D., Chaari, F., & Haddar, M. (2017). Angular-based modeling of induction motors for monitoring. *Journal of Sound and Vibration*, 395, 371-392.
- [6]: Feki, N. (2012). Modélisation électro-mécanique de transmissions par engrenages: Applications à la détection et au suivi des avaries (Doctoral dissertation, Lyon, INSA).
- [7]: Özgüven, H. N., & Houser, D. R. (1988). Mathematical models used in gear dynamics—a review. *Journal of sound and vibration*, 121(3), 383-411.
- [8]: W. A. TUPLIN 1958 Proceedings of the International Conference on Gearing, Institution of Mechanical Engineers, 24-30. Dynamic load on gear teeth
- [9]: W. A. TUPLIN 1950 Proceedings of the Institution of Mechanical Engineers 16, 162-167. Gear tooth stresses at high speed
- [10]: Korka, Z. (2007). An overview of mathematical models used in gear dynamics. *Romanian Journal of Acoustics and Vibration*, 4(1), 43-50.
- [11]: Fakher CHAARI, Mohamed Slim ABBES, Fernando Viadero RUEDA, Alfonso Fernandez del RINCON, Mohamed HADDAR, Analysis of planetary gear transmission in non-stationary operations.
- [12]: Dhatt, G., & Touzot, G. (1981). Une présentation de la méthode des éléments finis. Presses Université Laval.
- [13]: Al-Shyyab, A., & Kahraman, A. (2007). A non-linear dynamic model for planetary gear sets. *Proceedings of the Institution of Mechanical Engineers, Part K: Journal of Multi-body Dynamics*, 221(4), 567-576.
- [14]: C. Yuksel, A. Kahraman, Dynamic tooth loads of planetary gears sets having tooth profile wear, *Mechanisms and Machine Theory* 39(2004) 695–715.

- [15]: Modelling of local damages in spur gears and effects on dynamics response in presence of varying load conditions, F. Chaari\*, R. Zimroz\*\*, W. Bartelmus\*\*, T. Fakhfakh\*, M. Haddar\*
- [16]: Davis, J. R. (Ed.). (2005). Gear materials, properties, and manufacture. ASM International.
- [17]: Boiadjiev, I., Witzig, J., Tobie, T., & Stahl, K. (2014, August). Tooth flank fracture—basic principles and calculation model for a sub-surface-initiated fatigue failure mode of case-hardened gears. In International gear conference (pp. 670-80).
- [18]: A New Acoustic Emission Sensor Based Gear Fault Detection Approach Yongzhi Qu<sup>1</sup>, Eric Bechhoefer<sup>2</sup>, David He<sup>1</sup>, and Junda Zhu<sup>1</sup> <sup>1</sup>Department of Mechanical and Industrial Engineering, University of Illinois at Chicago, Chicago, IL, 60607, USA davidhe@uic.edu <sup>2</sup>NRG Systems, Hinesburg, VT, 05461, USA
- [19]: Gearbox Tooth Cut Fault Diagnostics Using Acoustic Emission and Vibration Sensors — A Comparative Study
- [20]: Imrek, H., & Unuvar, A. (2009). Investigation of influence of load and velocity on scoring of addendum modified gear tooth profiles. *Mechanism and Machine Theory*, 44(5), 938-948.
- [21]: Amarnath, M., & Lee, S. K. (2015). Assessment of surface contact fatigue failure in a spur geared system based on the tribological and vibration parameter analysis. *Measurement*, 76, 32-44 .
- [22] : Chaari, F., Fakhfakh, T., & Haddar, M. (2009). Analytical modelling of spur gear tooth crack and influence on gearmesh stiffness. *European Journal of Mechanics-A/Solids*, 28(3), 461-468.
- [23]: Rincon, A. F. D., Viadero, F., Iglesias, M., de-Juan, A., Garcia, P., & Sancibrian, R. (2012). Effect of cracks and pitting defects on gear meshing. *Proceedings of the Institution of Mechanical Engineers, Part C: Journal of Mechanical Engineering Science*, 226(11), 2805-2815.
- [24]: Liang, X., Zhang, H., Liu, L., & Zuo, M. J. (2016). The influence of tooth pitting on the mesh stiffness of a pair of external spur gears. *Mechanism and Machine Theory*, 106, 1-15.
- [25]: Z.G. Chen, Y.M. Shao, Mesh stiffness calculation of a spur gear pair with tooth profile modification and tooth root crack, *Mech. Mach. Theory* 62 (2013) 63 –74
- [26]: Ma, H., Li, Z., Feng, M., Feng, R., & Wen, B. (2016). Time-varying mesh stiffness calculation of spur gears with spalling defect. *Engineering Failure Analysis*, 66, 166-176.
- [27]: Sfakiotakis, V. G., & Anifantis, N. K. (2002). Finite element modeling of spur gearing fractures. *Finite elements in analysis and design*, 39(2), 79-92.
- [28]: Zamanian, A. H., & Ohadi, A. (2011). Gear fault diagnosis based on Gaussian correlation of vibrations signals and wavelet coefficients. *Applied Soft Computing*, 11(8), 4807-4819.

- [29]: Chaari.F, W. Baccar, M.S. Abbes, et al., Effect of spalling or tooth breakage on gearmesh stiffness and dynamic response of a one-stage spur gear transmission, *Eur.J. Mech. A Solids* 27 (2008) 691 –705.
- [30]: Bartelmus, W., & Zimroz, R. (2009). A new feature for monitoring the condition of gearboxes in non-stationary operating conditions. *Mechanical Systems and Signal Processing*, 23(5), 1528-1534.
- [31]: Hassan, A. R. (2009). Contact stress analysis of spur gear teeth pair. *World Academy of Science, Engineering and Technology*, 58(1), 597-602.
- [32]: Inalpolat, M., & Kahraman, A. (2009). A theoretical and experimental investigation of modulation sidebands of planetary gear sets. *Journal of Sound and Vibration*, 323(3-5), 677-696.
- [33]: Nakada T., Utagawa M., Dynamic loads acused by the varying elasticity of mating gear teeth, *Proceeding of the 6th Japan National Congress on Applied Mechanics*, 1956, p. 493-497.
- [34]: Xue, S., & Howard, I. (2018). Torsional vibration signal analysis as a diagnostic tool for planetary gear fault detection. *Mechanical Systems and Signal Processing*, 100, 706-728.
- [35]: Mbarek, A., Hammami, A., Rincón, A. F. D., Chaari, F., Rueda, F. V., & Haddar, M. (2021, February). Early Damage Detection in Planetary Gear Transmission in Down-Time Regime. In *International Workshop on Modelling and Simulation of Complex Systems for Sustainable Energy Efficiency* (pp. 31-37). Springer, Cham.
- [36]: Shing T. K., Dynamics and control of geared servomechanisms with backlash and friction consideration, PHD thesis, Harvard University and Industry, 1994.
- [37]: Tandon, N.; Mata, S. Detection of defects in gears by acoustic emission measurements. *J. Acoust. Emiss.* 1999, 19, 23–27.
- [38]: Li, H., Li, J., Liu, X., & Fok, A. (2012). Non-Destructive Examination of Interfacial Debonding in Dental Composite Restorations Using Acoustic Emission. *Composites and Their Applications*, 147.
- [39]: Gao, L., Zai, F., Su, S., Wang, H., Chen, P., & Liu, L. (2011). Study and application of acoustic emission testing in fault diagnosis of low-speed heavy-duty gears. *Sensors*, 11(1), 599-611.
- [40]: McFadden, P.D.; Smith, J.D. Acoustic Emission Transducer for the Vibration Monitoring of Bearings at Low Speeds. Report No. CUED/C-Mech/TR29, Engineering Department, Cambridge University: Cambridge, UK, 1983.
- [41]: Study and Application of Acoustic Emission Testing in Fault Diagnosis of Low-Speed Heavy-Duty Gears Lixin Gao 1 , Fenlou Zai 1 , Shanbin Su 1 , Huaqing Wang 2 , \*, Peng Chen 3 and Limei Liu 4

- [42]: Mba, R.H.; Finadlay, G.E. Condition Monitoring of Low-Speed Rotating Machinery Using Stress Waves. Proc. Inst. Mech. Eng. 1999, 213, 153-185.
- Waves. Proc. Inst. Mech. Eng. 1999, 213, 153-185.
- [43] : Abbas, M. S., Bouaziz, S., Chaari, F., Maatar, M., & Haddar, M. (2008). An acoustic–structural interaction modelling for the evaluation of a gearbox-radiated noise. International Journal of Mechanical Sciences, 50(3), 569-577.
- [44]: Kato, M., & Kozuka, N. (1996). U.S. Patent No. 5,508,477. Washington, DC: U.S. Patent and Trademark Office.
- [45]: Octobre2017, <https://electrotechnical-officer.com/operation-of-ships-induction-motors/>
- [46] : J.R.Ottewill, A.Ruszczczyk,D.Broda,monitoring tooth profile faults in epicyclic gearboxes using synchronously averaged motor currents : mathematical modeling and experimental validation,mssp(2016).
- [47]: H. Balan, M. I. Buzdugan, P. Karaisas, “Fault identification on electrical machines based on experimental analysis”, in Advances in Condition Monitoring of Machinery in Non-Stationary Operations, Springer, Berlin, Heidelberg, 2014, p. 611-630.
- [48]:Fourati,A(2017), Modélisation electromecanique d’une machine asynchrone sous approche angular, application au diagnostic des défauts des roulement en régime non stationnaire.
- [49] M. Blodt, P. Granjon, B. Raison, G. Rostaing, “Models for bearing damage detection in induction motors using stator current monitoring”, IEEE Trans. Ind. Electron. 55 (2008), no. 4, p. 1813-1822.
- [50]: Nandi, R. M. Bharadwaj, H. A. Toliyat, “Performance analysis of a three-phase induction motor under mixed eccentricity condition”, IEEE Trans. Energy Convers. 17 (2002), no. 3, p. 392-399. [17] R.
- [51]: R. Schoen, T. G. Habetler, F. Kamran, R. G. Bartfield, “Motor bearing damage detection using stator current monitoring”, IEEE Trans. Ind. Appl. 31 (1995), no. 6, p. 1274-1279.
- [52]:S. . H. Kia, H. Henao, G.-A. Capolino, “Gearbox monitoring using induction machine stator current analysis”, in 2007 IEEE International Symposium on Diagnostics for Electric Machines, Power Electronics and Drives, IEEE, 2007, p. 149- 154
- [53] : Zimroz, Radoslaw, and Anna Bartkowiak. "Investigation on spectral structure of gearbox vibration signals by principal component analysis for condition monitoring purposes." Journal of Physics: Conference Series. Vol. 305. No. 1. IOP Publishing, 2011

- [54]: Yasui, T., Kabetani, Y., Saneyoshi, E., Yokoyama, S., & Araki, T. (2006). Terahertz frequency comb by multifrequency-heterodyning photoconductive detection for high-accuracy, high-resolution terahertz spectroscopy. *Applied Physics Letters*, 88(24), 241104.
- [55]: Antonini, M., Barlaud, M., Mathieu, P., & Daubechies, I. (1992). Image coding using wavelet transform. *IEEE Transactions on image processing*, 1(2), 205-220.
- [56]: Flandrin, P., Rilling, G., & Goncalves, P. (2004). Empirical mode decomposition as a filter bank. *IEEE signal processing letters*, 11(2), 112-114.
- [57]: Combet, F., & Gelman, L. (2007). An automated methodology for performing time synchronous averaging of a gearbox signal without speed sensor. *Mechanical systems and signal processing*, 21(6), 2590-2606.
- [58]: Fakhfakh, T., Chaari, F., & Haddar, M. (2005). Numerical and experimental analysis of a gear system with teeth defects. *The International Journal of Advanced Manufacturing Technology*, 25(5), 542-550.
- [59] Barret, Philippe. "Régimes transitoires des machines tournantes électriques." (1987).
- [60] Ansari, A. A., and D. M. Deshpande. "Mathematical model of asynchronous machine in MATLAB Simulink." (2010).
- [61]: Chaari, F., Fakhfakh, T., Hbaieb, R., Louati, J., & Haddar, M. (2006). Influence of manufacturing errors on the dynamic behavior of planetary gears. *The International Journal of Advanced Manufacturing Technology*, 27(7), 738-746.
- [62]: Chen, K., Hu, J., & Peng, Z. (2017). Analytical Framework of Gearbox Monitoring Based on the Electro-mechanical Coupling Mechanism. *Energy Procedia*, 105, 3138-3145.
- [63]: Blodt, M., Chabert, M., Regnier, J., & Faucher, J. (2006). Mechanical load fault detection in induction motors by stator current time-frequency analysis. *IEEE Transactions on Industry Applications*, 42(6), 1454-1463.
- [64]: Feng, Z., Chen, X., & Zuo, M. J. (2018). Induction Motor Stator Current AM-FM Model and Demodulation Analysis for Planetary Gearbox Fault Diagnosis. *IEEE Transactions on Industrial Informatics*.
- [65]: Feki, N., Clerc, G., & Vexel, P. (2012). An integrated electro-mechanical model of motor-gear units—Applications to tooth fault detection by electric measurements. *Mechanical Systems and Signal Processing*, 29, 377-390.

- [66]: Chaari, F., Fakhfakh, T., & Haddar, M. (2005). Simulation numérique du comportement dynamique d'une transmission par engrenages en présence de défauts de dentures. *Mécanique & Industries*, 6(6), 625-633.
- [67] : Shiroishi, J. Y. S. T., Li, Y., Liang, S., Kurfess, T., & Danyluk, S. (1997). Bearing condition diagnostics via vibration and acoustic emission measurements. *Mechanical systems and signal processing*, 11(5), 693-705.
- [68]: Hassan, A. R. (2009). Contact stress analysis of spur gear teeth pair. *World Academy of Science, Engineering and Technology*, 58(1), 597-602.
- [69]: Ahmed Hammemi, Contribution to the study of the dynamic behavior of mechanical transmission in non-stationary conditions, 2015
- [70]: Timoshenko S., Baud R. V., « The strength of gear teeth », *Mechanical Engineering*, 1926, p. 1105-1109.
- [71]: Lin J., Parker R.G., Analytical characterization of the unique properties of planetary gear free vibration, *Journal of Vibration and Acoustics* 121(1999) 316–321.
- [72]: Radzevich, S. P., & Dudley, D. W. (1994). *Handbook of practical gear design*. CRC press.
- [73]: Nakada T., Utagawa M., Dynamic loads acused by the varying elasticity of mating gear teeth, *Proceeding of the 6th Japan National Congress on Applied Mechanics*, 1956, p. 493-497.
- [74]: Fernandez, P. G., de-Juan, A., Diez-Ibarbia, A., Sanchez-Espiga, J., & del Rincon, A. F. (2021). Acoustic intensity technique applied to monitor planetary gears. *Applied Acoustics*, 172, 107621.
- [75]: Yang, L. T., Shao, Y. M., Jiang, W. W., Zhang, L. K., Wang, L. M., & Xu, J. (2021). Effects of Tooth Surface Crack Propagation on Meshing Stiffness and Vibration Characteristic of Spur Gear System. *Applied Sciences*, 11(4), 1968.
- [76]: Gui, Y.; Han, Q.K.; Li, Z.; Chu, F.L. Detection and Localization of Tooth Breakage Fault on Wind Turbine Planetary Gear System considering Gear Manufacturing Errors. *Shock Vib.* 2014, 2014, doi:10.1155/2014/692347.
- [77] Thomson, W. T. "On-line current monitoring to detect electrical and mechanical faults in three-phase induction motor drives." (1994): 66-73.
- [78]: Hu, C., Smith, W. A., Randall, R. B., & Peng, Z. (2016). Development of a gear vibration indicator and its application in gear wear monitoring. *Mechanical Systems and Signal Processing*, 76, 319-336.

[79] : Caso, E., Fernandez-del-Rincon, A., Garcia, P., Diez-Ibarbia, A., & Sanchez-Espiga, J. (2020, September). Acoustic Emission Monitoring of Teeth Surface Damage Process in a Planetary Gearbox. In European Conference on Mechanism Science (pp. 256-264). Springer, Cham.

[80]: Hu, C., Smith, W. A., Randall, R. B., & Peng, Z. (2016). Development of a gear vibration indicator and its application in gear wear monitoring. *Mechanical Systems and Signal Processing*, 76, 319-336.

[81]: R.B. Randall, *Vibration-based condition monitoring: industrial, aerospace and automotive applications*, Wiley, Chichester, 2011

